processes

MDPI

Review

Oxidative Coupling of Methane for Ethylene Production: Reviewing Kinetic Modelling Approaches, Thermodynamics and Catalysts

Simoní Da Ros [1,*], Tahyná Barbalho Fontoura [2], Marcio Schwaab [3], Normando José Castro de Jesus [4] and José Carlos Pinto [2,*]

[1] UCL Institute for Sustainable Heritage, University College London, 14 Upper Woburn Place, London WC1H 0NN, UK
[2] Programa de Engenharia Química/COPPE, Universidade Federal do Rio de Janeiro, Cidade Universitária—CP: 68502, Rio de Janeiro 21941-972, RJ, Brazil; tahyna@peq.coppe.ufrj.br
[3] Departamento de Engenharia Química, Escola de Engenharia, Universidade Federal do Rio Grande do Sul, Rua Ramiro Barcelos 2777—Prédio 22202, Porto Alegre 90035-007, RS, Brazil; schwaab@ufrgs.br
[4] Braskem S.A., Rua Marumbi 1400, Campos Elíseos, Duque de Caxias 25221-000, RJ, Brazil; normando.jesus@braskem.com
* Correspondence: s.ros@ucl.ac.uk (S.D.R.); pinto@peq.coppe.ufrj.br (J.C.P.)

Abstract: Ethylene production via oxidative coupling of methane (OCM) represents an interesting route for natural gas upscaling, being the focus of intensive research worldwide. Here, OCM developments are analysed in terms of kinetic mechanisms and respective applications in chemical reactor models, discussing current challenges and directions for further developments. Furthermore, some thermodynamic aspects of the OCM reactions are also revised, providing achievable olefins yields in a wide range of operational reaction conditions. Finally, OCM catalysts are reviewed in terms of respective catalytic performances and thermal stability, providing an executive summary for future studies on OCM economic feasibility.

Keywords: natural gas upscaling; ethene; chemical reactors; thermal effects; catalyst stability

Citation: Da Ros, S.; Barbalho Fontoura, T.; Schwaab, M.; Castro de Jesus, N.J.; Pinto, J.C. Oxidative Coupling of Methane for Ethylene Production: Reviewing Kinetic Modelling Approaches, Thermodynamics and Catalysts. *Processes* **2021**, *9*, 2196. https://doi.org/10.3390/pr9122196

Academic Editor: Kody Powell

Received: 28 October 2021
Accepted: 30 November 2021
Published: 6 December 2021

1. Introduction

The oxidative coupling of methane (OCM) represents an interesting alternative process for producing ethylene, typically manufactured in steam-crackers from naphtha [1,2]. Here, OCM developments are critically revised in terms of kinetic mechanisms and respective applications towards chemical reactor modelling and design, discussing current challenges and directions for further research. Furthermore, thermodynamic aspects of the OCM reactions are also discussed, providing achievable olefins yields in a wide range of reaction conditions. Finally, OCM catalysts are revised in terms of the respective catalytic performances and thermal stability, providing an executive summary for future studies on OCM economic feasibility.

This work is organised as follows: Section 2 presents a bibliometric analysis of OCM scientific publications and patents, highlighting geographic, chronological and topic distributions; Section 3 revises OCM reaction and kinetic models, critically analysing chemical reactor modelling approaches; Section 4 summarises thermodynamic aspects of the OCM reactions and presents original calculations for extents of reaction, focusing on presenting maximum ethylene yields in a wide range of temperatures, pressures and feed compositions; Section 5 discusses OCM catalysts, summarising their performances and main features; Section 6 briefly discusses sustainability aspects of the OCM reactions; and, finally, Section 7 presents the main conclusions and opportunities for future work.

2. An Overview of OCM Scientific Publications and Patents

This section summarises the geographic and chronological distribution of OCM scientific publications and patents from approximately the last forty years of development of the OCM process, in order to identify the main industrial players and assess the technological development stage of OCM as a field of investigation. An extracted sample of scientific publications and patents is also analysed in relation to their topic distribution to identify the main areas of interest and areas which have been seemingly overlooked.

An initial search for publications was conducted using the '*all databases*' option in the "*Web of Science*" platform, using two sets of keywords to keep the search as general as possible. The two sets of keywords were composed of three words: (a) *oxidative*, *methane* and *coupling*; and four words: (b) *oxidative*, *methane*, *coupling* and *ethylene*. The initial search period was defined between 1980 and 2020.

From this initial search, 2581 and 794 results were found for keyword sets (a) and (b), respectively, at the original time of the search (April 2020), which represent the total number of publications including scientific and patent publications. A search conducted using the same method with the keyword '*OCM*' resulted in a similar value (2727 results between 1980 and 2020). It is important to note that the total number of manuscripts and patents in the analysed database has been updated since then, based on references cited by downloaded manuscripts and patents, new articles published in scientific journals and patents deposited in patent databases.

Based on these numbers, it is possible to speculate that the OCM technology is not completely mature, when compared to the number of search results that can be found for established industrial processes. For instance, 27,678 and 15,574 search results were found when the keywords '*hydrocarbon cracking*' and '*methane reforming*' were used for independent searches in the same period, respectively.

Despite the less substantial total number of search results when compared to the more traditional processes of hydrocarbon conversion, OCM technology has been the focus of a growing number of studies since 2007, as illustrated in Figure 1, where the chronological distributions of search results obtained for keyword sets (a) and (b) are plotted. As one can observe in Figure 1, OCM publications exhibit a bimodal distribution, with a maximum around 1994, followed by a reduction towards the late 1990s and early 2000 and an exponential increase from 2007 to recent years, which strongly correlates with the production volume of shale gas in the U.S., as illustrated in Figure 2, where the chronological distribution obtained for keyword set (a) is compared to the U.S. shale gas production, and the trends in prices of West Texas Intermediate (WTI) crude oil and Henry Hub natural gas.

Even though it might be expected that higher oil prices could encourage the development of cheaper alternative processes to the conventional cracking of ethane and/or heavier hydrocarbons to produce ethylene, the relationship between WTI crude oil prices and search results does not seem obvious. Instead, it is the price of natural gas that seems to more pronouncedly affect the efforts dedicated to OCM development, in combination with the increased production of shale gas, as previously mentioned.

The above relationship also makes sense when the geographical distribution of search results is considered, as shown in Figure 3, which illustrates how the U.S. appears to dominate the interest in the OCM technology, concentrating the highest number of search results obtained for keyword sets (a) and (b). Figure 3 further illustrates the rank of search results up to the ninth country position, which embraces 73 and 66% of the total number of search results for keywords in sets (a) and (b), respectively, from which the U.S., China, Germany, Japan and Russia represent the five countries that have dedicated the most effort towards the development of OCM technologies.

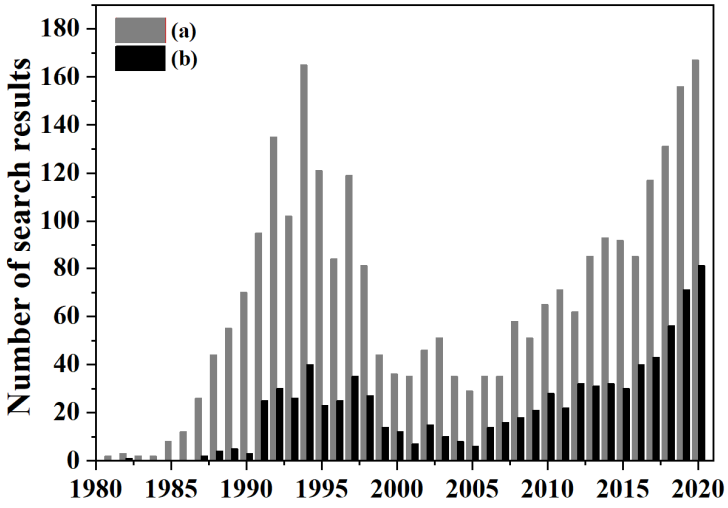

Figure 1. Chronological distributions of search results using the keyword sets (a): oxidative, methane and coupling; and (b): oxidative, methane, coupling and ethylene.

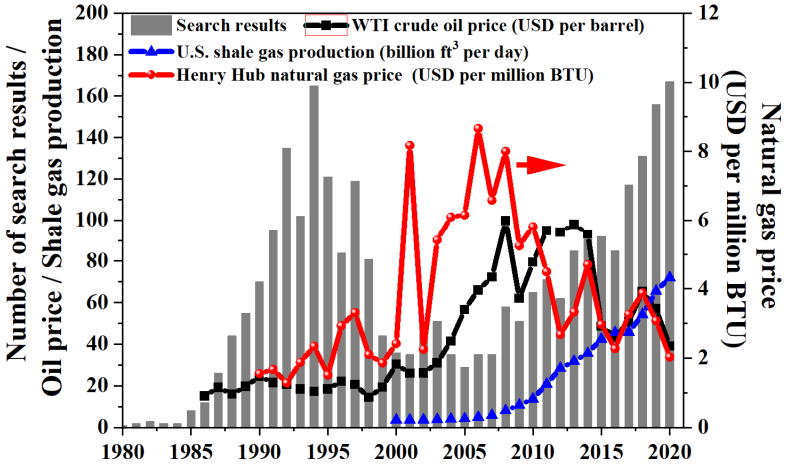

Figure 2. Comparison between the chronological distribution of search results using the keyword set (a) (oxidative, methane and coupling) and the prices of WTI crude oil (in USD per barrel) [3] and Henry Hub natural gas (in USD per million BTU) [4]; and the production of U.S. shale gas (in billion ft^3 per day) [5].

It is important to note that the above analysis was performed using the '*all databases*' option from the "*Web of Science*" platform, meaning that analysed distributions include search results from scientific publications, conference proceedings, reviews and patents. Therefore, to further evaluate the main players interested in the OCM technologies, the chronological and geographical distributions of search results were evaluated using the output number of files from two additional searches performed using the keyword sets (a) and (b), with the search database narrowed to contain only patent-related files, using the '*Derwent Innovations Index*' database from the "*Web of Science*" platform. Based on this analysis, the positive influence of the increase in natural gas production on the number of patents can be further assessed, as shown in Figure 4, which illustrates how the number of filed patents has been continuously increasing during the last decade, in concomitant agreement with the values of U.S. shale gas (Figure 2).

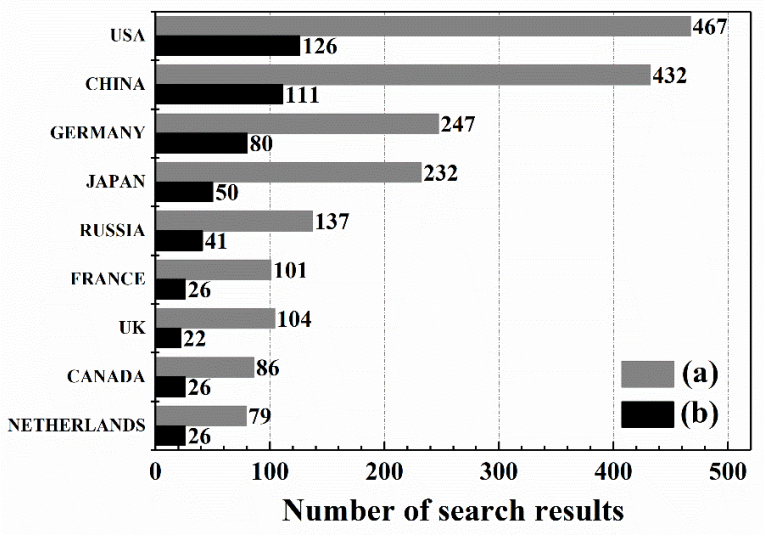

Figure 3. Geographical distributions of search results using the keyword sets (a): oxidative, methane and coupling; and (b): oxidative, methane, coupling and ethylene. Plotted countries represent 73 and 66% of the total number of search results for keyword sets (a) and (b), respectively.

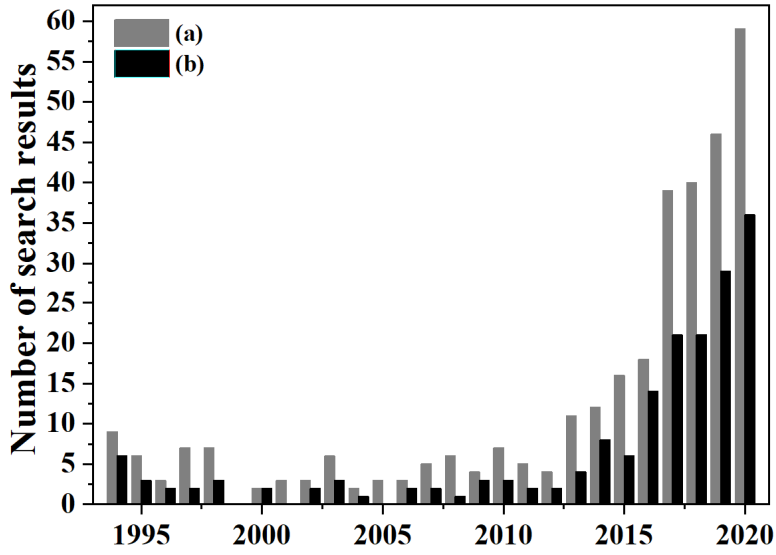

Figure 4. Chronological distributions of patent search results between 1994 and 2020 obtained using the keyword sets (a): oxidative, methane and coupling; and (b): oxidative, methane, coupling and ethylene.

The total number of patents, equal to 284 and 154 for keyword sets (a) and (b), respectively, also supports the previously suggested lack of maturity of the OCM technology, when compared to the numbers of patents filed on established industrial processes in the same period, as suggested by the number of results found while using the search words 'hydrocarbon cracking' and 'methane reforming', which resulted in 8442 and 2326 documents, respectively.

Based on the obtained data, the American companies Siluria Technologies Inc. and Lummus Technology (the latter having recently taken ownership of the former) have so far been the leaders in protecting their OCM developments, presenting a total of 30 patents during the last decade, followed by the Saudi Arabian Sabic Global Technologies, the Chinese Sinopec and the related China Petroleum & Chemical Corporation, the German Linde Group, and the Dutch Shell (Figure 5). Whereas the leadership on OCM intellectual property protection from American companies can be easily associated with the country's

largest worldwide production of natural gas, oil and natural gas liquids (NGL) (which includes ethane, liquified petroleum gas, LPG, and naphtha separated from the production of natural gas) [6], the driving forces behind the interest from Saudi Arabian companies cannot be directly associated with its natural gas production, which represented only 2.9% of the world share in 2018 (compared to 21.5% from the U.S., 4.2% from China and 17.3% from Russia in the same year) [6], but rather seem to be influenced by the country's second largest worldwide production of oil and natural gas liquids. This makes sense when the challenges of OCM industrial implementation are considered, as will be discussed throughout this review, since the process integration with existing plants of hydrocarbon conversion, such as ethane crackers, could provide economic benefits.

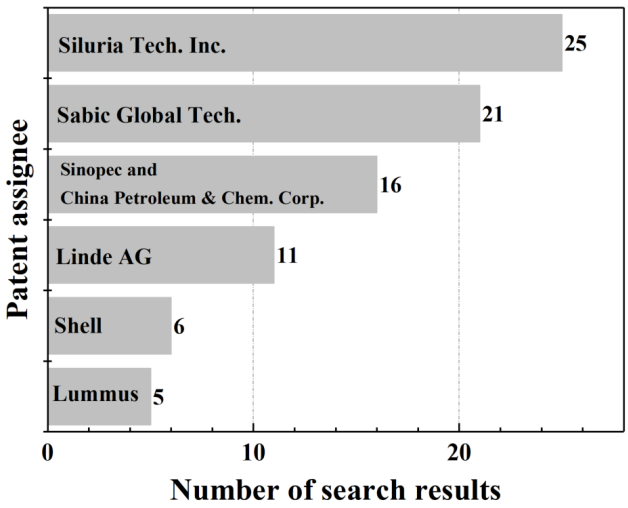

Figure 5. Filed patent distribution per assignee between 2010 and 2020, from the search using the '*Derwent Innovations Index*' database from the "*Web of Science*" platform and keyword set (b). For clarity, assignees with fewer than 5 filed patents were omitted. Numbers represent 69% of the total number of searched patents.

What Are OCM Scientific Publications and Patents about?

One of the main aims of the present review is the evaluation of the distribution of topics discussed in the published materials, in order to identify areas that have been receiving significant attention or have been seemingly overlooked by the technical communities. Thus, an extracted sample of the scientific papers (containing 120 papers published between 2016 and 2020) and patents (containing 121 deposits filed between 2010 and 2020) obtained from the search using keyword set (b) (ethylene, methane, oxidative, coupling) was evaluated in relation to the main focus of analysis.

Based on the evaluated scientific papers, seven different main subject streams have been identified: (1) modelling of the OCM process, embracing phenomenological and empirical mathematical descriptions of reactors and respective chemical kinetics [7–22], but also involving theoretical analyses of mechanistic models [23–29]; (2) economic evaluation of actual OCM commercial implementations, involving the analysis of capital and operational costs [30–35]; (3) assessment of environmental impacts, mainly involving the analysis of CO_2 emissions [31]; (4) development of new and/or improved catalysts for the production of ethylene from OCM reactions [27,36–73]; (5) development of alternative processes for CH_4 conversion into ethylene and/or other products, including, for instance, the non-oxidative coupling of methane [74–76]; (6) investigation of downstream purification strategies [77–79], concerning mainly the separation of products from the OCM reactor output stream; and finally, (7) the design, optimisation and development of OCM reactors for ethylene production, including the analysis of distinct reactor concepts (such as chemical looping [80–83], fluidized bed [84] and membrane reactors [85], in addition to the conventional packed-bed reactors [86]) [87,88], the analysis of different feed compositions

(including different oxidants or levels of inert dilution) [67,89], and experimental studies performed to optimise reactor performance through the investigation of the impact of reaction operational conditions on the ethylene yields [16,22,73,90].

Among the main identified subjects, the development of new catalysts for the OCM reaction seems to constitute the focus of most scientific publications, representing the subject of almost half of the assessed papers, as illustrated in Figure 6, which presents the obtained distribution of topics for scientific publications. In contrast, the remaining subjects have received less attention, with only 20% of mentioned subjects focusing on the mathematical description of the OCM process.

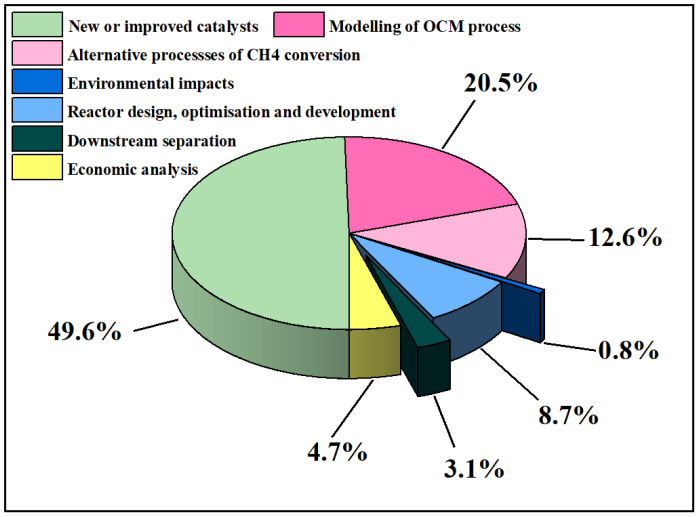

Figure 6. Distribution of topics in the extracted sample of scientific papers, containing 120 manuscripts published between 2016 and 2020.

From the extracted sample of filed patents, a different focus was identified, as illustrated in Figure 7, which presents the topic distribution among the main four identified subject streams. In this case, nearly half of the subjects were related to process flow diagrams, translating ideas of actual OCM process implementations, whereas only 27.8% of the mentioned topics described innovations in catalyst development. In addition, a significant part of the filed patents (almost 20%) proposes the use of OCM to produce other final products, rather than ethylene, such as ethylene oxide, liquid fuels, synthesis gas, poly-alpha-olefins, propylene, propanal, ethylbenzene, among others, therefore illustrating attempts to integrate OCM reactions with other processes. Finally, a smaller number of patents (2.4%) describes alternative processes for methane coupling, involving non-oxidative routes.

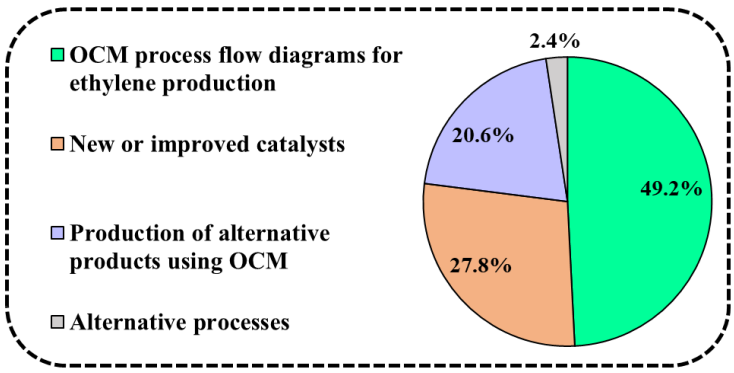

Figure 7. Distribution of topics in the extracted sample of patents, containing 121 patents filed between 2010 and 2020).

Among the filed patents related to process flow diagrams focused on ethylene production, five sub-streams of subjects could be identified, as illustrated in Figure 8. These sub-streams included: (1) downstream separation, involving analyses of pressure swing adsorption units or absorption towers, in addition to the conventional cryogenic distillation for separating CH_4 and olefins; (2) reactor development, involving analyses of fluidized bed reactors and special configurations for packed-bed reactors, including distinct catalyst bed configurations, specific distribution of catalytic layers, dilution of the catalytic bed with inert solids and the use of multi-stage adiabatic reactors; (3) OCM process flow diagrams, dealing with analyses of process design alternatives, including recycling and the use of distinct separation systems for purification of the OCM output reactor stream; (4) feeding systems and feed compositions, involving analyses of alternatives for mixing of reactants, spatial positioning of feed streams in the reactor vessel, investigation of different reactant feed compositions, and addition of water, CO_2, CO and chlorine radical precursors in the conventional CH_4 and O_2 feed streams; and, finally, (5) energy recovery, focusing on process ideas for utilising the heat produced in the OCM reactor for either adjusting the reactor feed mixture temperature and/or producing steam vapour.

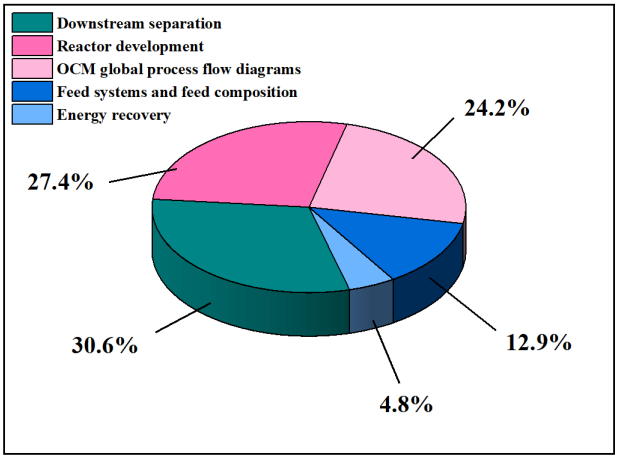

Figure 8. Distribution of subjects among extracted sample of patents related to OCM flow diagrams for ethylene production.

The analysis of topic distribution among scientific publications and patents interestingly suggests the distinct perspectives of the scientific community and industrial sector, in which the former seems to be concentrating efforts on the development of improved catalysts, while the latter seems to be trying to find solutions for engineering problems related to process implementation, in terms of downstream separation and reactor design. Therefore, this analysis provides some evidence for the need for further scientific studies concerning engineering aspects of the overall process implementation.

3. OCM Reactions and Kinetic Models

The oxidative coupling of methane (OCM) involves the conversion of methane mainly into ethane in the presence of oxygen and a suitable heterogeneous catalyst at high temperatures (reaction 1, Table 1).

Table 1. Possible global reactions involved in the OCM reaction mechanism [91,92].

Reaction	No.
$2CH_4 + \frac{1}{2}O_2 \rightarrow C_2H_6 + H_2O$	1
$C_2H_6 + \frac{1}{2}O_2 \rightarrow C_2H_4 + H_2O$	2
$C_2H_6 \rightarrow C_2H_4 + H_2$	3

Table 1. *Cont.*

Reaction	No.
$CH_4 + \frac{3}{2}O_2 \rightarrow CO + 2H_2O$	4
$CH_4 + O_2 \rightarrow CO + H_2O + H_2$	5
$CH_4 + 2O_2 \rightarrow CO_2 + 2H_2O$	6
$CO + \frac{1}{2}O_2 \rightarrow CO_2$	7
$C_2H_4 + 2O_2 \rightarrow 2CO + 2H_2O$	8
$CO + H_2O \rightarrow CO_2 + H_2$	9
$CO_2 + H_2 \rightarrow CO + H_2O$	10
$C_2H_4 + 2H_2O \rightarrow 2CO + 4H_2$	11

Ethane can be dehydrogenated to ethene via catalytic heterogeneous or thermal gas-phase oxidation (reactions 2 and 3). Partial and complete methane oxidation reactions are the main competitive pathways leading to CO and CO_2 (reactions 4–6). Consecutive reactions account for CO conversion to CO_2 (reaction 7), and ethene oxidation to CO (reaction 8). Moreover, the water–gas shift reaction (in both directions, reactions 9 and 10) and ethene steam reforming (reaction 11) have also been reported as important pathways [92].

The actual fundamental steps of the reaction mechanism described in Table 1 can be very complex, and both catalyst surface and gas-phase reactions must be taken into account to describe the overall kinetics through a model that can remain valid within a wide range of reaction conditions, enabling the more involved industrial reactor design [18,92–94]. It has been discussed that current kinetic models are not able to fully describe available experimental datasets, indicating that models proposed so far may be incomplete [29,95]. In spite of that, pioneering developments on OCM catalytic kinetic models made use of experiments performed in operational regions where gas-phase reactions could be minimised and thus neglected [92]. Similarly, gas-phase reaction kinetics have initially been investigated in the absence of catalysts [96,97].

3.1. Kinetics in the Absence of Catalyst

One of the pioneering studies regarding the OCM gas-phase reaction network in the absence of a heterogeneous catalyst was described by Zanthoff and Baerns [98]. These authors compiled a model involving a set of 164 elementary free-radical reactions and used kinetic constants obtained from the combustion literature. Later, dedicated experimental measurements, regression, sensitivity and parameter contribution analyses allowed for the reduction in the reaction network to 33 elementary free-radical reactions (reactions 1-33, Table 2), in accordance with a study that investigated OCM gas-phase reactions at atmospheric pressure, between 600 and 850 °C, using methane to oxygen feed ratios between 4 and 10 with different inert dilution levels, and spatial times between 0.1 and 1.9 $m^3 \cdot s \cdot mol^{-1}$ [96].

Table 2. Gas-phase reaction mechanism, as proposed by Chen et al. [96] for describing OCM reactions in the absence of catalysts and at atmospheric pressure.

Reaction	No.	Reaction	No.
$CH_4 + O_2 \leftrightarrow CH_3^\bullet + HO_2^\bullet$	1	$C_2H_6 + OH^\bullet \leftrightarrow C_2H_5^\bullet + H_2O$	18
$CH_4 + H^\bullet \leftrightarrow CH_3^\bullet + H_2$	2	$C_2H_6 + CH_3^\bullet \leftrightarrow C_2H_5^\bullet + CH_4$	19
$CH_4 + O^\bullet \leftrightarrow CH_3^\bullet + OH^\bullet$	3	$C_2H_5^\bullet + OH^\bullet \leftrightarrow C_2H_6 + O^\bullet$	20
$CH_4 + OH^\bullet \leftrightarrow CH_3^\bullet + H_2O$	4	$C_2H_5^\bullet + M \leftrightarrow C_2H_4 + H^\bullet + M$	21
$CH_4 + HO_2^\bullet \leftrightarrow CH_3^\bullet + H_2O_2$	5	$C_2H_5^\bullet + O_2 \leftrightarrow C_2H_4 + HO_2^\bullet$	22
$CH_3^\bullet + O_2 \leftrightarrow CH_3O^\bullet + O^\bullet$	6	$C_2H_4 + O_2 \leftrightarrow C_2H_3^\bullet + HO_2^\bullet$	23
$CH_3^\bullet + OH_2^\bullet \leftrightarrow CH_3O^\bullet + OH^\bullet$	7	$C_2H_4 + H^\bullet \leftrightarrow C_2H_3^\bullet + H_2$	24
$CH_3^\bullet + O_2 \leftrightarrow CH_2O + OH^\bullet$	8	$C_2H_4 + O^\bullet \leftrightarrow C_2H_3^\bullet + OH^\bullet$	25

Table 2. *Cont.*

Reaction	No.	Reaction	No.
$CH_3^\bullet + CH_3^\bullet + M \leftrightarrow C_2H_6 + M$	9 [a]	$C_2H_4 + OH^\bullet \leftrightarrow C_2H_3^\bullet + H_2O$	26
$CH_3O^\bullet + M \leftrightarrow CH_2O + H^\bullet + M$	10	$C_2H_4 + CH_3^\bullet \leftrightarrow C_2H_3^\bullet + CH_4$	27
$CH_2O + H^\bullet \leftrightarrow CHO^\bullet + H_2$	11	$C_2H_3^\bullet + M \leftrightarrow C_2H_2 + H^\bullet + M$	28
$CH_2O + CH_3^\bullet \leftrightarrow CHO^\bullet + CH_4$	12	$C_2H_3^\bullet + O_2 \leftrightarrow C_2H_2 + HO_2^\bullet$	29
$CHO^\bullet + M \leftrightarrow CO + M + H^\bullet$	13	$C_2H_4 + O^\bullet \leftrightarrow CH_3^\bullet + CHO^\bullet$	30
$CHO^\bullet + O_2 \leftrightarrow CO + HO_2^\bullet$	14	$C_2H_4 + OH^\bullet \leftrightarrow CH_3^\bullet + CH_2O$	31
$CO + HO_2^\bullet \leftrightarrow CO_2 + OH^\bullet$	15	$O_2 + H^\bullet + M \leftrightarrow HO_2^\bullet + M$	32
$CO + OH^\bullet \leftrightarrow CO_2 + H^\bullet$	16	$OH^\bullet + OH^\bullet + M \leftrightarrow H_2O_2 + M$	33
$C_2H_6 + H^\bullet \leftrightarrow C_2H_5^\bullet + H_2$	17		

[a] *M* denotes any other molecular species from the system.

However, the reaction network described in Table 2 was not suitable for describing experimental observations at higher pressure conditions up to nearly 1000 kPa [97], leading to the development of a modified and expanded reaction network where some of the reactions from Table 2 were removed and additional steps were included. The modifications accounted for the effect of pressure and the production of propane and propene, resulting in a system of 38 elementary free-radical reactions [97]. For instance, reactions No 11, 16, 20, 25 and 30 from Table 2 were not present in the updated model, which presented reactions No 1–6 summarised in Table 3 instead, in addition to reactions No 7–10, which involved the formation of propane and propene.

Table 3. Additional gas-phase reaction steps (in respect to Table 2), as proposed by Chen at al. [97], for describing OCM reactions in the absence of catalysts and under pressures up to 1000 kPa.

Reaction	No.	Reaction	No.
$CH_2O + OH^\bullet \leftrightarrow CHO^\bullet + H_2O$	1	$HO_2^\bullet + HO_2^\bullet \leftrightarrow O_2 + OH^\bullet + OH^\bullet$	6
$CH_2O + HO_2^\bullet \leftrightarrow CHO^\bullet + H_2O_2$	2	$C_2H_5^\bullet + CH_3^\bullet \leftrightarrow C_3H_8$	7
$C_2H_5^\bullet + HO_2^\bullet \leftrightarrow CH_3^\bullet + CH_2O + OH^\bullet$	3	$C_3H_8 + H^\bullet \leftrightarrow C_3H_7^\bullet + H_2$	8
$C_2H_3^\bullet + O_2 \leftrightarrow CH_2O + CHO^\bullet$	4	$C_2H_4 + CH_3^\bullet \leftrightarrow C_3H_7^\bullet$	9
$O_2 + H^\bullet \leftrightarrow OH^\bullet + O^\bullet$	5	$C_3H_7^\bullet \leftrightarrow C_3H_6 + H^\bullet$	10

The effect of pressure on the reaction rates involving unimolecular reactions was accounted for using Equation (1), where C_M represents the weighted sum of the concentration of all molecular species and k_u, k and k_∞ are reaction rate constants. Thus, at low pressure conditions, the reaction order was increased by one due to the influence of C_M, while this effect was less important at higher pressure conditions.

$$k_u = \frac{k \times C_M}{1 + k \times C_M} k_\infty \quad (1)$$

The mechanism based on the reaction steps presented in Tables 2 and 3 is constituted by an initiation step (reaction 1, Table 2), methyl radical production reactions (reactions 2–5), methyl radical oxidation steps (reactions 6–8), methyl radical coupling to ethane (reaction 9), radical decomposition reactions that lead to CO and CO_2 and involve methanal as an intermediary (reactions 10, 12–15, Table 2 and reactions 1–4, Table 3), ethane oxidation reactions that lead to ethene (reactions 17–19, 21–22, Table 2), ethene oxidation reactions that lead to acetylene (reactions 23–24, 26–29, Table 2), additional methyl radical production steps (reactions 31, Table 2), transfer reactions between oxygen and hydrogen radicals (reactions 32–33, Table 2 and reactions 5–6, Table 3) and, finally, reactions involving the formation of propane and its following dehydrogenation to propene (reactions 7–10, Table 3).

According to a contribution analysis performed with the model developed at atmospheric pressure, when the importance of a given reaction step for the consumption or production rate of a given species could be assessed, the methyl radical production originates mainly from hydrogen abstraction from methane by radicals (reaction steps No 2, 4 and 5, Table 2), whereas the initiation step involving molecular oxygen does not play an important role [96]. Moreover, the consumption of methyl radicals is mostly driven by reactions that result in the CO precursors $CH_3O^{\bullet}$ and CH_2O (reaction steps No 6–8, Table 2) and return to methane (reactions No 2, 12 and 19, Table 2). This would be the main reason for unselective oxidation, as the reaction leading to ethane production (No 9, Table 2) would account for only 33% of the methyl radical consumption.

The updated kinetic model for the OCM gas-phase reaction system comprised thirteen differential equations, one for each molecule j (O_2, H_2O, H_2O_2, H_2, CH_4, CH_2O, CO, CO_2, C_2H_2, C_2H_4, C_2H_6, C_3H_8, C_3H_6), and assumed that the reactor behaviour could be described by a plug-flow model at steady state, Equation (2), where temperature and pressure gradients could be neglected. In Equation (2), F_j is the molar flow rate of compound j, d_t is the reactor inner diameter, v_{ij} is the stoichiometric coefficient of compound j at reaction i, and r_i is the reaction rate of reaction i, described according to Equation (3). In Equation (3), k_i and k_{-i} are the rate constants of the forward and backward reaction, respectively, C_j is the molar concentration of the species j and α_{ij} represents the stoichiometric factor of the reactants. Radical concentrations were defined with the help of the quasi steady-state approximation [96].

$$\frac{dF_j}{dz} = \frac{\pi \times d_t^2}{4} \sum_{i=1}^{NR} v_{ij} r_i \text{ with } \mathrm{F_j}(z=0) = \mathrm{F_{j,0}} \tag{2}$$

$$r_i = \vec{r}_i - \overleftarrow{r}_i = k_i \prod_j C_j^{\alpha_{ij}} - k_{-i} \prod_j C_j^{\alpha_{ij}} \tag{3}$$

The reaction network used to describe the OCM kinetics in the absence of catalyst was later modified and expanded from 38 [97] to 39 [99] reaction steps, although these modifications would not significantly change previous model interpretations. Modified reaction steps (reactions 7, 9 and 10 in Table 3) were re-written considering the presence of a collision partner, M, while the additional included step further accounted for the formation of ethyl radicals from ethane, Equation (4).

$$C_2H_6 \leftrightarrow C_2H_5^{\bullet} + H^{\bullet} \tag{4}$$

These pioneering studies contributed to the understanding of the effects of operational variables on achievable values of conversions and products distribution. For instance, CH_4 conversions have been shown to reach up to approximately 33%, depending on the O_2 feed composition (Figure 9). However, higher spatial times can lead to a reduction in ethene and ethane selectivities, while CO and CO_2 productions can increase considerably, Figure 10a. The linear effect of temperature, in turn, has also been shown to be positive for increasing CH_4 and O_2 conversions and CO and CO_2 selectivities, whereas ethene and ethane selectivities are reduced (Figure 10b).

Higher pressures were reported to promote CH_4 and O_2 conversions, as shown in Figure 11a, while its effect on selectivities of carbonaceous products was less pronounced and depended on O_2 conversion, Figure 11b. These results suggest that C2 yields might be increased at higher pressures, as higher methane conversions can be achieved while keeping C2 selectivity nearly constant, at least for conditions of high oxygen conversions. A similar effect of pressure was reported by Ekstrom et al. [100] and Beck et al. [101], who showed the beneficial effect of pressure for C2 and C3 yields in the presence of catalyst up to 10 bar.

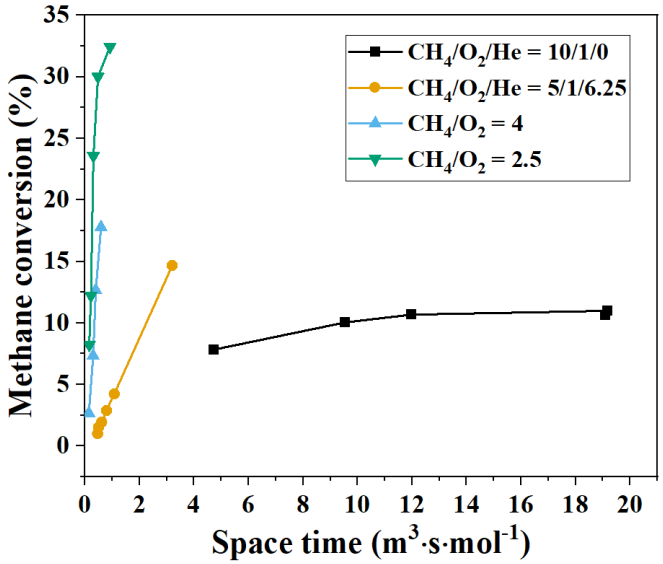

Figure 9. Effect of spatial time on experimental CH_4 conversion for different feed compositions at atmospheric pressure and in the absence of catalyst [96,97]. The maximum temperature across the reactor ranged between 790 and 826 °C at the analysed conditions. Spatial time is defined as the ratio between the reactor volume and the inlet molar flow rate of CH_4.

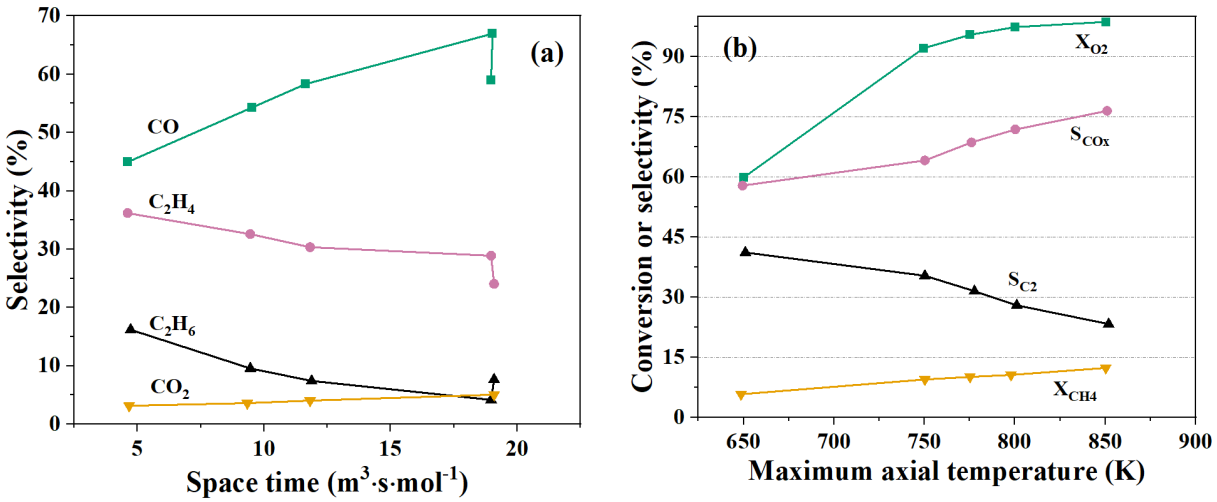

Figure 10. Effect of spatial time on carbon selectivities at 790 °C and CH_4:O_2:He = 10:1:0 (**a**) and effect of maximum reactor temperature on C_2 and CO_x (*S*) selectivities and CH_4 and O_2 conversions (X_{CH4} and X_{O2}) at CH_4:O_2:He of 10:1:0 and spatial time of 1.9 $m^3 \cdot s \cdot mol^{-1}$ (**b**), at atmospheric pressure and in the absence of catalyst [96,97].

3.2. Kinetics in the Presence of Catalyst

In the presence of catalyst, and assuming that gas-phase reactions are not significant (as suggested by experiments performed in the absence of catalyst), a one-dimensional, pseudo-homogeneous plug-flow model embracing 10 reaction steps, as presented in Table 4, was able to fairly well describe experimental data obtained over a La_2O_3/CaO catalyst in a catalytic packed-bed reactor [92]. The model was built using experimental data acquired under pressure between 1 and 1.3 atm, maximum axial reactor temperature between 700 and 955 °C, inlet CH_4/O_2 molar ratio between 5 and 10, CH_4 conversion between 1 and 32% and O_2 conversion between 15–100%. The whole model contained 52 parameters which were estimated with a total of 135 experiments. According to the authors, the main drawback of this model lies in the assumption that gas-phase reactions are negligible, limiting its application to reactors with small gas-phase volumes.

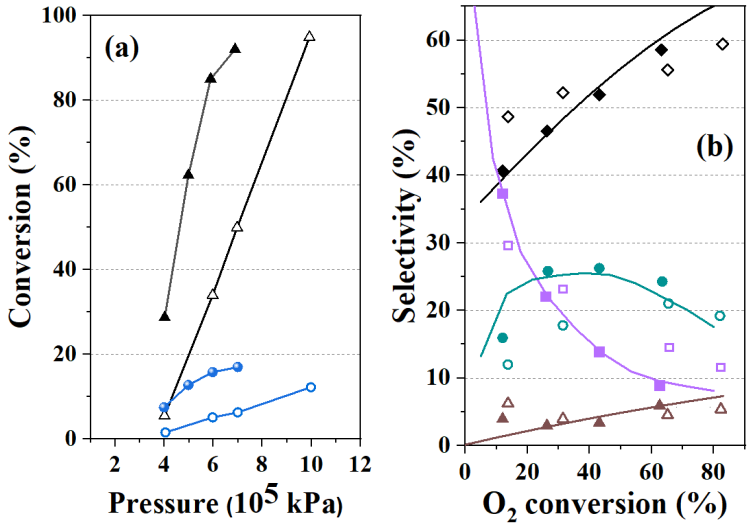

Figure 11. (**a**): Pressure effect on O_2 (Δ, ▲) and CH_4 (•, ○) conversions at 817 °C and inlet CH_4/O_2 molar ratio equal to 10 (empty symbols) and equal to 5 (filled symbols). (**b**): Carbon selectivities for C_2H_4 (•, ○), C_2H_6 (■, □), CO (◊, ♦), and CO_2 (Δ, ▲) at 1 atm and 827 °C (filled symbols and solid lines), and at 4 atm at 805 °C (empty symbols), for inlet CH_4/O_2 molar ratio equal to 4 [97]. Continuous lines are for visualisation only.

Table 4. Reaction steps considered in the kinetic model proposed by Stansch et al. [92] to describe OCM in the presence of a La_2O_3/CaO catalyst.

Reaction	Reaction Rate Equation
$CH_4 + 2O_2 \rightarrow CO_2 + 2H_2O$	$r_1 = \frac{k_1 p_{CH_4}^{m_1} p_{O_2}^{n_1}}{(1+K_{1,CO_2} p_{CO_2})^{n_1}}$
$2CH_4 + \frac{1}{2}O_2 \rightarrow C_2H_6 + H_2O$	$r_2 = \frac{k_2 \left(K_{O_2} p_{O_2}\right)^{n_2} p_{CH_4}}{\left(1+\left(K_{O_2} p_{O_2}\right)^{n_1} + K_{CO_2} p_{CO_2}\right)^2}$
$CH_4 + O_2 \rightarrow CO + H_2O + H_2$	$r_3 = \frac{k_3 p_{CH_4}^{m_3} p_{O_2}^{n_3}}{(1+K_{3,CO_2} p_{CO_2})^{n_3}}$
$CO + \frac{1}{2}O_2 \rightarrow CO_2$	$r_4 = \frac{k_4 p_{CH_4}^{m_4} p_{O_2}^{n_4}}{(1+K_{4,CO_2} p_{CO_2})^{n_4}}$
$C_2H_6 + \frac{1}{2}O_2 \rightarrow C_2H_4 + H_2O$	$r_5 = \frac{k_5 p_{C_2H_6}^{m_5} p_{O_2}^{n_5}}{(1+K_{5,CO_2} p_{CO_2})^{n_5}}$
$C_2H_4 + 2O_2 \rightarrow 2CO + 2H_2O$	$r_6 = \frac{k_6 p_{C_2H_4}^{m_6} p_{O_2}^{n_6}}{(1+K_{6,CO_2} p_{CO_2})^{n_6}}$
$C_2H_6 \rightarrow C_2H_4 + H_2$	$r_7 = k_7 p_{C_2H_6}$
$C_2H_4 + 2H_2O \rightarrow 2CO + 4H_2$	$r_8 = k_8 p_{C_2H_4}^{m_8} p_{H_2O}^{n_8}$
$CO + H_2O \rightarrow CO_2 + H_2$	$r_9 = k_9 p_{CO}^{m_9} p_{H_2O}^{n_9}$
$CO_2 + H_2 \rightarrow CO + H_2O$	$r_{10} = k_{10} p_{CO_2}^{m_{10}} p_{H_2}^{n_{10}}$

p_i is the partial pressure of compound j; k_i denotes the specific reaction rate constant for reaction i, which is related to temperature by the Arrhenius equation; K_i represents the equilibrium adsorption constants, and m_i and n_i are parameters related to the order of the reaction i with respect to the compound j.

Figure 12 shows the effect of spatial time on CH_4 and O_2 conversions, and main carbon containing products yields, at 700 and 830 °C, over a La_2O_3/CaO catalyst [92]. No further increase in the CH_4 conversion with spatial time was observed when O_2 was completely consumed. Moreover, ethane yield behaviour supported the hypothesis that ethane is a primary product, as evidenced by the observation of a smooth maximum as a function of spatial time (Figure 12b). Ethene is also suggested as an intermediate compound, as its yield is levelled off. Finally, CO and CO_2 were also assumed to be primary products. CO yield goes through a maximum at higher temperatures, indicating its likely conversion to CO_2, Figure 12c. The catalytic conversion of CO into CO_2 was also supported by experiments performed with CO and O_2 in the feed only, over a Li/MgO catalyst [102].

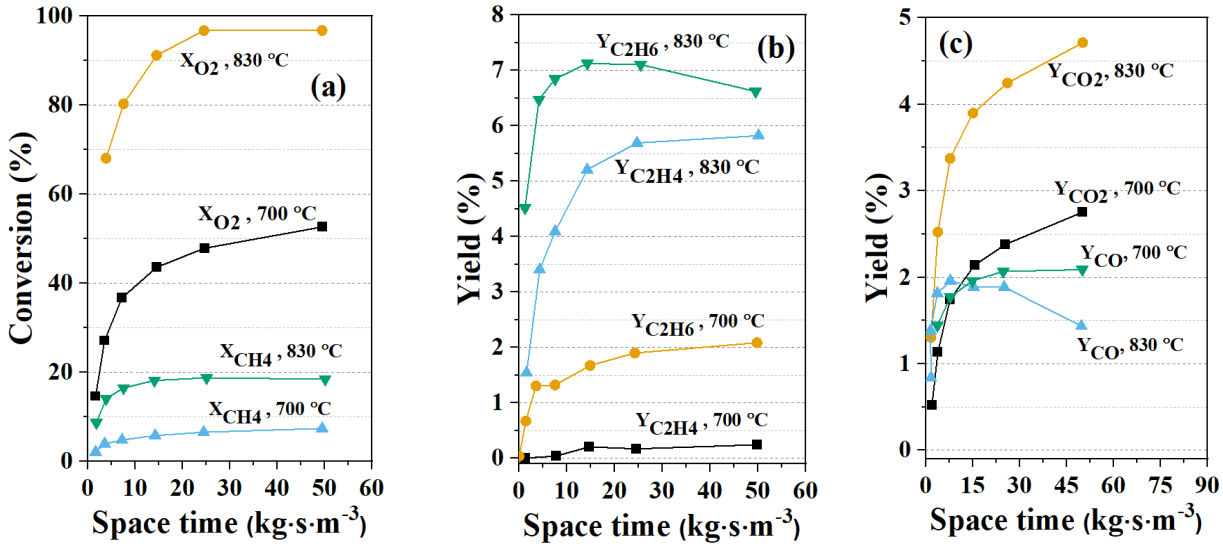

Figure 12. Effect of spatial time on (**a**) CH_4 and O_2 conversion at 700 (▲, ■) and 830 °C (▼, ●); (**b**) C_2H_4 and C_2H_6 yields at 700 (■, ●) and 830 °C (▲, ▼); and (**c**) CO_2 and CO yields at 700 (■, ▼) and 830 °C (●, ▲). Inlet CH_4:O_2:N_2 feed composition equal to 70:10:20 vol% [92].

Based on kinetic parameter estimates, the increase in C2 selectivity with reaction temperature has been rationalised as being due to the higher activation energy for ethane formation, when compared to activation energies for CO and CO_2 formations from CH_4 [92]. However, the positive effect of temperature on C2 selectivity has also been reported as being due to the decrease in the rate of formation of carbon oxides from the decomposition of methyl peroxy radicals (such as $CH_3OO^{\bullet}$) at the catalyst surface, which would be less favoured at higher temperatures [103].

Furthermore, steam-reforming reactions of CH_4 and C_2H_6 were ruled out by experiments performed using only methane and water, and ethane and water as feed over the La_2O_3/CaO catalyst. Even at high temperatures (tested between 800 and 880 °C) and spatial times, methane conversion was negligible, whereas ethane was converted mainly into ethene, indicating its conversion to ethene via dehydrogenation. Conversely, a feed comprising only ethene and water produced mainly CO and CO_2, suggesting that ethene might be converted by steam reforming (Table 4, reaction 8) and implying the importance of water–gas shift reactions in the mechanism (Table 4, reaction 9–10). The rate of C2 formation was observed to increase linearly with the methane partial pressure, whereas it passed through a maximum as a function of the O_2 partial pressure. On the other hand, increasing both CH_4 and O_2 partial pressures caused a positive linear effect on the rate of CO_x formation [92].

Moreover, experiments performed with the co-feeding of CH_4, O_2 and CO_2 showed that the increase in the CO_2 partial pressure (whereas keeping CH_4 and O_2 partial pressures constant) in the feed was harmful to C2 formation rates over a La_2O_3/CaO catalyst, as shown in Figure 13a [92]. A similar effect from the co-feeding of CH_4, O_2 and CO_2 was also reported over a Li/MgO catalyst [102]. The authors further verified that the reaction of CH_4 with CO_2 to CO could be promoted at OCM reaction conditions, by performing reactions using only CH_4 and CO_2 as feed (the importance of gas-phase methane dry reform was ruled out based on experiments performed in the absence of the catalyst). The effect of CO_2 was evaluated while keeping the partial pressures of CH_4 and O_2 and total pressure constant, by using helium as balance gas [102]. Thus, the CO_2 effect was not related to total pressure or methane partial pressure effects. In line with results from previous studies [92,93], the increase in the CO_2 partial pressure resulted in lower methane conversions, as shown in Figure 13b, and lower formation rates of C2 and COx products (not shown).

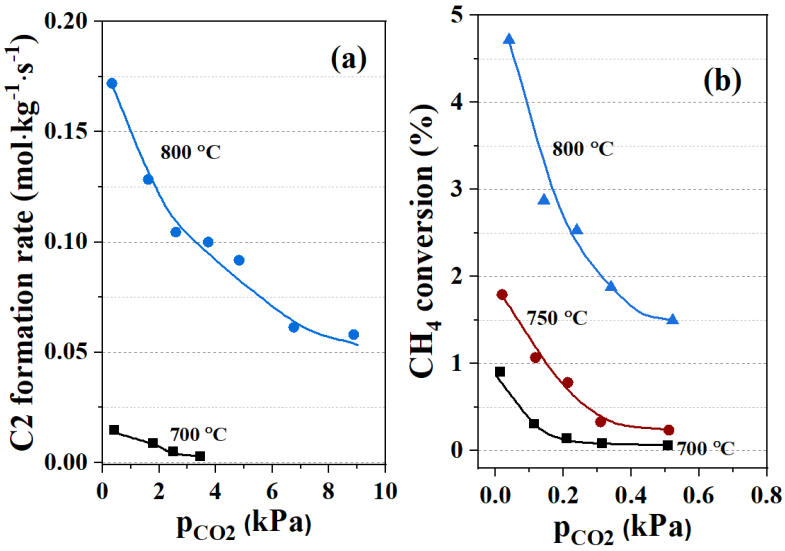

Figure 13. (**a**): Effect of CO_2 partial pressure on C2 formation rates over a La_2O_3/CaO catalyst at 700 (■) and 800 °C (●) (p_{CH4}, p_{O2} and p_{N2} equal to 51, 7.3 and 42.7 kPa, respectively) [92]. (**b**): Effect of CO_2 partial pressure on CH_4 conversion at 700 (■), 750 (●) and 800 °C (▲) over Li/MgO catalyst with p_{CH4}, p_{O2} and p_{tot} equal to 0.2, 0.01 and 1 atm, respectively [102]. Continuous lines are for visualisation only.

Therefore, it has been concluded that CO_2 might be adsorbed on catalyst active sites, resulting in an inhibiting effect on C2 formation [18]. For instance, the competition between CO_2 and O_2 for the same surface active sites was proposed to explain the rate of ethane formation (Table 4, reaction 2) and the inhibiting effect of CO_2 was also taken into account in oxidation reactions (Table 4, reactions 1, 3, 4, 5 and 6) [92]. This hypothesis is in line with previous suggestions [102], as it has been verified that the C2 selectivity can remain constant with the increase in the CO_2 feed partial pressure (even though reaction rates were reduced), indicating a possible common CH_4 activation site for both C2 and COx species, which would be poisoned by CO_2.

Following the kinetic model proposed by Stansch et al. [92], an extended model in which the presence of gas-phase reactions was also considered has also been proposed [93]. This approach initially considered 10 catalytic reaction steps, being further expanded to 14 [104] and finally to 26 [105] catalytic reaction steps, which were coupled to the system of 39 gas-phase reaction steps described in Section 3.1. Table 5 illustrates the 26 catalytic reaction steps as proposed by these authors. In this table, a catalytic surface site is represented by '*', while active oxygen species are represented by 'O*'. According to this reaction network, the formation of methyl radicals is believed to occur in accordance with the Eley–Rideal mechanism, where gas-phase methane reacts with oxygen active species at the catalyst surface, reaction 2, Table 5 [93,106–109].

This approach would also imply a unique identity for oxygen active species, which would be produced from the dissociative adsorption of O_2. Indeed, the dissociative adsorption of O_2 over MgO, Li-MgO and Sn-Li-MgO catalysts has been demonstrated by experiments involving isotopes of O_2. According to these experiments, the switch from a gas feed containing $^{16}O_2$ to a gas feed containing $^{18}O_2$ over a catalytic bed at steady-state conditions at 750 °C allowed for the observation of $^{16}O^{18}O$ species by mass spectrometry, supporting the dissociative adsorption hypothesis [106].

However, the participation of oxygen active species from catalyst surfaces has also been demonstrated. In this case, CH_4 pulse experiments performed in the absence of O_2 have proven the production of $CH_3^{\bullet}$ radicals and CO over Sm_2O_3 and $CH_3^{\bullet}$ radicals, CO and CO_2 over MgO catalysts at 450 and 550 °C, respectively [107].

Table 5. Catalytic surface reaction steps as proposed by Kechagiopoulos et al. [105].

No	Catalytic Reaction	No	Catalytic Reaction
1	$O_2 + 2* \leftrightarrow 2O*$	14	$C_2H_4 + O* \leftrightarrow C_2H_4O*$
2	$CH_4 + O* \leftrightarrow CH_3^{\bullet} + OH*$	15	$C_2H_4O* + O* \leftrightarrow C_2H_3O* + OH*$
3	$C_2H_6 + O* \leftrightarrow C_2H_5^{\bullet} + OH*$	16	$C_2H_3O* + O* \leftrightarrow CH_2O* + HCO*$
4	$C_2H_4 + O* \leftrightarrow C_2H_3^{\bullet} + OH*$	17	$C_2H_5^{\bullet} + O* \leftrightarrow C_2H_4 + OH*$
5	$2OH* \leftrightarrow H_2O* + O*$	18	$CH_3O^{\bullet} + O* \leftrightarrow CH_2O + OH*$
6	$H_2O* \leftrightarrow H_2O + *$	19	$CH_2O + O* \leftrightarrow CHO^{\bullet} + OH*$
7	$CH_3^{\bullet} + O* \leftrightarrow CH_3O*$	20	$CHO^{\bullet} + O* \leftrightarrow CO + OH*$
8	$CH_3O* + O* \leftrightarrow CH_2O* + OH*$	21	$H_2 + O* \leftrightarrow H^{\bullet} + OH*$
9	$CH_2O* + O* \leftrightarrow HCO* + OH*$	22	$H_2O_2 + O* \leftrightarrow HO_2^{\bullet} + OH*$
10	$HCO* + O* \leftrightarrow CO* + OH*$	23	$HO^{\bullet} + O* \leftrightarrow O^{\bullet} + OH*$
11	$CO* + O* \rightarrow CO_2* + *$	24	$H_2O + O* \leftrightarrow HO^{\bullet} + OH*$
12	$CO + * \rightarrow CO*$	25	$HO_2^{\bullet} + O* \leftrightarrow O_2 + OH*$
13	$CO_2 + * \leftrightarrow CO_2*$	26	$HO_2^{\bullet} + * \leftrightarrow OH^{\bullet} + O*$

Broadly, the above general reaction network has been supported by experimental studies conducted at atmospheric pressures. For instance, the degradation of C2 compounds involving catalytic surface steps is in agreement with the positive effect that short spatial times have on C2 selectivities [110,111]. However, the type of reactor where the above reaction network occurs can also play a very important role to explain the process outputs. For this reason, modelling approaches used to describe OCM reactors are discussed in the following sections.

3.3. Modelling Approaches for OCM Reactors

Different reactors have been considered for the OCM process, including fluidized bed (FBR) [112–114], membrane (MR) [115–117] and packed-bed (PBR) reactors [14,18,105,118–123], with their advantages, drawbacks and catalytic performances being recently reviewed by Cruellas et al. [124]. As stressed by these authors, PBR and FBR represent the most common configurations used to perform OCM studies, due to their wide use in the chemical industry, easy scaling-up, easy heat management (in the case of fluidized bed reactors), and wide availability on a laboratory scale.

Indeed, the present analysis focused on the modelling and simulation of OCM reactors and found that the great majority (48% of a sample of 30 scientific publications) of available studies was dedicated to PBR, while FBR and MR were investigated in 26 and 9% of the analysed studies, respectively, with the remaining 17% being related to other reactor types, including gas–solid vortex reactors (GSVR) and spouted bed reactors (Figure 14a). The developed models were based mainly on the homogeneous (or pseudo-homogeneous) kinetic approach, considering that this approach is simpler and more suitable to describe OCM reactions than more complex heterogeneous models (Figure 14b). It was also possible to verify that the large majority of these works used the kinetic mechanism developed by Stansch et al. [92] (Table 4) as a reference, due to its simplicity and applicability (Figure 14c), whereas distinct types of catalysts have been considered (Figure 14d). Regarding the energy balances, most studies assumed that reactions were performed in adiabatic or isothermal mode, which can constitute a major drawback for the interpretation of large-scale industrial reactors and somewhat hide the important heat transfer effects that take place in the catalyst bed. In the next sections, some of these models and their characteristic features are discussed.

3.3.1. Modelling Approaches for Packed-Bed Reactors

As introduced in Section 3.3, PBR has been one of the most investigated OCM reactor types and its modelling approaches can be classified according to the phenomena in the reactor and catalyst scale. For instance, one- or two-dimensional models are usually applied when significant radial gradients of concentration and/or temperature are considered absent or present, respectively, whereas pseudo-homogeneous or heterogeneous models

are often employed to describe one or more phases in the system, usually associated with the absence or presence of concentration and/or temperature gradients inside catalyst particles [123,125].

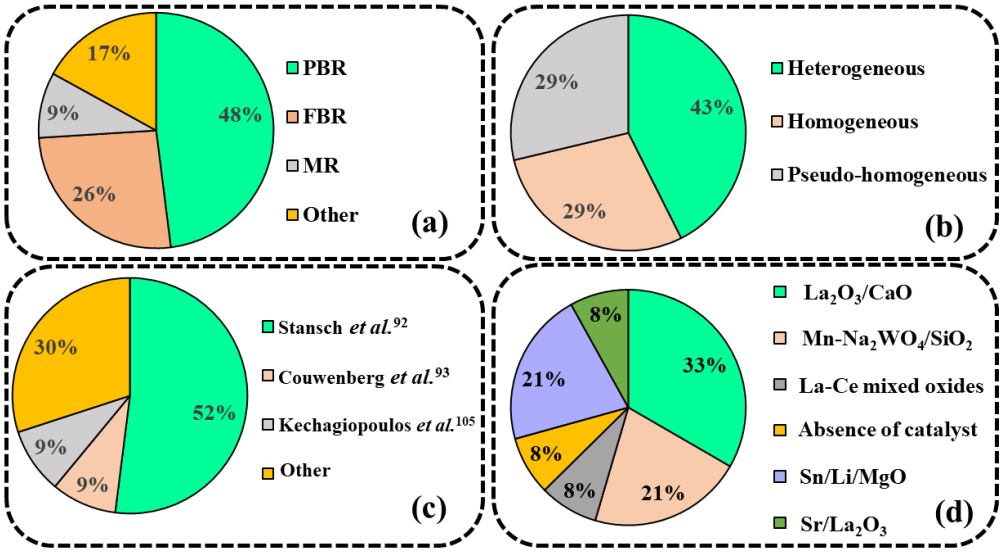

Figure 14. Distributions of types of reactors (**a**), models (**b**), kinetic mechanisms (**c**) and catalysts (**d**) used in modelling studies. Percentages have been calculated from a sample of 30 papers.

Pioneering studies on the modelling of OCM PBRs considered an isothermal, heterogeneous model at steady-state conditions, where mass balances described the external gas phase and the gas phase contained within the catalyst pores [118]. These authors showed the importance of considering mass transport limitations for the proper reactor description of reaction events even when no significant concentration gradients were present for stable compounds, such as main reactants and products. Due to the high reactivity of radical intermediates, significant concentration gradients of radical species could be expected to develop, so that the neglection of gradients might result in erroneous predictions of C2 selectivity [18,118]. However, temperature gradients and pressure drops were considered unimportant.

The model proposed by Couwenberg et al. [93,118], briefly illustrated by Equations (5) and (6), where ε_b, F_v, A_s, D_i, $D_{e,i}$ and ε_c represent bed porosity, volumetric flow rate, reactor cross-sectional area, molecular diffusion coefficient, effective internal diffusion coefficient and catalyst porosity, respectively, represented a great advance when compared to previous and simpler models, such as the one proposed by Stansch et al. [92]. For the first time, concentration gradients of molecular and radical species between the inner catalyst particle and the bulk reactor gas phase were explicitly considered in a model which simultaneously coupled the distinct reaction networks occurring at the gas phase, $R_{i,g}$, and catalytic surface, $R_{i,c}$. In this model, the gas-phase reaction network was considered to follow the mechanism involving the 39 reaction steps as described in Section 3.1, while the reaction network on the catalyst surface was described using 10 reaction steps for which kinetic parameters were either estimated with available experimental data or calculated from physico-chemical relationships [93].

$$\frac{F_v}{\varepsilon_b A_s}\frac{\partial C_{i,g}}{\partial z} = \frac{D_i}{r}\frac{\partial}{\partial r}\left(r\frac{\partial C_{i,g}}{\partial r}\right) + R_{i,g} \quad (5)$$

$$-\frac{D_{e,i}}{\xi^2}\frac{\partial}{\partial \xi}\left(\xi^2\frac{\partial C_{i,c}}{\partial \xi}\right) = R_{i,c} + \varepsilon_c R_{i,g} \quad (6)$$

However, while this approach allowed for a good description of experimental observations within the range of conditions used in the regression analysis (which involved pressures between 1.1 and 1.5 atm), the predicted catalytic performance was unable to

describe conversion levels at higher pressure conditions, as illustrated in Figure 15. As mentioned previously, the description of the reaction network on the catalyst surface was later extended from 10 to 14 [104], and later to 26 elementary steps [105], as described in Table 5.

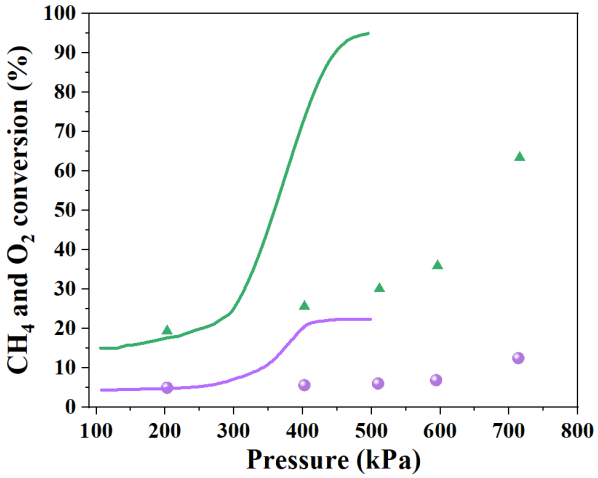

Figure 15. CH_4 (●, purple line) and O_2 (▲, green line) experimental conversion and model prediction (lines) [93]. Reaction conditions were 712 °C, CH_4/O_2 molar ratio of 4 and spatial time equal to 1 kg·s·mol^{-1}, using a Sn/Li/MgO catalyst.

Further model improvements included the explicit consideration of the effects of temperature, pressure and gas composition on the previously mentioned molecular and effective internal diffusion coefficients, D_i and $D_{e,i}$, as illustrated by Equations (7) and (8) [105], where $D_{i,j}$ is the molecular diffusion coefficient of component i in j; M_i and M_j are the molecular weights of compounds i and j; Σv_i represents the sum of atomic diffusion volumes for the atoms of the molecule i; x_i is the molar fraction of the component i; N_{mol} and N_{rad} are the total number of molecules and radicals, respectively, and τ_c is the catalyst pellet tortuosity.

$$D_{i,j} = 3.16 \times 10^{-8} \frac{T^{1.75}}{P_{tot}\left(\left(\sum v_i\right)^{1/3} + \left(\sum v_j\right)^{1/3}\right)} \left(\frac{1}{M_i} + \frac{1}{M_j}\right)^{1/2} \quad (7)$$

$$D_{e,i} = \frac{\varepsilon_c}{\tau_c} \left((1 - x_i) \left(\sum_{j=1(j \neq i)}^{N_{mol}+N_{rad}} \frac{x_j}{D_{i,j}} \right)^{-1} \right) \quad (8)$$

It is interesting to note that this modelling approach, initially built from experimental observations using Li/MgO and Sn-doped Li/MgO catalysts [118], was also applied to, and able to explain experimental data from Sr/La_2O_3 [126], La-Sr/CaO and Na-Mn-W/SiO_2 catalysts [16,17]. However, the investigated pressure conditions were limited to values below 1.9 atm.

Additional modelling approaches have also been reported. For instance, Valadkhani et al. [91] considered a transient, one-dimensional pseudo-homogeneous model with axial mixing to describe mass and energy balances for reacting species, where the reaction network involved up to 10 steps, similar to the ones proposed by Stansch et al. [92], and reaction rate equations were described by power law relationships. However, while a good agreement between model simulations and experimental catalytic performances obtained over a Na-Mn-W/SiO_2 catalyst was reported, pressure conditions were also limited to values below 2 atm. In another study [14], a steady-state, two-dimensional pseudo-homogeneous model with axial mixing was used to describe mass and energy balances. Using reaction networks such as the one suggested by Stansch et al. [92], the

authors were also able to validate their model with experimental observations, although this validation was limited to atmospheric pressure conditions.

Further OCM PBR developments have explored experimentally the feasibility of operation under autothermal conditions, by using the feed as coolant [127]. However, to understand reactor performance behaviour under this operational mode, an analysis of the multiple steady states of the OCM reaction network is necessary. Unfortunately, due to the complexity of the reactor fluid dynamic and kinetics, there is no unequivocal theoretical study available in the literature showing these complex nonlinear behaviours for real OCM reactors, even though efforts have been dedicated to explain involved phenomena using ideal reactor models, such as plug flow reactors (PFR), continuously stirred tank reactors (CSTR) and lumped thermal reactors (LTR) [20,21,123,127,128].

For instance, as an attempt to demonstrate the existence of multiple steady states, bifurcation analyses considering CSTR, LTR and PFR reactor configurations have been reported by Vandewalle et al. [128]. The authors showed that only CSTR and LTR reactors present regions with multiple steady states and hysteresis, although the LTR reactor presented the best performance (higher CH_4 conversion with lower feed temperature). Although this study indicated the potential feasibility of autothermal operation, it must be noted that the considered reactor models present significant simplifications, as they neglect the occurrence of mass and energy radial gradients, and that validation of simulated autothermal conditions and resulting catalytic performance has yet to be confirmed experimentally. Therefore, further studies on this area are greatly needed, as previously pointed out by Sarsani et al. [127].

3.3.2. Modelling Approaches for Fluidized Bed Reactors

Fluidized bed reactors (FBRs) have been proposed as an alternative OCM reactor concept in order to facilitate the management of produced heat and avoid thermal runaway [112,113,129]. Additionally, according to Pannek and Mleczko [112], comparable or higher CH_4 conversions and C_2 selectivities could be achieved in a FBR when compared with the more usual PBR configuration, although these results could be strongly influenced by operational conditions.

To describe this reactor, as illustrated in Figure 16, one must observe that the gaseous stream flows through the bed in the emulsion in the form of bubbles. Pannek and Mleczko [112] considered a model which was based on the two-phase theory of fluidization and in accordance with the bubble assemblage model (BAM) [130], assuming a constant emulsion porosity.

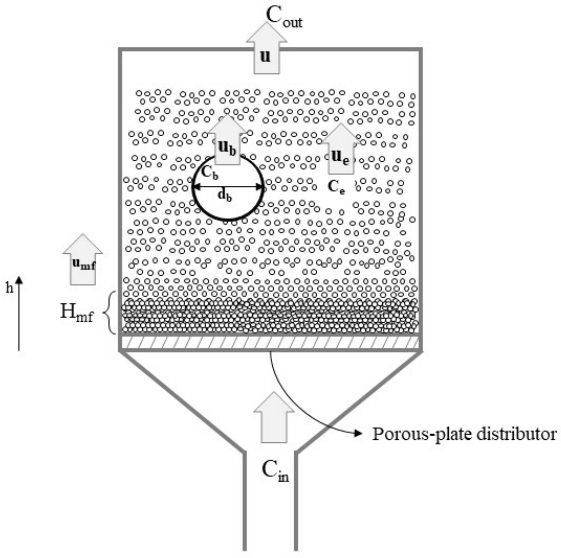

Figure 16. Illustration of a fluidized bed reactor [112].

The minimum fluidization velocity (u_{mf}), the bed height at minimum fluidized velocity (H_{mf}), the bubble diameter (d_b), bubble growth and bubble velocity were calculated with empirical correlations. The fluidized bed was discretised into several domains along the distance above the gas distributor, represented by h in Figure 16. In each of these domains the bubble and emulsion phases were modelled as perfectly mixed reactors. For the reaction network, both gas-phase [98] and catalytic surface reaction steps [131] were considered. Main model equations are briefly illustrated by Equations (9) and (10) [130], where F and f are the volumetric fraction of gas in the bubble and emulsion phases, respectively; C_i is the reactant concentration in phase i; D_i is the axial dispersion coefficient in phase i; u is the superficial gas velocity; F_0 is the gas interchange coefficient per unit of volume of gas bubble; F_s is the volumetric fraction of solid in the bubble phase; γ is the throughflow factor, which represents the flows through the emulsion phase; u_e is the superficial gas velocity in the emulsion phase; and the subscripts "b" and "e" represent the bubble and emulsion phases, respectively.

$$F\frac{\partial C_b}{\partial t} - FD_b\frac{\partial^2 C_b}{\partial h^2} + Fu\frac{\partial C_b}{\partial h} + F_0(C_b - C_e) + F_s\gamma = 0 \quad (9)$$

$$f\frac{\partial C_e}{\partial t} - fD_e\frac{\partial^2 C_e}{\partial h^2} + fu_e\frac{\partial C_e}{\partial h} + F_0(C_b - C_e) + f_s\gamma = 0 \quad (10)$$

Pannek and Mleczko [112] showed through simulations that C2 selectivities were affected by mass transfer limitations between the phases and that, as expected, C2 selectivities and yields can be a function of temperature and gas velocity.

In another study, computational fluid dynamics (CFD) simulation tools were used to study the reactor performance and reactions pathways [114]. In this case, the authors coupled the CFD description of fluid–solid flow with the ten steps of the catalytic reaction network, as proposed by Stansch et al. [92]. Their simulations were carried out using the Euler–Euler (EE) model approach based on the kinetic theory of granular flow. In the EE approach, both gas and solid phases are interpenetrating fluids [132]. For each gas and solid phase, the model comprises momentum conservation equations, which are linked by interphase momentum transfer, energy conservation equations, including a radiative heat transfer between the reactor wall and the feed, and mass conservation equations for each compound. The authors showed that their results of C_2 selectivity and methane conversion agreed well with available experimental data, and that mass transfer limitations between phases can significantly affect the reaction pathways.

3.3.3. Modelling Approaches for Membrane Reactors

Membrane reactor configurations, which can allow for the separation of CH_4 and O_2 feed streams, have attracted significant attention, as the limited contact between O_2 and CH_4 and achievable low oxygen concentrations can limit methane conversion, increasing selectivity to ethane and ethylene [113,115–117,124,133]. In this case, the reactor design comprises two concentric tubes that are separated by a membrane, as presented in Figure 17. The most common type of membranes used in OCM processes include porous and dense membranes. These two groups are subject to different gas permeation mechanisms, following the Knudsen diffusion and the mixed electron/ion conduction in porous and dense membranes, respectively [124]. In some cases, a catalyst is coated on the membrane wall and reaction occurs at the membrane surface, as illustrated in Figure 18.

Holst et al. [115] proposed a two-dimensional, pseudo-homogeneous model to describe the OCM packed-bed membrane reactor (PBMR), which used a generic ceramic membrane and a catalyst bed of La_2O_3/CaO. The model comprised steady-state mass, energy, and momentum balances, as illustrated by Equations (11)–(13), where boundary conditions accounted for the flux through the membrane for the reactor tube and shell (not shown) and the ten elementary steps of the reaction network developed by Stansch et al. [92] were used to represent the net reaction rates. In Equations (11)–(13), C_i is the concentration of reactant i; u_z is the superficial velocity in the z axis (Figure 18); D_r is

the effective diffusion coefficient in the r axis; $R_{i,j}$ is the reaction rate for component i in reaction j; T is the temperature; c_p is the heat capacity; λ_r is the heat transfer coefficient in the radial direction; ΔH_{Rj} is the reaction enthalpy of reaction j; P is the pressure; ρ_g and ε_k are the gas density and bed porosity, respectively; Re is the Reynolds number; and d_k is the catalyst pellet size.

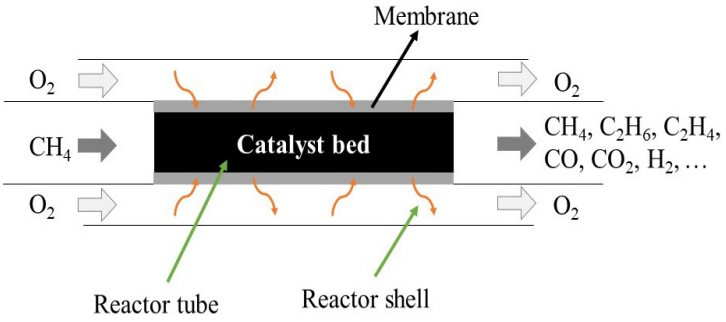

Figure 17. Membrane reactor configuration [133].

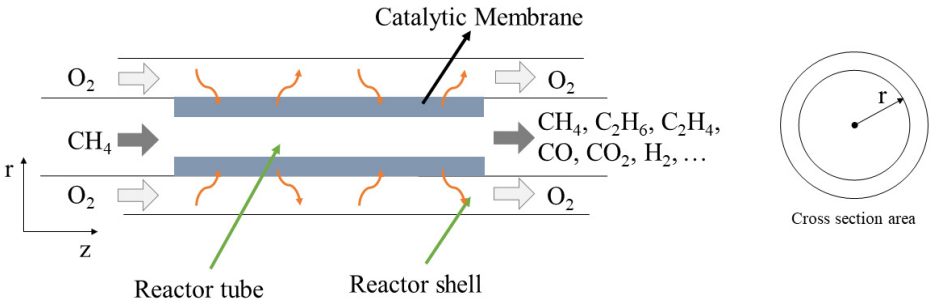

Figure 18. Catalytic membrane reactor configuration [115].

$$\frac{\partial C_i}{\partial z} = \frac{1}{u_z}\left[D_r\left(\frac{\partial^2 C_i}{\partial r^2} + \frac{1}{r}\frac{\partial C_i}{\partial r}\right) + \sum_j R_{i,j}\right] \tag{11}$$

$$\frac{\partial T}{\partial z} = \frac{1}{C_i c_p u_z}\left[\lambda_r\left(\frac{\partial^2 T}{\partial r^2} + \frac{1}{r}\frac{\partial T}{\partial r}\right) + \sum_j\left(-\Delta H_{R_j} R_{i,j}\right)\right] \tag{12}$$

$$\frac{\partial P}{\partial z} = -\frac{\rho_G u_z^2}{d_k}\frac{(1-\varepsilon_k)}{\varepsilon_k^3}\left[\frac{150(1-\varepsilon_k)}{\mathrm{Re}} + 1.75\right] \tag{13}$$

Good agreement between the experimental data and simulations was observed (for CH_4/O_2 feed molar ratio of 2, at 1.1 bar and inlet temperature of 750 °C) and the authors concluded that fast OCM reactions can cause concentration gradients due to oxygen depletion in the vicinity of the membrane [115].

Onoja et al. [117] proposed a different approach, where the optimisation of the axial thickness of the membrane was carried out to maximise the C_2 selectivity. A two-dimensional, steady-state model coupled with the kinetic mechanism proposed originally by Stansch et al. [92] was employed to describe mass and energy balances in the tube phase, in accordance with Equations (14) and (15).

$$u_{z-tube}\frac{\partial C_{i-tube}}{\partial z} = D_{er}\left(\frac{\partial^2 C_{i-tube}}{\partial r^2} + \frac{1}{r}\frac{\partial C_{i-tube}}{\partial r}\right) + \sum_j R_{i-tube,j} \tag{14}$$

$$u_{z-tube}\left(\sum_i\left(c_{p_i}C_{i-tube}\right)\right)\frac{\partial T_{tube}}{\partial z}=\left[\lambda_{er}\left(\frac{\partial^2 T_{tube}}{\partial r^2}+\frac{1}{r}\frac{\partial T_{tube}}{\partial r}\right)+\sum_j\left(-\Delta H_{R_j}R_{i-tube,j}\right)\right] \quad (15)$$

$$u_{z-shell}=\frac{\partial C_{i-shell}}{\partial z}=-\frac{4}{d_t}J_i \quad (16)$$

$$u_{z-shell}\left(\sum_i\left(c_{p_i}C_{i-shell}\right)\right)\frac{\partial T_{shell}}{\partial z}=\frac{4}{d_t}\left[U_a+\sum_i\left(c_{p_i}J_i\right)\right]\left(T_{tube}-T_{shell}\right) \quad (17)$$

Additionally, no reactions were assumed to take place in the membrane itself, which was based on its inherent contribution to mass and energy balances through the permeation flux, J_i, Equations (16) and (17), where C_i is the concentration of reactant i; $u_{z\text{-}tube}$ and $u_{z\text{-}shell}$ are the superficial velocity in the tube and shell, respectively; D_{er} is the effective bulk diffusivity of gas mixture; $R_{i,j}$ is the reaction rate for component i in reaction j; T is the temperature; c_p is the heat capacity; λ_{er} is the effective radial thermal conductivity; ΔH_{Rj} is the reaction enthalpy of reaction j; d_t is the tube diameter; and U_a is the overall heat transfer coefficient through the membrane.

In a first analysis, the authors compared the performance of a conventional packed-bed reactor (PBR) with the performance of a membrane reactor (MR) without varying the membrane thickness. Simulations performed at 1 bar and 800 °C indicated that larger catalytic bed lengths could be required in an MR to achieve similar methane conversion when compared with a PBR. However, a yield of 11.63% and C_2 selectivity of 47.86% were achieved in the MR in opposition to 8.28% and 29.86%, respectively, obtained with the PBR. By using the variable thickness membrane reactor (VTMR) configuration, C_2 selectivities and yields of nearly 60% and 14% could be achieved, respectively. Interestingly, these authors have also shown how the VTMR could allow for the minimisation of hot spot formation, as the increase in membrane thickness along the axial direction could contribute to managing O_2 permeation flux and its consumption rate, resulting in a smoother axial temperature profile when compared to MR and PBR configurations, as illustrated in Figure 19 [117]. However, although these results seem very promising, simulations have yet to be validated by experimental observations.

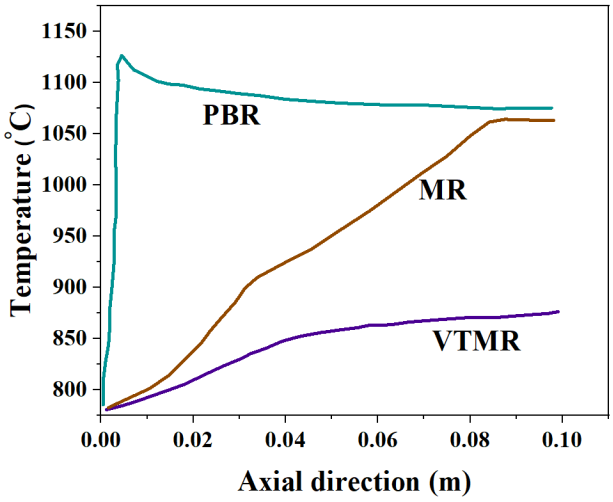

Figure 19. Simulated temperature profiles for PBR, MR and VTMR in adiabatic operation (adapted from [117]).

Furthermore, although membrane reactors seem quite attractive for OCM due to their higher C_2 selectivity and the reduction in inlet air separation costs, some drawbacks should be noted, such as the costs associated with the use of membranes, difficulties in reaction heat management, the appropriate sealing of membrane packs and the membrane

long-term stability. In addition, membrane catalytic activity can itself become a limiting factor for OCM yields [124].

3.4. Thermal Effects

As discussed in the previous sections, OCM reaction networks and associated kinetic constants estimated for packed-bed reactors have been mostly obtained assuming the occurrence of negligible temperature gradients in the catalytic bed. However, it has been shown experimentally that this assumption is hardly achieved due to the formation of hot spots [134–136]. Typically, a fast increase in temperature is observed as CH_4 and O_2 enter the reactor, due to fast rates of exothermic oxidation reactions, as illustrated in Figure 20. As O_2 is consumed along the reactor length, temperature tends to stabilise [91,135]. The difference between the nominal reactor temperature and the maximum axial catalytic bed temperature in PBRs has also been shown to depend on both the inlet gas flow composition and gas flow velocity [134,135], as shown in Figure 20.

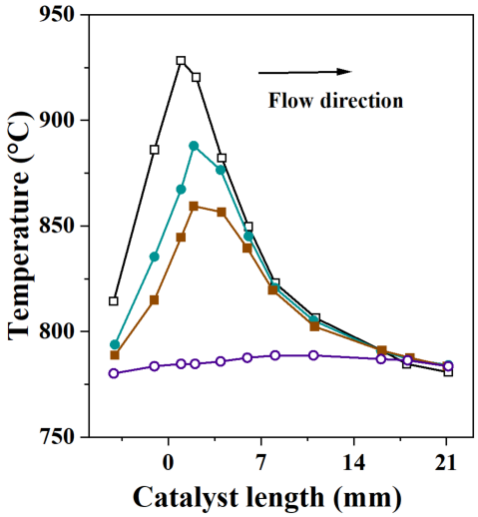

Figure 20. PBR axial temperature profile as a function of catalytic bed reactor (1.0 mL) length measured over a $Mn/Na_2WO_4/SiO_2$ catalyst at CH_4/O_2 feed molar ratio of 5 (□), 7 (●), and 10 (■) [134]. Open circles (○) represent profiles obtained when only O_2 was fed into the reactor.

To minimise the effects associated with hot spots in packed-bed reactors, efforts have been dedicated to evaluate strategies for heat management, including the dilution of the feed stream with inert gases [136] and water steam [137], and the dilution of the catalytic bed with inert solids [16]. However, the effectiveness of these strategies and their economic implications at actual high-pressure industrial operation conditions must still be evaluated.

4. Thermodynamic Considerations

This section presents a detailed analysis about the behaviour of OCM mixtures at equilibrium conditions. Although previous reports have discussed thermodynamic aspects of the OCM reaction system [138], there has been no extensive evaluation of equilibrium compositions in a wide range of reaction conditions, taking into account the impact of pressure, CH_4/O_2 feed molar ratio, temperature, the presence of inert gases, and the co-feeding of ethane, CO_2 and H_2O on the resultant thermodynamic ethene yield. For instance, Geerts et al., (1990) [138] reported the equilibrium thermodynamics of methane pyrolysis and its oxidation, presenting equilibrium compositions for the OCM reaction as cumulative molar fractions for different temperatures at a single fixed condition of CH_4/O_2 feed molar ratio and pressure.

More recently, Gibbs energies for four global oxidative reactions at 800 °C and 1 atm have been reported [139], highlighting their negative magnitudes and therefore their thermodynamic feasibility. Equilibrium carbon-based selectivity distributions for different

CH_4/O_2 feed ratios at 800 °C and 1 atm in the presence [57] and the absence [139] of solid graphite formation have also been considered, indicating the formation of coke as predominant at high CH_4/O_2 feed ratios (above 4), while CO was the most favoured carbon-containing gaseous product. Similarly, equilibrium molar-based selectivity distributions for a large range of temperatures, at 1 bar and CH_4/O_2 feed molar ratio equal to 9 [140] and 4 [21], have also been discussed, illustrating the high thermodynamic compositions of H_2 and CO obtained at typical OCM temperatures between 700 and 1000 °C.

Thermodynamic constraints also impose the maximum conversion that can be achieved at a certain condition of temperature, pressure and initial reactants composition [141]. Thus, it is possible to estimate the maximum yield of a desired product that can be obtained at the ideal selectivity reached under the kinetic regime. In this aspect, efforts have been dedicated to estimate an upper bound for the C2 yield [18,142], given the importance of this information for analysing the economic feasibility of the industrial OCM process implementation.

Surprisingly, and to the best of our knowledge, no upper bound based exclusively on thermodynamic constraints has been discussed in a wide range of reaction conditions. Thus, this section aims to expand the current understanding on the equilibrium behaviour of the OCM system by assessing the impact of pressure, CH_4/O_2 feed molar ratio, temperature, the presence of inert content, and the co-feeding of ethane and CO_2 on the resulting thermodynamic ethene yield. As thermodynamic effects may also affect kinetic regimes to some extent, through, for instance, equilibrium constants within reaction rate equations, we hope to shed more light into the understanding of this complex reaction system.

Thermodynamic calculations were performed with help of the Gibbs energy minimisation method, using the '*GPREC—Gas-phase reaction equilibrium calculator*' [143] and the '*ThermoSolver*' software version 1.0 [144]. Unless otherwise stated, yields and selectivities have been defined in carbon bases (see Section S1 in the Supplementary Materials) and equilibrium compositions have been investigated assuming the presence of eight compounds, which included CH_4, O_2, CO, CO_2, H_2, H_2O, C_2H_6, and C_2H_4. As will be shown later, the formation of additional compounds, such as propene, propane and acetylene, can be neglected at the equilibrium due to their low thermodynamic yields. In addition, this study also neglected the formation of coke to calculate the maximum achievable thermodynamic yield. Table S1 in the Supplementary Materials summarises standard Gibbs energies in increasing order at 900 °C and standard reaction enthalpies for possible global OCM reactions, which will be further discussed in the following sections.

4.1. The Effect of Temperature and CH_4/O_2 Feed Ratio on Equilibrium Compositions

The effect of temperature and CH_4/O_2 feed molar ratio at 1 bar is illustrated in Figure 21a–f, where the ethene yield (a), CH_4 conversion (b), and carbon-based selectivity for C_2H_4 (c), CO (d) and CO_2 (e) are plotted as functions of temperature between 700 and 950 °C for CH_4/O_2 feed molar ratios ranging between 1.5 and 9. In the present study, the CH_4/O_2 feed molar ratio was varied while keeping the total number of mols of reactants constant.

As one can see in Figure 21a, the thermodynamic temperature window for ethene production lies above 700 °C, with ethene yields increasing with the continuous increase in temperature and CH_4/O_2 feed molar ratio. Similar behaviour is verified for the combined ethene and ethane yields, presented in Figure S1 of the Supplementary Materials. In contrast, CH_4 conversion presents only a slight increase with the increase in temperature for the same CH_4/O_2 feed molar ratio, Figure 21b, while a more pronounced reduction in conversion is observed with the continuous increase in the CH_4/O_2 feed molar ratio. Thus, higher ethene yields observed with the continuous increase in temperature for a fixed CH_4/O_2 feed molar ratio should result from a change in the product's selectivity distribution, as illustrated in Figure 21c–e. Indeed, as temperature is increased, exothermic oxidation reactions that lead to CO and CO_2 formation are unfavoured, while the endothermic dehydrogenation of ethane can be promoted (Table S1). It is also interesting to note the

complex behaviour of CO selectivity, which presents a point of maximum as a function of temperature that also depends on the CH_4/O_2 feed molar ratio, Figure 21d. For higher feed oxygen contents (CH_4/O_2 feed molar ratios smaller than 3), CO selectivity increases with temperature, whereas at lower oxygen contents, the selectivity is reduced. In this case, the less exothermic character of oxidation reactions that lead to CO, when compared to the ones that lead to CO_2, plays a role: as CO_2 formation is more largely unfavoured with the temperature increase, the CO selectivity can increase.

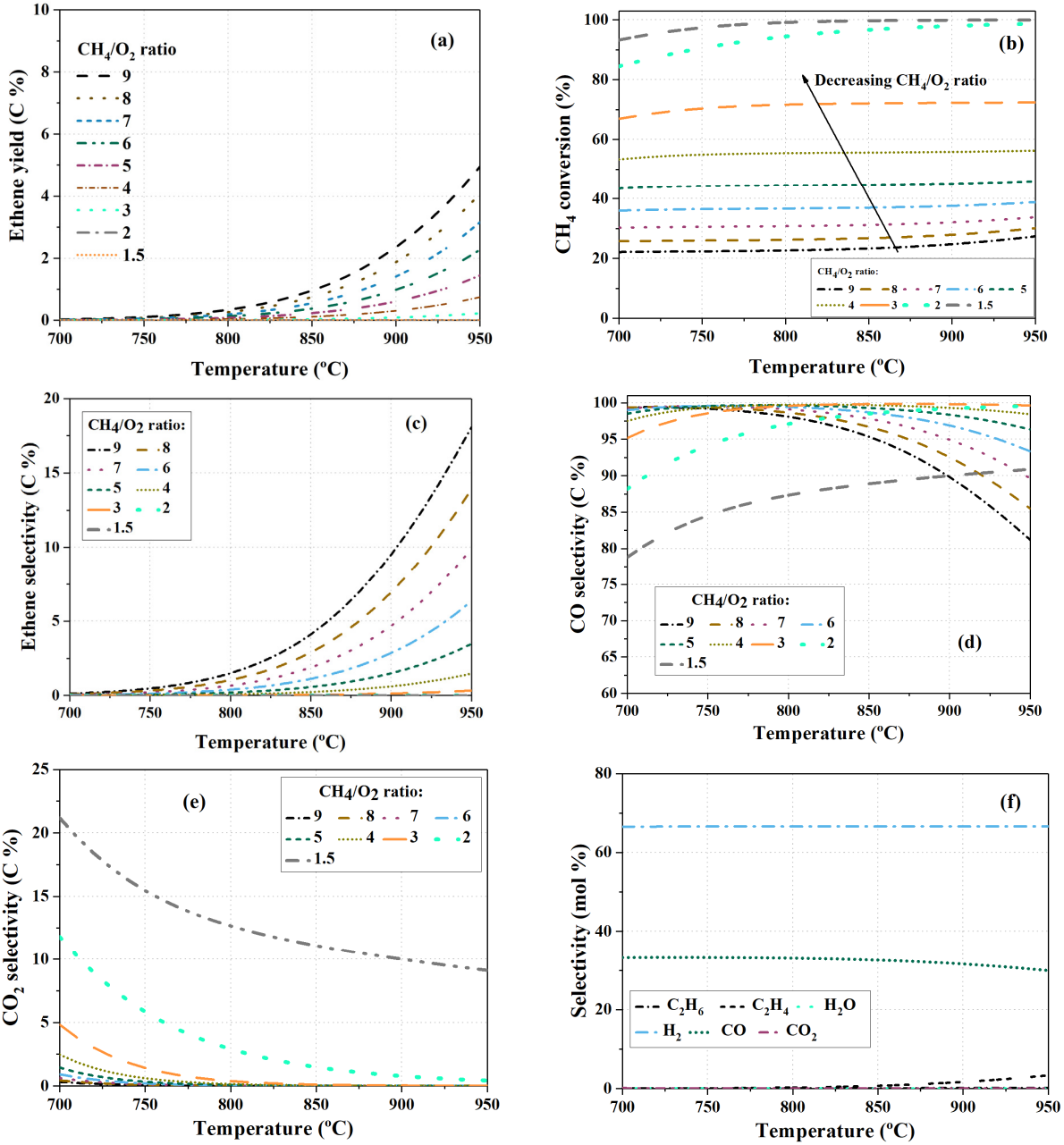

Figure 21. Effect of the CH_4/O_2 feed ratio and temperature at 1 bar on the ethene yield (**a**), CH_4 conversion (**b**), carbon-based selectivity for C_2H_4 (**c**), CO (**d**), and CO_2 (**e**), and molar-based selectivity distribution at the CH_4/O_2 feed molar ratio of 9 (**f**). Feed composition contained CH_4 and O_2 only and was varied while keeping the total number of added mols constant.

Figure 21f also illustrates the molar-based selectivity distribution at the CH_4/O_2 feed molar ratio equal to 9 at 1 bar as a function of temperature. As previously pointed out [21,140], thermodynamic equilibrium does not favour ethene production in the OCM

reaction network, as CO and H_2 are the most favoured gaseous products, stressing the need for the process to operate under a kinetic regime.

4.2. The Effect of Inert Dilution and Pressure

The effect of feed composition dilution and pressure at 900 °C is illustrated in Figure 22a–c, where CH_4 conversion (a), ethene yield (b) and carbon-based selectivity distribution (c) are presented as functions of the inert composition. In the present study, the CH_4/O_2 feed molar ratio was kept constant and equal to 9, while also keeping constant the total number of mols in the feed. Thus, the increase in the inert content could also be translated as the reduction in the partial pressures of CH_4 and O_2.

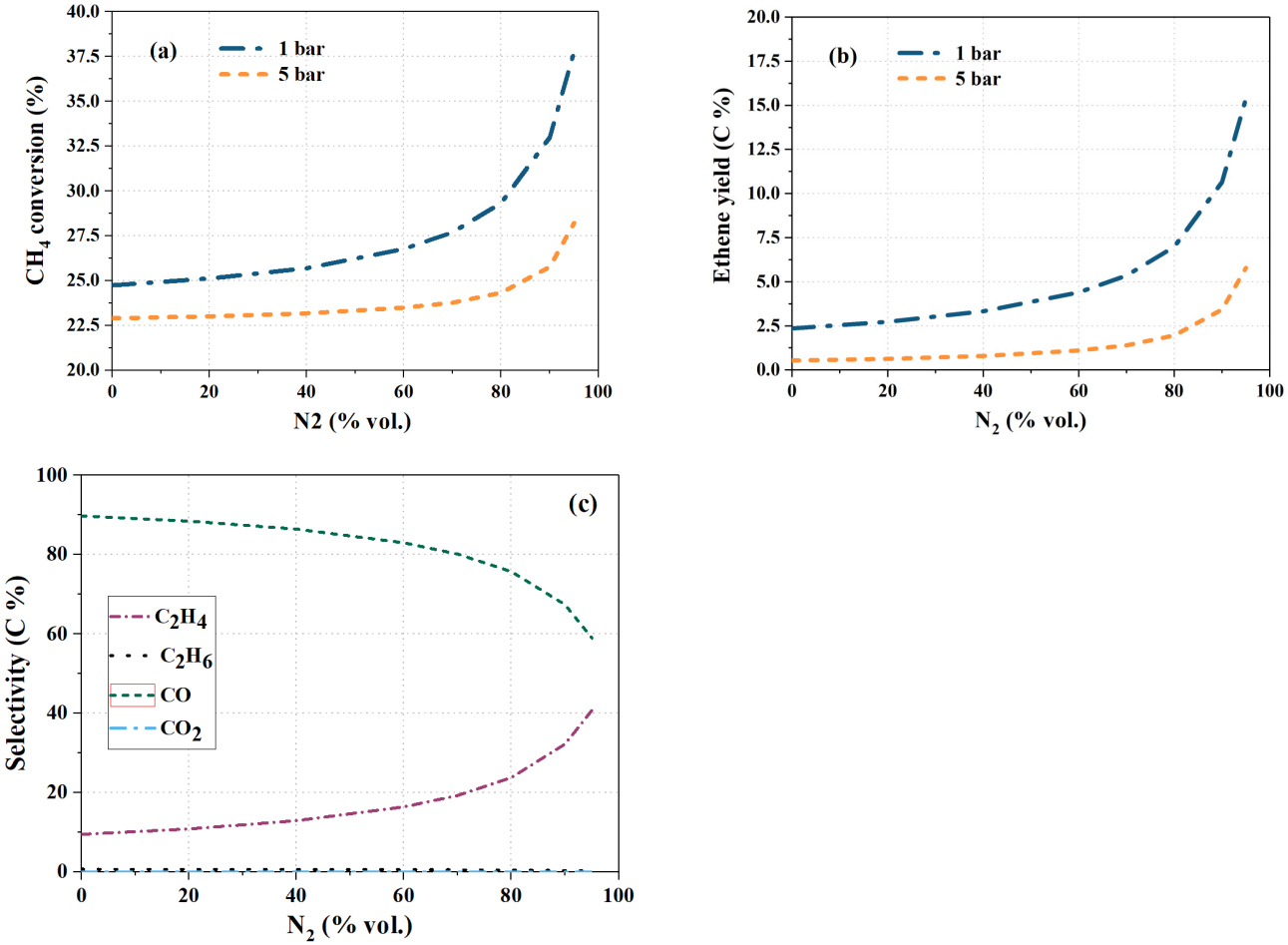

Figure 22. Effect of the inert composition and pressure at the CH_4/O_2 feed ratio equal to 9 and 900 °C on the methane conversion (**a**); ethene yield (**b**); and carbon-based selectivity distribution at 1 bar (**c**). Feed composition comprised CH_4, O_2 and N_2 only and inert composition was varied while keeping the total number of added mols and the CH_4/O_2 feed ratio constant.

Higher inert contents promote CH_4 conversion, Figure 22a, resulting in larger ethene yields, Figure 22b, while also increasing ethene carbon-based selectivity, Figure 22c. The increase in conversion with more diluted feed compositions can be more easily understood when the stoichiometry of OCM reactions is considered, as illustrated in Table S1. In this case, the higher number of mols among most reactions products favours the forward reaction at higher inert contents, as the probability of molecular collisions among the smaller number of reactant mols is higher when compared to the number of collisions required for the backward reaction [141]. This very same molecular explanation can be used

to explain the reduction in CH_4 conversion at higher total pressure conditions (Figure 22a) as the backward reaction direction is promoted in this case.

In line with the above discussion, the change in the distribution of carbon-based products selectivity with the inert content can be related to the favouring of ethane dehydrogenation at more diluted conditions. A similar behaviour of the products selectivity distribution can be verified at 5 bar (not shown) when the inert content is changed, exhibiting, however, a less pronounced change in CO and ethene selectivity, which changed from 96.8 and 2.3% in the absence of N_2 to 79 and 21% in the presence of 95% of the inert in the feed, respectively.

It is interesting to note that the effect of an inert composition agrees with kinetic observations in respect to ethene selectivities (Figure 11), as lower CH_4 and O_2 partial pressures promote ethene selectivity. However, the thermodynamic effect of total pressure on CH_4 conversion is contrary to the effect observed under a catalytic kinetic regime. In this case, higher total pressures lead to increased methane conversions (respecting thermodynamic limits), likely due to increased rates of gas-phase reaction rates.

4.3. The Combined Effect of Temperature, CH_4/O_2 Feed Ratio and Inert Composition

The effect of operation variables including temperature, CH_4/O_2 feed molar ratio and inert composition on equilibrium compositions was combined in Figure 23, where ethene yields are plotted as a function of methane conversion. In this figure, each line connected by geometric symbols represents a condition of equal temperature and inert composition, while values of ethene yield and methane conversion are changed as a result of different CH_4/O_2 feed molar ratios, represented by the diagonal straight lines.

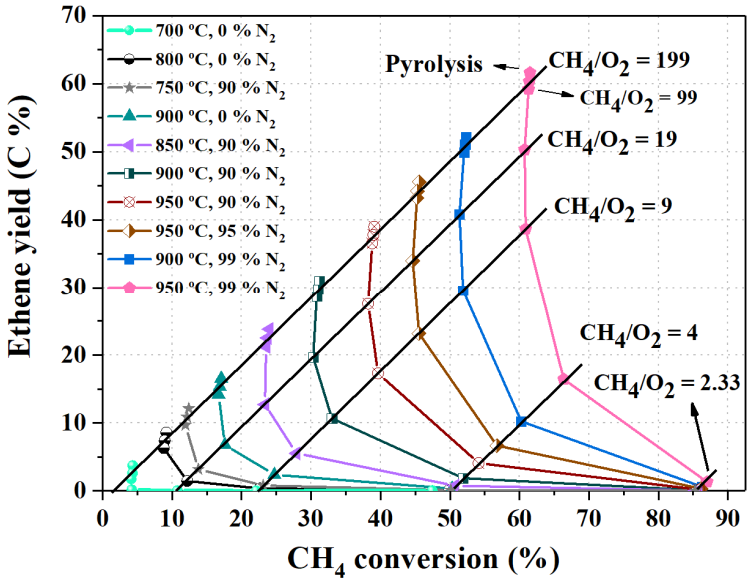

Figure 23. Thermodynamic ethene yield as a function of CH_4 conversion at 1 bar and different conditions of temperature, CH_4/O_2 feed molar ratio and inert concentration. Feed composition was varied while keeping the total number of mols of reactants constant.

For the same temperature and inert composition, higher thermodynamic ethene yields are achieved as the O_2 content is decreased, despite the resulting lower methane conversions. As the O_2 is reduced, oxidation reactions involving O_2 can be suppressed, leading to an increase in the ethene selectivity, as previously illustrated in Figure 21c. Figure 23 illustrates that the maximum achievable thermodynamic ethene yield at each condition of temperature and inert composition is closely related to the point at which methane conversion can be performed solely by pyrolysis, assuming no coke formation, as previously reported [138], as in this case the undesirable formation of CO and CO_2 can be avoided.

While Figure 23 illustrates how the thermodynamic ethene yield is limited by CH_4 conversion as the O_2 content is reduced, one should also note that even in an ideal scenario where OCM reactions can be performed and simultaneously suppress coke, CO and CO_2 formation, the thermodynamic ethene yield would still be limited by CH_4 conversion, as illustrated in Figure 24.

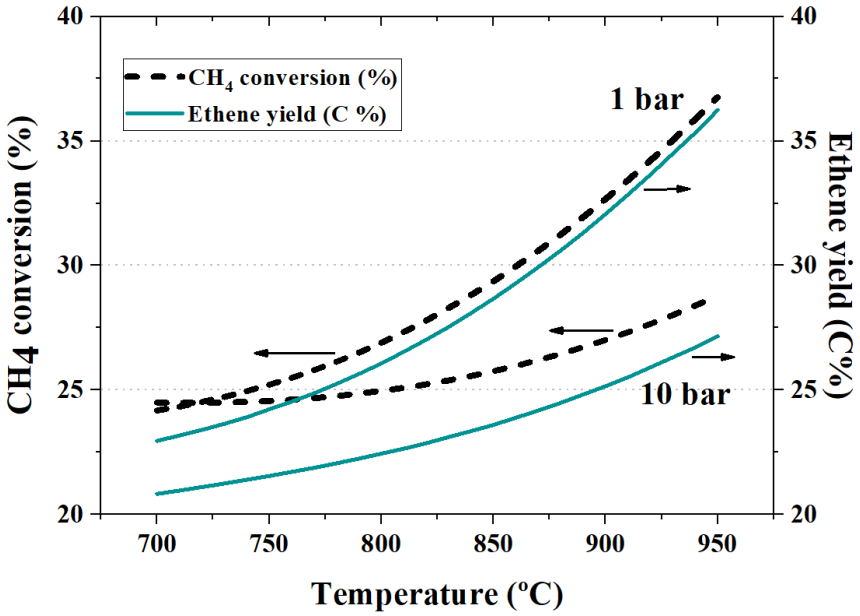

Figure 24. Thermodynamic CH_4 conversion and ethene yield as a function of temperature at the CH_4/O_2 feed molar ratio equal to 9, and pressures of 1 and 10 bar. Equilibrium composition was calculated assuming the presence of the following six compounds: CH_4, O_2, H_2, H_2O, C_2H_6 and C_2H_4.

Figure 24 illustrates methane conversions and ethene yields as functions of temperature at 1 and 10 bar, calculated by assuming a reactant feed composition comprising only CH_4 and O_2 at the CH_4/O_2 feed molar ratio equal to 9, and assuming the presence of six compounds, which included CH_4, O_2, H_2, H_2O, C_2H_6 and C_2H_4. As the formation of CO and CO_2 was assumed to be null, the difference between CH_4 conversion and ethene yield represents the yield towards ethane (not shown). As one can see, even in this case methane conversions are far from 100%.

4.4. Effect of Co-Feeding Ethane and CO_2

Several works have investigated the kinetic aspects of separately co-feeding ethane and CO_2 along with CH_4 and O_2 mixtures in the OCM reactor, either in the presence or absence of heterogeneous catalysts [99,145]. This section evaluates the thermodynamic benefits and drawbacks associated with these approaches.

4.4.1. Co-Feeding of Ethane

It has been shown that the addition of C_2H_6 into the CH_4 and O_2 feed mixtures can lead to an increase in ethene yields both in the presence and absence of catalyst, with the increase being more pronounced when ethane dehydrogenation is performed without any catalyst [99,145]. However, while ethene yield is increased, CH_4 conversion is reduced and can even cease in the presence of catalyst, while it can slightly increase in its absence, depending on the ethane composition [99,145]. Thus, the present study also evaluated the thermodynamics effect of co-feeding ethane into the OCM reactor in a wide range of operational conditions.

As illustrated in Figure 25a,b, which presents ethene yield as a function of temperature at a CH_4/O_2 feed molar ratio equal to 9 and pressure of 1 (a) and 10 (b) bar for different ethane feed compositions ranging between 0 and 30 mol%, the co-feeding of ethane increases thermodynamic ethene yields in significant amounts.

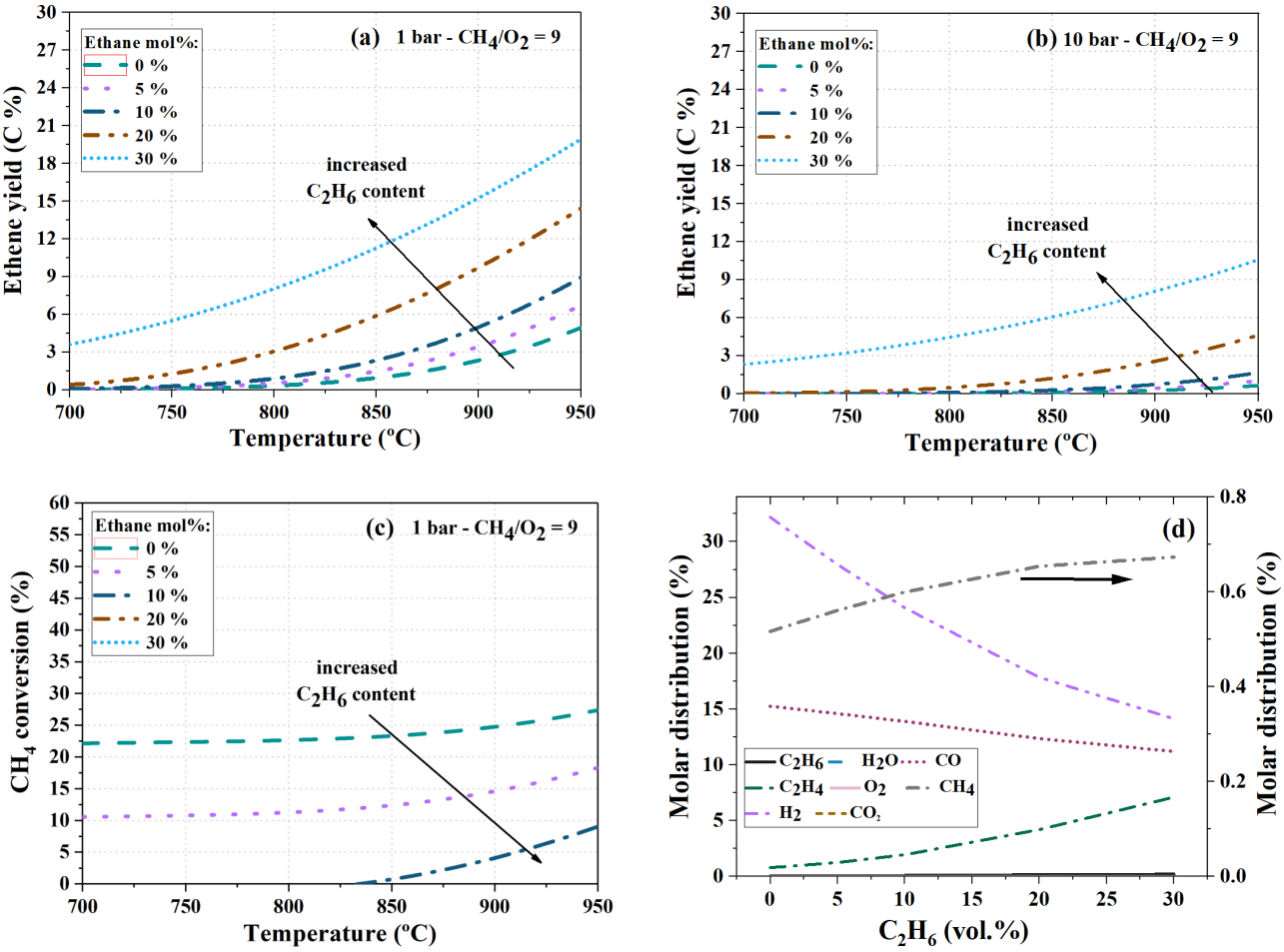

Figure 25. Effect of co-feeding C_2H_6 on: (**a**,**b**) carbon-based C_2H_4 yield as a function of temperature at the CH_4/O_2 feed molar ratio equal to 9 and pressure of 1 (**a**) and 10 (**b**) bar; (**c**) CH_4 conversion as a function of temperature at the CH_4/O_2 molar feed ratio equal to 9 and pressure of 1 bar; and (**d**) equilibrium molar distribution as a function of C_2H_6 feed composition at 900 °C, 1 bar and CH_4/O_2 molar feed ratio equal to 9. C_2H_6 composition in the feed was varied while keeping the total number of mols and the CH_4/O_2 feed molar ratio constant. C_2H_4 yield was calculated considering both CH_4 and C_2H_6 in the feed (see Equation (A5) in the Supplementary Materials).

While CH_4 and C_2H_6 as reactants can compete for O_2, leading to a reduction in the CH_4 conversion, as illustrated in Figure 25c, both ethane oxidation and pyrolysis can produce CH_4 [146], resulting in the net increase in the CH_4 composition with the ethane feed composition, as illustrated in Figure 25d (right axis), and, thus, in artificially negative methane conversion values, purposely omitted in Figure 25c. Figure 25d also illustrates the equilibrium molar distribution among remaining compounds as a function of ethane feed composition at 900 °C, 1 bar and CH_4/O_2 molar feed ratio equal to 9, where both CO and H_2 compositions are reduced at higher ethane feed composition conditions. While the reduction in CO composition can be associated with the preferential ethane oxidation, which can reduce O_2 availability for oxidising CH_4, the reduction in H_2 composition can be either associated with its consumption in reactions involving the formation of CH_4 or its lower production through ethane dehydrogenation.

4.4.2. Co-Feeding of CO_2

Research has long aimed to evaluate the potential feasibility of recycling OCM produced CO_2 into the catalytic OCM reactor. As discussed in the previous section, the co-feeding of CO_2 with CH_4 and O_2 mixtures over catalytic OCM reactors has been demonstrated to result in significantly lower methane conversions and ethene yields, a fact usually associated with the competitive adsorption of CO_2 and O_2 on catalyst active sites [92,102,147,148]. However, it has also been suggested that the co-feeding of CO_2 can play a role in improving catalyst stability [147] and even present a positive impact on ethene yield, either through its interaction with the catalyst surface [28] or by enabling changes in CH_4 and O_2 diffusivities when used as a diluent, which could create local environments of higher CH_4/O_2 molar ratios within the catalyst bed [149]. Indeed, in an excellent review covering the advances in catalyst development for the CO_2-OCM process [150], the authors summarise how different reducibility features from catalytic systems, such as CeO_2/ZnO and $SrMnO_{2.5}$ oxides, could result in improved performances in C2 formation. In this mechanism, CO_2 would decompose at the catalyst surface, forming CO and an oxygen active site, and this step would involve CO_2 oxidising a reduced metal, such as Zn^{+1} or Mn^{2+}.

Despite previous works on the thermodynamic aspects of methane dry reforming [151], involving reactant mixtures of CH_4 and CO_2, which indicated the preferential thermodynamic production of CO and H_2 over ethene and ethane, to the best of our knowledge, the effect of CO_2 co-feeding with CH_4 and O_2 mixtures on thermodynamic ethene yields in a wide range of OCM operational conditions has not been reported. Thus, one objective of the present study was the investigation of the thermodynamic effects of CO_2 co-feeding.

Figure 26a shows thermodynamic ethene yields as a function of temperature at 1 bar for different feed mixtures of CO_2, CH_4 and O_2, where the CO_2 composition was varied between 0 and 30 mol% while the CH_4/O_2 molar ratio was kept constant and equal to 9. As one can see, the use of CO_2 as a diluent results in lower thermodynamic ethene yields, driven by a shift in the products selectivity distribution, as illustrated in the molar composition distribution at 900 °C in Figure 26c, towards the increased formation of CO and H_2, which also can boost thermodynamic CH_4 conversions, as illustrated in Figure 26b. Thus, while CO_2 recycling can be favourable for the production of synthesis gas (as previously stated [151]), any observed positive effects of CO_2 co-feeding on ethene yields should not result from thermodynamic effects.

4.5. The Importance of Considering Additional Products on Equilibrium Compositions

The effect of the operation variables temperature, pressure, inert composition, CH_4/O_2 feed ratio and co-feeding on equilibrium compositions has so far been analysed assuming the existence of eight compounds: CH_4, O_2, CO, CO_2, H_2, H_2O, C_2H_6, and C_2H_4. In this section, this group is expanded in order to assess the impact of the formation of additional compounds, including propene, propane and acetylene, on equilibrium compositions, as these compounds have been reported as constituents in stream flows, exemplifying the outlet of OCM reactors designed to produce up to 1000 kt per year of polymer-grade ethylene [152].

As illustrated in Figure 27, no significant changes in CH_4 conversions and C_2H_4 selectivities could be verified after the inclusion of propane, propene, and acetylene in the thermodynamic calculations, as these compounds are not favoured at equilibrium. Therefore, previously observed operational variable effects can be considered the same when these compounds are present in the reacting system as co-products.

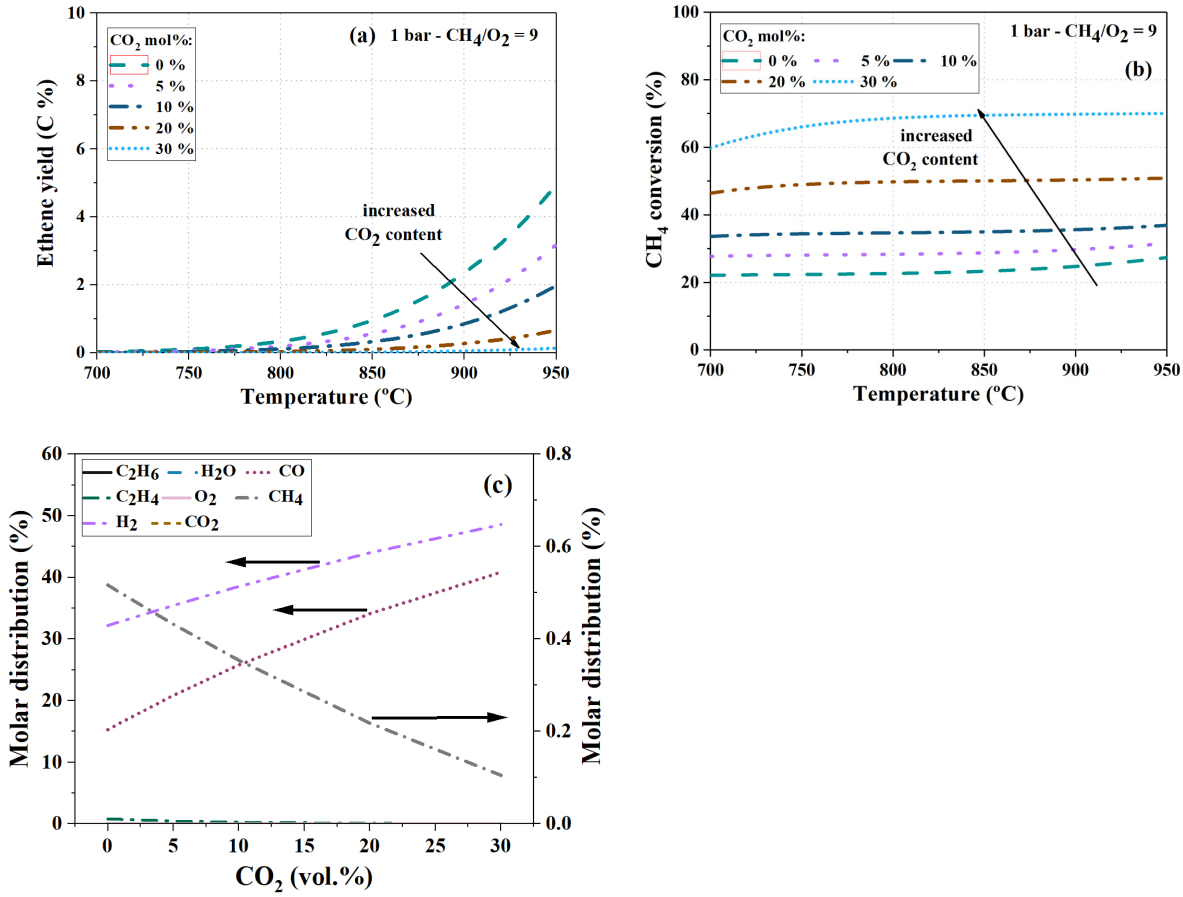

Figure 26. Effect of co-feeding CO_2 on carbon-based ethene yield (**a**) and CH_4 conversion (**b**) as a function of temperature at the CH_4/O_2 molar feed ratio equal to 9 and pressure of 1 bar; and (**c**) equilibrium molar distribution as a function of CO_2 feed composition at 900 °C, 1 bar and CH_4/O_2 molar feed ratio equal to 9. CO_2 composition in the feed was varied while keeping the total number of mols and the CH_4/O_2 feed molar ratio constant. Ethene yield was calculated considering both methane and CO_2 in the feed.

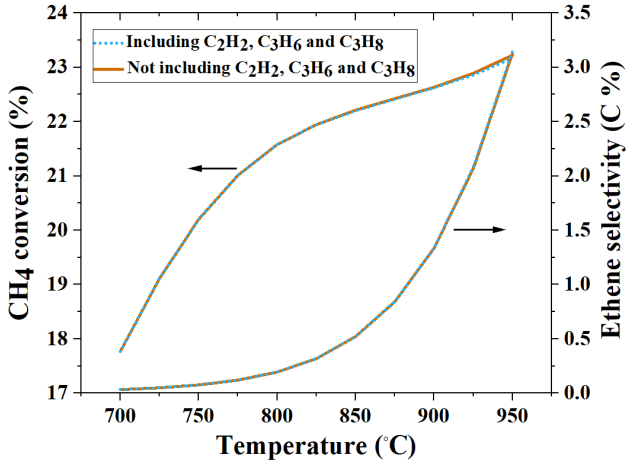

Figure 27. CH_4 conversion and C_2H_4 selectivity (in C%) as a function of temperature at 9 bar and CH_4/O_2 feed molar ratio of 9. Reactant composition comprised CH_4 and O_2 only. Equilibrium compositions were calculated assuming the initial group of eight compounds (including CH_4, O_2, CO, CO_2, H_2, H_2O, C_2H_6, and C_2H_4) and an expanded group containing eleven compounds in which propane, propene and acetylene were added.

5. Active OCM Catalysts

According to the generally accepted kinetic mechanism, the main role of a catalyst in ethene formation is to assist the generation of methyl radicals, $CH_3^{\bullet}$, by either homolytic or heterolytic C-H bond cleavage in the CH_4 molecule [109], as illustrated in Figure 28.

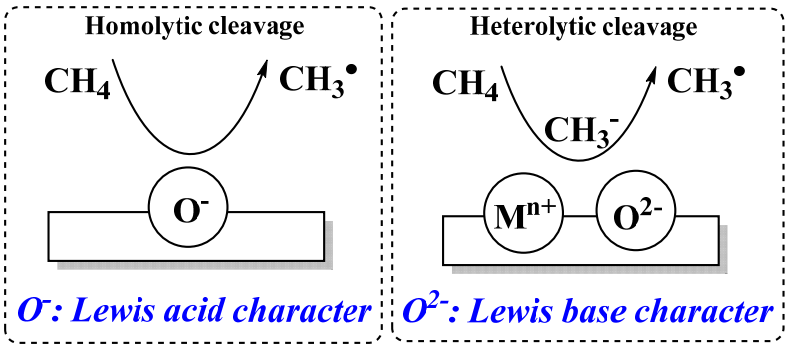

Figure 28. Simplified illustration of CH_4 activation via homolytic and heterolytic routes involving different active sites on a metal oxide catalyst surface.

The activation of methane via homolytic scission is believed to involve O^- active species, which act as Lewis acid [29,109]. These active species can be created by either the doping of metal oxides with dopants capable of promoting the creation of lattice oxygen vacancies, which may enable the formation of O^- species in the vicinities of O^{2-} lattice oxygen, and/or by the adsorption of molecular oxygen on Lewis base centres on the catalyst surface, which can lead to the formation of electrophilic O^- species depending on the amount of charge exchanged [107,109]. Unfortunately, the adsorption of molecular O_2 can also lead to the formation of weakly bounded nucleophilic O_2^- species, believed to be involved in the conversion of CH_4, C_2H_6 and C_2H_4 to oxygenated compounds [109,153]. On the other hand, CH_4 activation via a heterolytic route would involve a Lewis acid–base pair centre on the catalyst surface, such as $M^{2+}-O^{2-}$, resulting in the formation of a hydroxyl group and a methyl anion, which would then desorb as a methyl radical after losing an electron. Moreover, the catalyst surface would also be involved in radicals quenching by promoting termination reactions which reduce the concentration of radicals, leading to unselective pathways [93].

While the mechanism and nature of active sites is still in debate, as illustrated by the fact that several catalyst properties, such as surface oxide reducibility [154], acid–base properties [28,155], metal oxide–support interactions and morphology, may play an important role in C2 formation, as recently reviewed [156]. This section aims to quantitatively review and compare the catalytic performances of OCM heterogeneous catalysts. By focusing on quantitative aspects of catalytic performance, we hope to provide an overview that can contribute to future analyses of OCM economic viability at an industrial scale. Catalysts in this section have been organised in terms of the number of metals that constitute the oxide. Thus, it will be shown in the next sections that there are many different metal combinations which are OCM active.

5.1. Monometallic Oxides

Many single metal oxides have demonstrated OCM activity, including MgO, CaO, BaO, SrO, Al_2O_3, Fe_2O_3, Sm_2O_3, La_2O_3, Nd_2O_3, ZrO_2, Nd_2O_3, Nb_2O_5 and Gd_2O_3. Their efficiency in activating CH_4 and O_2 has been correlated with their surface acid–base and/or redox properties [67,110].

In order to better understand the relationship between single oxides basicity and their OCM activity, La_2O_3, Nd_2O_3, ZrO_2, and Nb_2O_5 were evaluated individually by Kús et al. [110]. These authors found La_2O_3 and Nd_2O_3 oxides to be more active and C2 selective when compared to ZrO_2 and Nb_2O_5. The results were well correlated with

the total basicity of the evaluated catalysts, which was measured by CO_2 temperature-programmed desorption (CO_2-TPD) experiments and by reactions of 2-butanol conversion. Interestingly, La_2O_3 presented the highest total basicity, CH_4 conversion and C2 selectivity. More recently, a comparison among single lanthanoid oxides further confirmed the findings of Kús et al. [110,157].

C2 selectivity over monometallic oxides can be observed to fluctuate around 32.3 ± 1.5%, as illustrated in Figure 29a, while C2 yield and CH_4 conversion vary and reach up to approximately 14 and 40%, respectively. In this figure, 54 experimental data points for C2 yields as a function of CH_4 conversion, collected over monometallic oxide catalysts, including MgO, CaO, BaO, SrO, Al_2O_3, Fe_2O_3, Sm_2O_3, La_2O_3, Nd_2O_3, ZrO_2, Nd_2O_3, Nb_2O_5 and Gd_2O_3, at different OCM reaction conditions [110,111,158–163], indicate that despite differences in catalyst chemical composition, an average selectivity could be calculated. Obviously, while a linear increase in yield with conversion was expected, a similar average slope among catalysts with different catalytic properties could indicate that effects other than kinetics could be limiting catalytic performance.

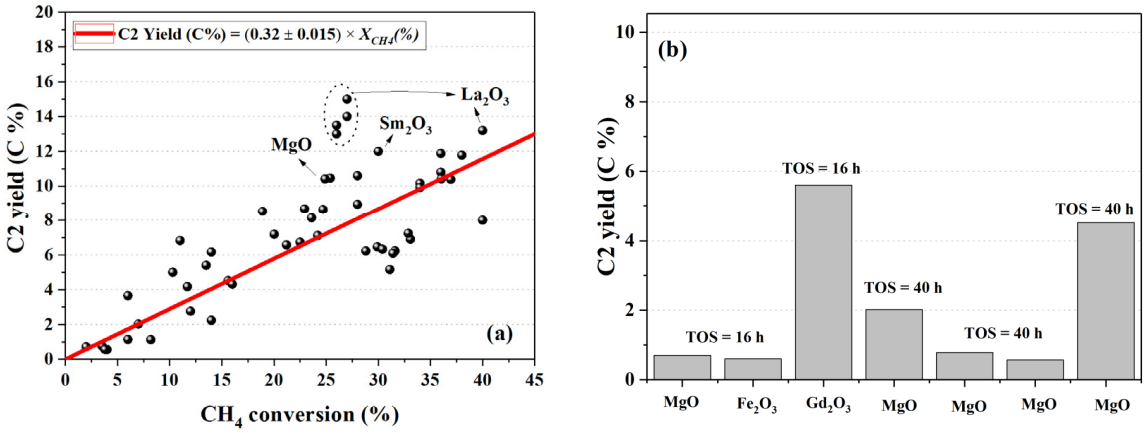

Figure 29. C2 yields as a function of CH_4 conversion over monometallic oxides (**a**) and C2 yields for different catalysts after reaction times (time on stream (TOS)) longer than 16 h (**b**). Data sourced from [110,111,158–163]. Dashed circle indicates data from La_2O_3 nanowires [163].

Moreover, Figure 29b summarises C2 yields obtained after reaction times longer than 16 h, suggesting that the assessment of thermal stability among different monometallic oxides deserves further attention. For instance, Arndt et al. [111] demonstrated how different catalyst preparation methodologies could significantly impact the thermal stability of obtained oxides, which despite presenting similar selectivities to C2, could be more active for longer.

5.2. Bimetallic Oxides

Alkali-metal-doped basic oxides have shown promising catalytic performance for C2 selectivities in the OCM process. However, the evaporation of alkali metals at high temperature is reported as a cause of catalyst deactivation [164]. For instance, Li-doped MgO (Li/MgO) oxide has been a classic catalyst used in OCM reaction studies [102,103,165], this system receiving great attention due to its high initial selectivity and activity towards C2 compounds [52]. However, its stability has been proved to be limited due to Li volatility [106,111].

In an attempt to improve the thermal stability of Li-doped MgO catalysts, different catalyst preparation procedures have been investigated, using different lithium loadings [111]. However, regardless of the synthesis preparation method, catalyst activity has been observed to significantly reduce with reaction times, resulting in recommendations against the use of Li/MgO systems for industrial applications.

The doping of CaO with alkali metals has also been reported to improve the catalytic performance towards C2 compounds when compared with the single oxides (including Li-CaO, Na-CaO, K-CaO, Rb-CaO, Cs-CaO) [164]. These authors further investigated the effect of the doping metal composition on the catalytic performance, by testing two alkali metal to Ca ratios, as illustrated in Figure 30a. However, unlike the findings from Kús et al. [110], no clear relationship between catalyst surface basicity and catalytic performance could be quantified, as illustrated in Figure 30b, where the linear correlation coefficient between surface basicity, in mol·m^2, and CH_4 conversion, C2 selectivity and C2 yield are plotted as a function of reaction conditions. As can be seen, the obtained correlations are all below 0.4, suggesting a weak or non-existent relationship.

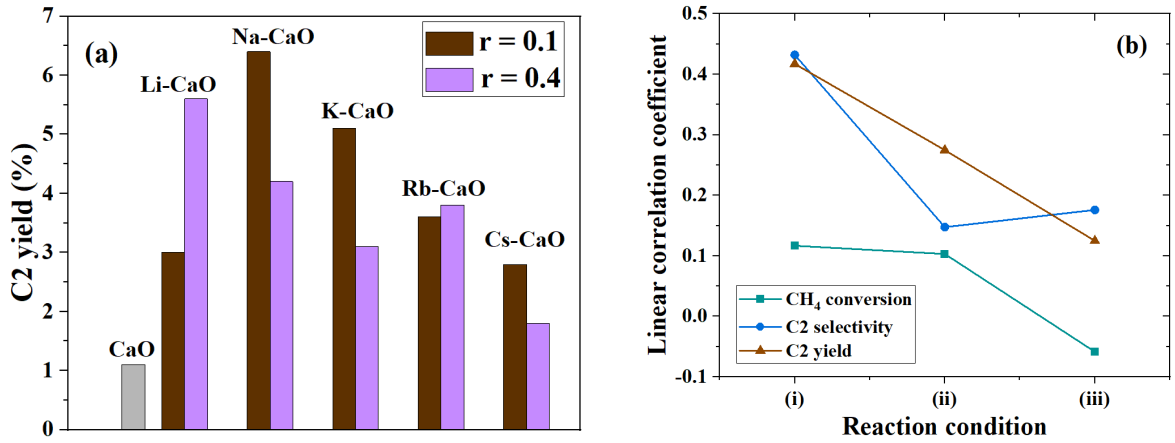

Figure 30. (**a**) C2 yield for different bimetallic catalysts obtained at 700 °C and CH_4/O_2 of 4.0. In the figures, *r* denotes the alkali metal to Ca ratio. (**b**) Linear correlation coefficient between surface basicity, in mol·m^2, and CH_4 conversion (■), C2 selectivity (●) and C2 yield (▲) as a function of reaction conditions ((*i*): 700 °C, CH_4/O_2 of 4.0; (*ii*): 750 °C, CH_4/O_2 of 4.0; (*iii*): 750 °C, CH_4/O_2 of 8.0. Data sourced from [164].

A similar lack of clear relationship between catalyst properties, such as surface basicity and specific area and catalytic performance, was reported for La-doped CaO catalysts prepared from different sources of starting materials [159], leading the authors to conclude that surface acidity could also be important in the OCM mechanism, even though surface acidity was not characterised.

In contrast, a clear relationship between CH_4 conversion, C2 selectivity and surface basicity was reported for catalysts based on Sr-Al mixed oxides [160]. In this study, the authors demonstrated how tailoring the Sr/Al atomic ratio could allow for improving C2 selectivities and yields, as illustrated in Figure 31, as Sr atoms substituted on the amorphous fraction of the Al_2O_3 oxide could contribute to the formation of both oxygen vacancies and oxygen electrophilic species through O_2 adsorption on Lewis base centres, supporting therefore that CH_4 activation could occur via a homolytic route (Figure 28). However, an increase in the ratio between Al^{IV}/Al^{VI} species with Sr composition was also observed, and thus a contribution from acid–base pairs through a heterolytic route could not be ruled out. The Sr/Al-1.25 catalyst would, in addition, be able to keep its catalytic performance without significant signs of deactivation for 48 h at 810 °C [160].

The concentration of basic sites was also demonstrated to correlate with C2 yields over Sm_2O_3/MgO, TbO_x/MgO, CeO_2/MgO and PrO_y/MgO systems [52], according to measurements of CO_2-TPD. In this case, the volume of CO_2 desorbed at around 360 °C followed the order of $Sm_2O_3/MgO > TbO_x/MgO > PrO_y/MgO > MgO > CeO_2/MgO$, which was similar to the order of obtained C2 yields between 500 and 800 °C.

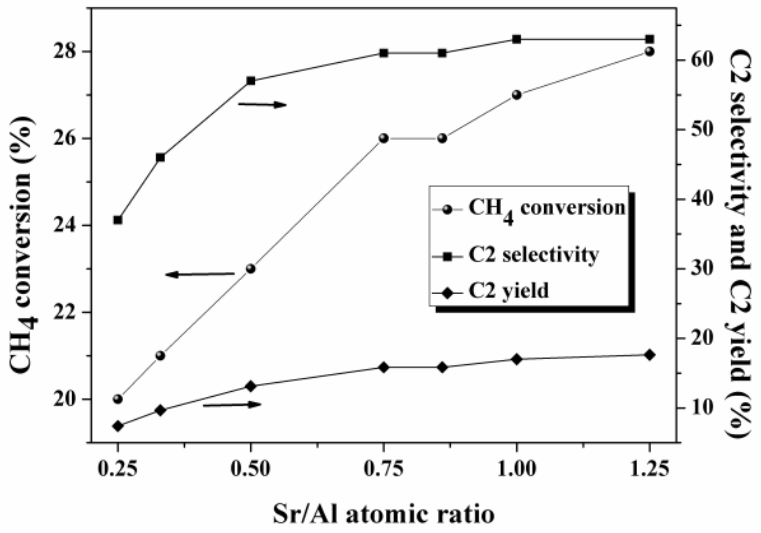

Figure 31. Sr/Al atomic ratio effect on catalytic performance. Reactions were performed at 810 °C, CH_4/O_2 equal to 5, and total flow of 130 mL·min^{-1} [160].

Catalytic systems based on Sr-doped La_2O_3 [126,163,166] have also been reported as promising, with more recent findings supporting their high concentration of basic sites [63,157]. However, catalytic stability seems to be limited to reaction times up to 30 h, with longer stability up to 60 h being demonstrated upon the doping of Sr/La_2O_3 with zirconium [63].

Besides the distinct chemical properties obtained from different combinations of metal oxides, morphological properties have also been demonstrated to exert an important role in the OCM process, as demonstrated by the advent of nanocatalysts showing catalytic advantages when compared to their bulk powder counterparts [163,167]. For instance, nanocatalysts have been demonstrated to be active at lower reaction temperatures [167,168], a fact which has been associated with their larger surface area and well-defined surface structure [167]. Improved thermal stability has also been suggested as a potential advantage due to higher levels of surface organisational stoichiometry, which could minimise the likelihood of deactivation due to particles sintering and metal agglomeration [169,170]. In this context, the development of nanocatalysts with particular morphologies, such as nanofibers and nanowires, has been receiving great attention, in particular due to the large surface-to-volume ratios achievable with these systems, enabling higher fractions of atoms to be located at the surface, and thus increasing the availability of active sites. However, as pointed by Yunarti et al. [161], typical high OCM temperatures may negatively impact the above-mentioned morphological features, minimising their catalytic advantages.

Experimental data obtained over bimetallic oxides are organised in Figure 32, where C2 yields are plotted as a function of the CH_4 conversion. This figure includes experimental data obtained over catalysts based on promoted or supported alkaline earth metal oxides, including K/MgO [158], Li/MgO [103,111,158,162], Ba/MgO [171], Na/MgO, Rb/MgO, Cs/MgO [103], Li/CaO, Na/CaO, K/CaO, Rb/CaO, Cs/CaO [164], La_2O_3/CaO [159], Sm_2O_3/MgO, TbO_x/MgO, CeO_2/MgO and PrO_y/MgO [52] (Figure 32a); lanthanoids metal oxides, such as $LaAlO_3$, $LaGaO_3$, $LaInO_3$ [172], Sr/La_2O_3 [126,163,166], La_2O_3-CeO [135,169] (Figure 32b); and transition or post-transition metal oxides, including $SrTiO_3$, Sr_2TiO_4 [173], Mn/TiO_2, Mo/TiO_2, Cr/TiO_2, Co/TiO_2 [161] and $SrO\text{-}Al_2O_3$ [160,174] mixed oxides (Figure 32c).

It can be observed that CH_4 conversions are typically lower than 30% and that the maximum experimental C2 yields fluctuate around 15–20%. When overall C2 yields are evaluated as a function of the methane conversion, a similar mean C2 selectivity approximately equal to 53% can be calculated, indicating that bimetallic oxides could present an overall similar catalytic performance, with C2 yield being a function of CH_4

conversion. In addition, with only a few exceptions, we have verified experimental CH_4 conversions to be far from equilibrium, as illustrated in Figure S2a–c in the Supplementary Materials, suggesting that similar C2 selectivities could not be explained by global thermodynamic equilibrium.

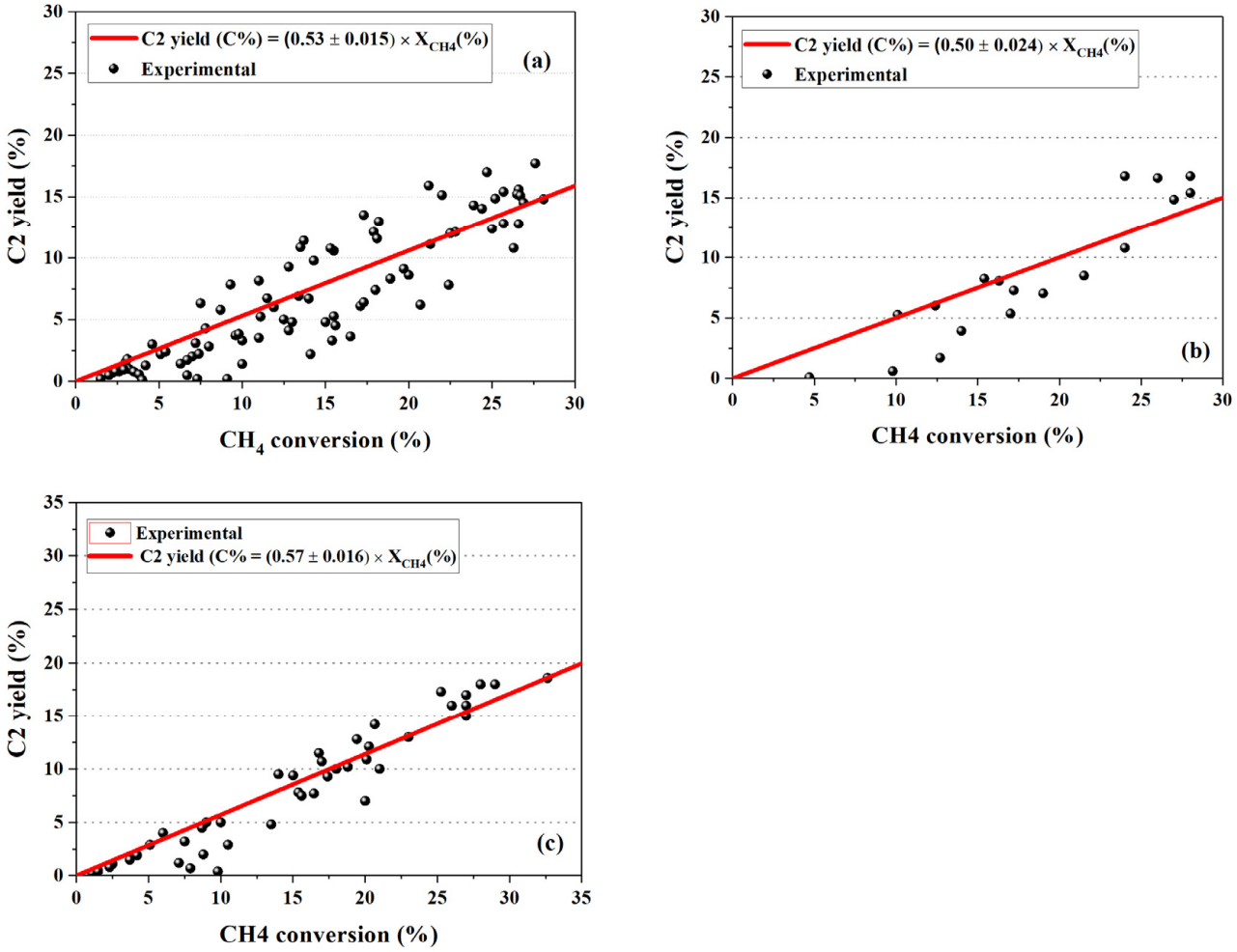

Figure 32. Experimental C2 yields as a function of CH_4 conversion for bimetallic oxides: (**a**) promoted or supported alkaline earth metal oxides, (**b**) involving lanthanoids metal oxides, and (**c**) transition or post-transition metal oxides. Data sources are indicated in the text.

As discussed in Section 4 and illustrated in Figure 24, the maximum achievable thermodynamic yield corresponds to conditions in which CO and CO_2 formation can be suppressed, in which case the thermodynamic C2 yield approaches CH_4 conversion. Therefore, if observed experimental CH_4 conversions would be assumed as approaching the maximum C2 thermodynamic yield, it would be possible to verify that experimental yields could be further increased in most cases if the formation of CO and CO_2 could be avoided, as illustrated in Figure 33. Additionally, the above could also suggest that ethane and ethene formation could indeed be affected by a thermodynamic factor, since experimental C2 yields are not so far from this hypothetical maximum achievable in the absence of CO and CO_2. Thus, ethane and ethene formation reactions could be at the vicinity of a '*pseudo-equilibrium*' state, in which the formation of CO and CO_2 would represent the lowest limiting surface steps.

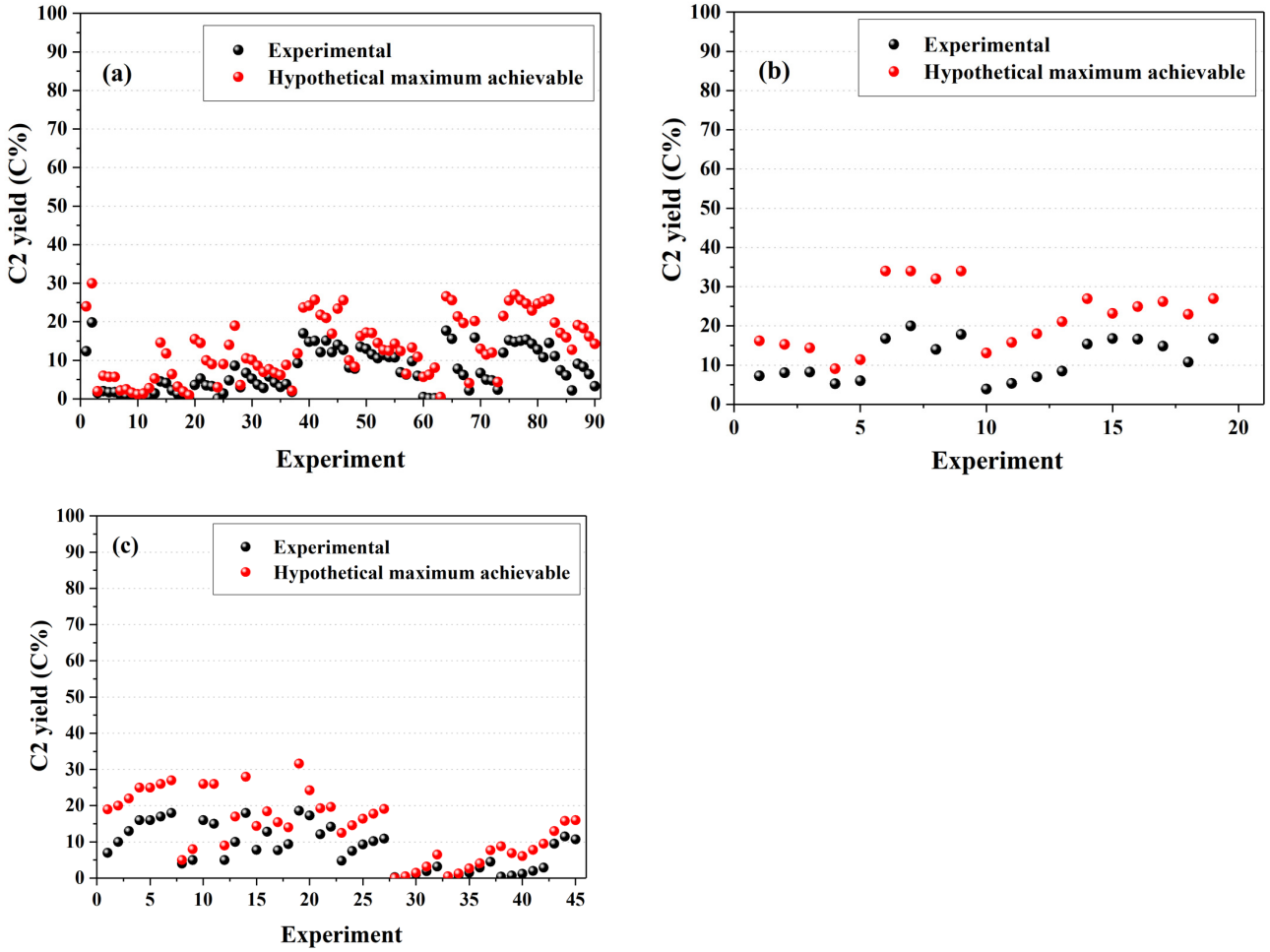

Figure 33. Comparison between experimental C2 yield and hypothetical maximum C2 achievable yield (in the absence of CO and CO_2 and at the same level of experimental methane conversion) for bimetallic oxides: (**a**) promoted or supported alkaline earth metal oxides, (**b**) involving lanthanoids metal oxides, and (**c**) transition or post-transition metal oxides.

5.3. Trimetallic Oxides

A wide variety of trimetallic oxide catalysts have also been investigated for ethene production from OCM, including Ba-substituted $LaInO_3$ perovskites [172], alkali or alkaline metal (Li, Na, Ca or Mg)-doped lanthanoid oxides (Sm_2O_3, TbO_x, CeO_2, and PrO_y) supported on MgO [52], substituted titanates $SrTiO_3$ and Sr_2TiO_4, promoted with Mg, Ca, Ba, Pb and Al [173], structured rings and monoliths based on bismuth-yttrium-samarium oxide [175] and Mg-Na-doped La_2O_3 nanowires [163].

Figure 34 summarises the ranges of CH_4 conversion and C2 yields reported over these catalytic systems, in which it can be noted that most of the conversions and yields are concentrated in the range below 30 and 20%, respectively, and that an average C2 selectivity of 54 ± 1.2% can describe reasonably well overall catalytic performances, in agreement with the average C2 selectivity calculated for bimetallic systems, Section 5.2.

CH_4 conversions higher than 30% at C2 yield levels of 20–25% have been reported over structured rings and monoliths based on bismuth-yttrium-samarium oxide [175]. According to these authors, the superior activity of the monolith-like structured catalytic reactor would relate to its organised flow pattern, which can contribute to more efficient interaction between reactants and the catalyst surface, as also concluded by others [56]. More recently, $La_2Ce_{1.5}Ca_{0.5}O_7$ oxides have also been reported to reach similar catalytic performances, with demonstrated thermal stability for up to 100 h [38].

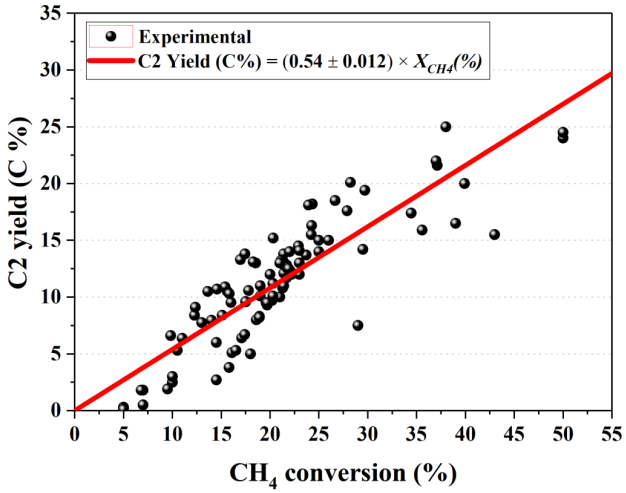

Figure 34. Experimental C2 yields as a function of methane conversion for trimetallic oxides. Data sources are indicated in the text.

Ba-substituted $LaInO_3$ catalytic activity has been rationalized to result from the production of active oxygen species upon Ba addition [172]. For alkali or alkaline metal (Li, Na, Ca or Mg)-doped lanthanoid oxides (Sm_2O_3, TbO_x, CeO_2, and PrO_y) supported on nanoparticles MgO catalysts [52], Li-TbO_x/MgO and Na-TbO_x/MgO systems have demonstrated the most promising performances, albeit presenting poor thermal stability in a 30 h-long reaction test at 700 °C, with a CH_4/O_2 feed molar ratio equal to 4 and reactant stream diluted in nitrogen. Interestingly, the catalytic activity observed at 700 °C for the Li, Na, Ca or Mg-doped TbO_x/n-MgO systems could be well explained by its correlation with the distribution of basic sites per unit of surface area, as illustrated in Figure S3 in the Supplementary Materials. For substituted titanates $SrTiO_3$ and Sr_2TiO_4, promoted with Mg, Ca, Ba, Pb and Al [173], a positive effect of these metal additions on the initial $SrTiO_3$ and Sr_2TiO_4 materials has also been observed. In particular, Mg addition demonstrated the best improvement in C2 yield, which could also be associated with the resultant increase in the concentration of basic sites, as suggested by CO_2 adsorption experiments followed by infrared spectroscopic analysis.

Finally, it is also interesting to compare the catalytic activity reported over Mg-Na-doped La_2O_3 nanowire oxides [163], prepared using a biological template, reported as the key factor for the final oxide morphology, and a slow multi-step calcination procedure. In this case, Mg and Na addition resulted in only minor improvement in C2 selectivity at the cost of slightly lower CH_4 conversions, affording similar C2 yields between the Mg-Na-doped (11–15%) and monometallic La_2O_3 (13–15%) nanowire oxides.

5.4. Multimetallic Oxides

In the search for more efficient catalysts, multi-component systems have also been explored. By using computer-aided design with an artificial neural network, Huang et al. (2001, 2003) [176,177] reported an optimal chemical composition for a catalytic system constituted by Na, Mn, Zr, S, W and P supported on SiO_2. According to these authors' results, the optimised catalysts would be able to achieve selectivities towards C2 compounds as high as 70% even at CH_4 conversion levels of 35%, at nearly 800 °C and using a reactant stream of CH_4 and O_2 with no diluent. However, their thermal stability for long reaction times was not reported.

Another example involves Na-Co-doped LiMnMgB and undoped LiMnMgB oxide systems [178], for which high selectivities (64–68%) at relatively high CH_4 conversion levels (24–29%) have also been reported. In this case, the main advantage in doping the LiMnMgB system seems to have been the resultant higher activity at lower temperatures, affording a C2 yield increase from 1 to 12% between the undoped and doped system at 750 °C [178].

However, to the best of our knowledge, multimetallic catalyst systems comprising *Me*-W-Mn-O/SiO_2, in which *Me* stands for Na or Ce, and TiO_2-doped *Na*-W-Mn-O/SiO_2, represent some of the few catalytic systems for which thermal stability has been shown to endure for up to 500 and 1000 h [50,134,179,180]. Not surprisingly, these catalysts have been extensively investigated in an attempt to understand the reasons for their outstanding stability and identify active sites [44,181]. However, as noted previously [181], the identity of active sites associated with these systems remains under debate [182,183], with more recent findings suggesting sodium oxide species as active sites which would remain stable due to 'synergistic' effects between Na_2WO_4 and Mn_7SiO_{12} phases [182].

In addition, several studies have explored the impact of different preparation procedures [48,54,174,184,185], alternative supports to SiO_2 [178,186–188], dopants [183] and the substitution of Na [46,49,51,179,186,189] or Mn [186] by different elements in the above-mentioned system. Incipient wetness impregnation was suggested to produce a more active catalyst when compared to sol-gel synthesis for athe same chemical composition in a study involving *Na*-W-Mn-O/SiO_2 [184]. In contrast, sol-gel synthesis was indicated as the most suitable method for obtaining higher ethylene yields when compared to impregnation or physical mixing in a study involving *Li*-W-Mn-O/SiO_2 [179]. According to these authors [179], the high degree of homogenisation enabled by the sol-gel method would be responsible for the formation of a highly crystalline structure, which would be important to obtain higher C2 yields, even though similar catalytic performances were observed for catalysts prepared by physical mixing, which presented poor crystallinity. More recently, the preparation of core–shell structures has been claimed to result in more C2-selective *Na*-W-Mn-O/SiO_2 catalysts due to a greater dispersion of active components, even though reported selectivities could not be regarded as statistically different from bulk *Na*-W-Mn-O/SiO_2 catalysts [190].

The evaluation of alternative supports to SiO_2 has in general confirmed SiO_2 as the most promising support for this catalytic system [178,186–188], as further illustrated in Figure 35, which was compiled from data reported by [53,178,185–189,191], where reports in a molar base [183,187,192] were excluded. In addition, it was demonstrated that the use of ordered mesoporous silica, as opposed to commercial silica gel, could improve catalytic performance by enabling better dispersion of active sites on the catalyst surface, as suggested by energy-dispersive X-ray spectroscopy (EDX) mapping measurements, even after the collapse of the mesoporous structure upon thermal treatment around 750 °C [53,192].

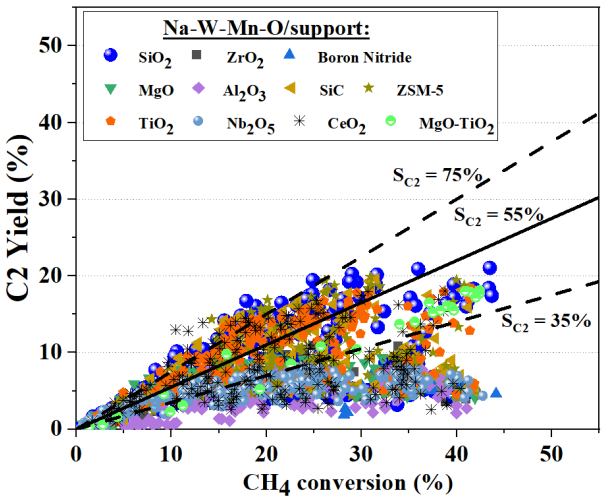

Figure 35. Experimental C2 yield as a function of CH_4 conversion reported over Na-W-Mn-O/support catalysts at different OCM reaction conditions [53,178,185–189,191]. The continuous black line denotes the slope where selectivity is 55%.

The doping of the *Na*-W-Mn-O/SiO_2 catalyst with Pt, Ir and Rh has also been reported to improve catalyst reducibility, as suggested by H_2 temperature-programmed reduction experiments (H_2-TPR), resulting in a shift in the product selectivity distribution in which smaller amounts of CO and CO_2 compounds were observed at 750 °C [183]. More recently, high-throughput screening has also been applied to assess the effect of substituting Na or Mn by different elements in the above-mentioned system in a wide range of reaction operational conditions [186], further supporting previous indications that the best catalytic performance is associated with the *Na*-W-Mn-O/SiO_2 system [189].

Finally, it is interesting to note that most promising catalytic performances, as illustrated in Figure 35, could still be described by an average C2 selectivity approximately equal to 55 ± 20%, with slightly higher selectivities being observed at lower CH_4 conversions.

6. Environmental Concerns: Can OCM Be Sustainable?

OCM has been described as one of the most promising routes to convert methane into more valuable hydrocarbons [35,193,194]. However, economic feasibility analyses have shown that greater C2 yields are needed to enable profit [123]. For this reason, many efforts focused on optimising C2 yields have been made, as also shown in previous sections. In contrast, little attention has been focused on addressing the huge amounts of CO and CO_2 produced. As a matter of fact, OCM implementation should only be encouraged if produced CO and CO_2 can be realistically recycled in the process or managed by alternative solutions.

Prospects for CO_2 utilisation can be broadly divided into two main process categories. The first involves the direct consumption of CO_2, for example, its use in the production of food, beverages, and chemicals. The second class of processes involves its conversion into other compounds. However, although such applications exist, their viable scales are still small and, therefore, they have a small impact on current global CO_2 emissions [195–197]. Additional pathways and their associated challenges are discussed in [198].

Therefore, integrating OCM with an ethane cracker could represent an alternative for reutilising the CO and CO_2 produced, although not necessarily representing a complete solution. In this case, OCM-generated CO and CO_2 could be coupled with H_2 from ethane cracking in a methanation reactor for producing methane. In addition, this approach can present the advantage of energy savings, as the heat produced in the methanation reactor could be used as supply in endothermic ethane dehydrogenation [199]. However, questions arise on the impact of the impurities present in OCM output streams on the stability and performance of methanation catalysts. Clearly, more studies must be carried out in this area to prove the technical and economic feasibility of these integrations.

7. Conclusions and Outlook

The present review on the oxidative coupling of methane for ethylene production has highlighted important challenges to be addressed if OCM technology is to be implemented at an industrial scale. Firstly, the proposed bibliometric analysis of OCM scientific publications and patents indicated that the focuses of academic and industrial research have been distinct, with the former concentrating efforts towards catalyst development and the latter being concerned with broader aspects of process flow diagrams. Therefore, further scientific studies to support the industrial focus on optimising OCM flow diagrams seem to be needed.

Secondly, the proposed analysis of OCM reactions and kinetics, involving chemical reactor modelling approaches, suggests that further studies are greatly needed to enable the prediction (and thus optimisation) of catalytic performances at reaction conditions of industrial interest (involving high pressures), despite the significant advances in the understanding of kinetic mechanisms and the modelling of catalytic activity. Additionally, how experimental studies have indicated the existence of different active sites on OCM catalyst surfaces was discussed, including, for instance, different oxygen active species. Despite this, the kinetic models developed so far have considered a unique entity to represent existing active catalyst sites. Moreover, the fact that both simpler (involving

10 catalytic reaction steps) and more complex (involving 26 catalytic reaction steps) kinetic models can well represent catalytic performances at atmospheric conditions suggests that kinetic descriptions can be improved and that further studies are urgently needed for discriminating among OCM kinetic models and, thus, determining the most suitable one for reactor and process design.

The analysis of chemical reactor modelling approaches also suggests the lack of consensus on the importance of describing mass and energy balances in the reactor and catalyst scale, as the vast majority of scientific papers concerning modelling studies (58% of a sample of 30 papers) reports a preference for the use of homogeneous or pseudo-homogeneous models, despite undeniable previous research on the importance of considering concentration gradients of radical intermediate species inside catalyst particles. Thus, further studies are needed for developing heterogenous and two-dimensional models that can embrace mass and energy transport among the distinct reactor phases simultaneously. These models could then be applied for assessing the feasibility of autothermal operation, which could represent a great technological breakthrough for OCM operation.

Furthermore, the proposed review on some thermodynamic aspects of the OCM reactions stressed how maximum ethylene yields are limited by CH_4 thermodynamic conversions, although favoured by high inert feed compositions and high temperatures (above 850 °C). As thermodynamics favour H_2 and CO formation at typical OCM conditions, it appears that economic feasibility should be pursued while integrating OCM with alternative processes.

Finally, the analysis of OCM active catalysts and their performances suggests that a common average selectivity of approximately 55% can be observed among promising catalytic materials, despite operating far from global thermodynamic equilibrium, indicating that OCM catalytic performance may be affected (and limited) by thermodynamic factors, further supporting the need for additional studies on OCM kinetic models, as already mentioned. However, the review also stresses the need for further assessments on catalyst stability at reaction conditions of industrial interest, as thermal stability has been largely overlooked, despite its fundamental importance for OCM industrial feasibility.

Supplementary Materials: The following are available online at https://www.mdpi.com/article/10.3390/pr9122196/s1, Section S1: Yields and Selectivities definitions, Table S1: Standard Gibbs energies in increasing order at 900 °C and standard reaction enthalpies for global OCM reactions, Figure S1: Effect of the CH_4/O_2 feed ratio and temperature at 1 bar on the combined ethene and ethane (C2) yield, Figure S2: Comparison between experimental and equilibrium CH_4 conversions for bimetallic oxides, Figure S3: Relationship between C2 yield and basicity distribution per unit of surface area.

Author Contributions: Conceptualisation, S.D.R.; Methodology, S.D.R.; Formal Analysis, S.D.R.; Investigation, S.D.R.; Visualisation, S.D.R.; Writing—original draft preparation, S.D.R. and T.B.F.; Writing—review and editing, S.D.R., J.C.P., M.S., T.B.F. and N.J.C.d.J.; funding acquisition: J.C.P. All authors have read and agreed to the published version of the manuscript.

Funding: The authors thank CNPq (Conselho Nacional de Desenvolvimento Científico e Tecnológico, Brazil), CAPES (Coordenação de Aperfeiçoamento de Pessoal de Nível Superior), FAPERJ (Fundação Carlos Chagas Filho de Apoio à Pesquisa do Estado do Rio de Janeiro, Brazil) and BRASKEM S.A. for financial support and scholarships. The APC has been waived.

Data Availability Statement: All collected data are presented in this work.

Conflicts of Interest: The authors declare no conflict of interest.

References

1. Da Ros, S.; Jones, M.D.; Mattia, D.; Pinto, J.C.; Schwaab, M.; Noronha, F.B.; Kondrat, S.A.; Clarke, T.C.; Taylor, S.H. Ethanol to 1,3-Butadiene Conversion by Using ZrZn-Containing MgO/SiO_2 Systems Prepared by Co-Precipitation and Effect of Catalyst Ccidity Modification. *ChemCatChem* **2016**, *8*, 2376–2386. [CrossRef]
2. Da Ros, S.; Jones, M.D.; Mattia, D.; Schwaab, M.; Noronha, F.B.; Pinto, J.C. Modelling the Effects of Reaction Temperature and Flow Rate on the Conversion of Ethanol to 1,3-Butadiene. *Appl. Catal. A Gen.* **2017**, *530*, 37–47. [CrossRef]

3. EIA. Petroleum & Other Liquids, WTI Spot Price. Available online: www.eia.gov/dnav/pet/hist/rwtcA.htm (accessed on 4 August 2021).
4. EIA. Henry Hub Natural Gas Spot Price (Dollars per Million Btu). Available online: www.eia.gov/dnav/ng/hist/rngwhhda.htm (accessed on 4 August 2021).
5. EIA. Natural Gas: Dry Shale Gas Production Estimates by Play. Available online: https://www.eia.gov/naturalgas/data.php#production (accessed on 4 August 2021).
6. BP British Petrolium. BP Statistical Review of World Energy 2019 Report. Available online: https://www.bp.com/content/dam/bp/business-sites/en/global/corporate/pdfs/energy-economics/statistical-review/bp-stats-review-2019-full-report.pdf (accessed on 4 August 2021).
7. Ohyama, J.; Nishimura, S.; Takahashi, K. Data Driven Determination of Reaction Conditions in Oxidative Coupling of Methane via Machine Learning. *ChemCatChem* **2019**, *11*, 4307–4313. [CrossRef]
8. Miyazato, I.; Nishimura, S.; Takahashi, L.; Ohyama, J.; Takahashi, K. Data-Driven Identification of the Reaction Network in Oxidative Coupling of the Methane Reaction via Experimental Data. *J. Phys. Chem. Lett.* **2020**, *11*, 787–795. [CrossRef]
9. Ghareghashi, A.; Sarrafi, A.; Ghader, S. The Effect of Heat Transfer on Products of a Thermally Coupled Shell and Tube Reactor Consisting of Two Processes: Steam Reforming of Methane and Oxidative Coupling of Methane. *Chem. Eng. Process. Process Intensif.* **2018**, *133*, 263–277. [CrossRef]
10. Li, D.; Baslyman, W.S.; Sarathy, S.M.; Takanabe, K. Impact of OH Radical Generator Involvement in the Gas-Phase Radical Reaction Network on the Oxidative Coupling of Methane—A Simulation Study. *Energy Technol.* **2019**, *8*, 1900563. [CrossRef]
11. Yancy-Caballero, D.M.; Biegler, L.T.; Guirardello, R. Large-Scale DAE-Constrained Optimization Applied to a Modified Spouted Bed Reactor for Ethylene Production from Methane. *Comput. Chem. Eng.* **2018**, *113*, 162–183. [CrossRef]
12. Mohammadi, Y.; Penlidis, A. "Optimulation" in Chemical Reaction Engineering: Oxidative Coupling of Methane as a Case Study. *Ind. Eng. Chem. Res.* **2018**, *57*, 8664–8678. [CrossRef]
13. Wiyaratn, W.; Manundawee, S.; Arpornwichanop, A.; Assabumrungrat, S.; Watanapa, A.; Worawimut, C. Two-Dimensional Mathematical Modeling of the Oxidative Coupling of Methane in a Membrane Reactor. *Eng. J.* **2016**, *20*, 17–33. [CrossRef]
14. Manundawee, S.; Arpornwichanop, A.; Assabumrungrat, S.; Wiyaratn, W. Two-Dimensional Modeling of the Oxidative Coupling of Methane in a Fixed Bed Reactor: A Comparison among Different Catalysts. *Eng. J.* **2017**, *21*, 77–99. [CrossRef]
15. Lomonosov, V.; Gordienko, Y.; Ponomareva, E.; Sinev, M. Kinetic Conjugation Effects in Oxidation of C1-C2 Hydrocarbons: Experiment and Modeling. *Chem. Eng. J.* **2019**, *370*, 1210–1217. [CrossRef]
16. Alexiadis, V.I.; Serres, T.; Marin, G.B.; Mirodatos, C.; Thybaut, J.W.; Schuurman, Y. Analysis of Volume-to-surface Ratio Effects on Methane Oxidative Coupling Using Microkinetic Modeling. *AIChE J.* **2018**, *64*, 2603–2611. [CrossRef]
17. Alexiadis, V.I.; Chaar, M.; van Veen, A.; Muhler, M.; Thybaut, J.W.; Marin, G.B. Quantitative Screening of an Extended Oxidative Coupling of Methane Catalyst Library. *Appl. Catal. B Environ.* **2016**, *199*, 252–259. [CrossRef]
18. Obradović, A.; Thybaut, J.W.; Marin, G.B. Oxidative Coupling of Methane: Opportunities for Microkinetic Model-Assisted Process Implementations. *Chem. Eng. Technol.* **2016**, *39*, 1996–2010. [CrossRef]
19. Karakaya, C.; Zhu, H.; Loebick, C.; Weissman, J.G.; Kee, R.J. A Detailed Reaction Mechanism for Oxidative Coupling of Methane over $Mn/Na_2WO_4/SiO_2$ Catalyst for Non-Isothermal Conditions. *Catal. Today* **2018**, *312*, 10–22. [CrossRef]
20. Pirro, L.; Obradović, A.; Vandegehuchte, B.D.; Marin, G.B.; Thybaut, J.W. Model-Based Catalyst Selection for the Oxidative Coupling of Methane in an Adiabatic Fixed-Bed Reactor. *Ind. Eng. Chem. Res.* **2018**, *57*, 16295–16307. [CrossRef]
21. Sun, Z.; Kota, A.; Sarsani, S.; West, D.H.; Balakotaiah, V. Bifurcation Analysis of Methane Oxidative Coupling without Catalyst. *Chem. Eng. J.* **2018**, *343*, 770–788. [CrossRef]
22. Liu, Z.; Ho Li, J.P.; Vovk, E.; Zhu, Y.; Li, S.; Wang, S.; Van Bavel, A.P.; Yang, Y. Online Kinetics Study of Oxidative Coupling of Methane over La_2O_3 for Methane Activation: What Is behind the Distinguished Light-off Temperatures? *ACS Catal.* **2018**, *8*, 11761–11772. [CrossRef]
23. Chaudhari, V.; Dutta, K.; Li, C.J.; Kopyscinski, J. Mechanistic Insights of Methane Conversion to Ethylene over Gallium Oxide and Gallium Nitride Using Density Functional Theory. *Mol. Catal.* **2020**, *482*, 110606. [CrossRef]
24. Pirro, L.; Mendes, P.S.F.; Paret, S.; Vandegehuchte, B.D.; Marin, G.B.; Thybaut, J.W. Descriptor-Property Relationships in Heterogeneous Catalysis: Exploiting Synergies between Statistics and Fundamental Kinetic Modelling. *Catal. Sci. Technol.* **2019**, *9*, 3109–3125. [CrossRef]
25. Luo, L.; You, R.; Liu, Y.; Yang, J.; Zhu, Y.; Wen, W.; Pan, Y.; Qi, F.; Huang, W. Gas-Phase Reaction Network of Li/MgO-Catalyzed Oxidative Coupling of Methane and Oxidative Dehydrogenation of Ethane. *ACS Catal.* **2019**, *9*, 2514–2520. [CrossRef]
26. Parishan, S.; Nowicka, E.; Fleischer, V.; Schulz, C.; Colmenares, M.G.; Rosowski, F.; Schomäcker, R. Investigation into Consecutive Reactions of Ethane and Ethene Under the OCM Reaction Conditions over $MnxOy–Na_2WO_4/SiO_2$ Catalyst. *Catal. Lett.* **2018**, *148*, 1659–1675. [CrossRef]
27. Noon, D.; Zohour, B.; Bae, A.; Seubsai, A.; Senkan, S. Effects of Ir-Doping on the Transition from Oxidative Coupling to Partial Oxidation of Methane in La_2O_3-CeO_2 Nanofiber Catalysts: Spatial Concentration and Temperature Profiles. *RSC Adv.* **2017**, *7*, 26783–26789. [CrossRef]
28. Schmack, R.; Friedrich, A.; Kondratenko, E.V.; Kraehnert, R.; Polte, J.; Werwatz, A. A Meta-Analysis of Catalytic Literature Data Reveals Property-Performance Correlations for the OCM Reaction. *Nat. Commun.* **2019**, *10*, 441. [CrossRef]
29. Lomonosov, V.I.; Sinev, M.Y. Oxidative Coupling of Methane: Mechanism and Kinetics. *Kinet. Catal.* **2016**, *57*, 647–676. [CrossRef]

30. Penteado, A.T.; Kim, M.; Godini, H.R.; Esche, E.; Repke, J.U. Techno-Economic Evaluation of a Biogas-Based Oxidative Coupling of Methane Process for Ethylene Production. *Front. Chem. Sci. Eng.* **2018**, *12*, 598–618. [CrossRef]
31. Ortiz-Espinoza, A.P.; Noureldin, M.M.B.; El-Halwagi, M.M.; Jiménez-Gutiérrez, A. Design, Simulation and Techno-Economic Analysis of Two Processes for the Conversion of Shale Gas to Ethylene. *Comput. Chem. Eng.* **2017**, *107*, 237–246. [CrossRef]
32. Cruellas, A.; Heezius, J.; Spallina, V.; van Sint Annaland, M.; Medrano, J.A.; Gallucci, F. Oxidative Coupling of Methane in Membrane Reactors; A Techno-Economic Assessment. *Processes* **2020**, *8*, 247. [CrossRef]
33. Godini, H.R.; Azadi, M.; Penteado, A.; Khadivi, M.; Wozny, G.; Repke, J.U. A Multi-Perspectives Analysis of Methane Oxidative Coupling Process Based on Miniplant-Scale Experimental Data. *Chem. Eng. Res. Des.* **2019**, *151*, 56–69. [CrossRef]
34. Cruellas, A.; Bakker, J.J.; van Sint Annaland, M.; Medrano, J.A.; Gallucci, F. Techno-Economic Analysis of Oxidative Coupling of Methane: Current State of the Art and Future Perspectives. *Energy Convers. Manag.* **2019**, *198*, 111789. [CrossRef]
35. Spallina, V.; Velarde, I.C.; Jimenez, J.A.M.; Godini, H.R.; Gallucci, F.; Van Sint Annaland, M. Techno-Economic Assessment of Different Routes for Olefins Production through the Oxidative Coupling of Methane (OCM): Advances in Benchmark Technologies. *Energy Convers. Manag.* **2017**, *154*, 244–261. [CrossRef]
36. Dutta, K.; Chaudhari, V.; Li, C.J.; Kopyscinski, J. Methane Conversion to Ethylene over GaN Catalysts. Effect of Catalyst Nitridation. *Appl. Catal. A Gen.* **2020**, *595*, 117430. [CrossRef]
37. Kirik, N.P.; Anshits, N.N.; Rabchevskii, E.V.; Solov'ev, L.A.; Anshits, A.G. Effect of HF Modification on the Catalytic Properties of Ferrospheres in the Oxidative Coupling of Methane. *Kinet. Catal.* **2019**, *60*, 196–204. [CrossRef]
38. Xu, J.; Zhang, Y.; Liu, Y.; Fang, X.; Xu, X.; Liu, W.; Zheng, R.; Wang, X. Optimizing the Reaction Performance of $La_2Ce_2O_7$-Based Catalysts for Oxidative Coupling of Methane (OCM) at Lower Temperature by Lattice Doping with Ca Cations. *Eur. J. Inorg. Chem.* **2019**, *2019*, 183–194. [CrossRef]
39. Fei, C.; Jian, Y.; Liang, Y.; Jun, Z.; Huahua, Z.; Huanling, S.; Lingjun, C. Influence of the Composition/Texture of Solid Acid WO_3/TiO_2-Supported Lithium-Manganese Catalysts on the Oxidative Coupling of Methane. *Wuli Huaxue Xuebao Acta Phys. Chim. Sin.* **2019**, *35*, 1027–1036. [CrossRef]
40. Cheng, F.; Yang, J.; Yan, L.; Zhao, J.; Zhao, H.; Song, H.; Chou, L. Impact of Chloride Ions on the Oxidative Coupling of Methane over Li/SnO_2 Catalyst. *React. Kinet. Mech. Catal.* **2018**, *125*, 675–688. [CrossRef]
41. Haneda, M.; Katsuragawa, Y.; Nakamura, Y.; Towata, A. Promoting Effect of Cerium Oxide on the Catalytic Performance of Yttrium Oxide for Oxidative Coupling of Methane. *Front. Chem.* **2018**, *6*, 581. [CrossRef]
42. Peng, L.; Xu, J.; Fang, X.; Liu, W.; Xu, X.; Liu, L.; Li, Z.; Peng, H.; Zheng, R.; Wang, X. SnO_2 Based Catalysts with Low-Temperature Performance for Oxidative Coupling of Methane: Insight into the Promotional Effects of Alkali-Metal Oxides. *Eur. J. Inorg. Chem.* **2018**, *2018*, 1787–1799. [CrossRef]
43. Oh, S.C.; Xu, J.; Tran, D.T.; Liu, B.; Liu, D. Effects of Controlled Crystalline Surface of Hydroxyapatite on Methane Oxidation Reactions. *ACS Catal.* **2018**, *8*, 4493–4507. [CrossRef]
44. Li, Z.; Wang, S.; Hong, W.; Zou, S.; Xiao, L.; Fan, J. Intelligent Optimization of $Na-Mn-W/SiO_2$ Catalysts for the Oxidative Coupling of Methane. *ChemNanoMat* **2018**, *4*, 487–495. [CrossRef]
45. Nadezhda, P.K.; Natalia, N.A.; Evgenii, V.R.; Leonid, A.S. The Activity of the HF-Modified Ferrospheres in Oxidative Coupling of Methane. *J. Sib. Fed. Univ. Chem.* **2018**, *11*, 347–360. [CrossRef]
46. Nipan, G.D. Specific Phase Transformations of $K/W/Mn/SiO_2$ Composite Catalyst. *Inorg. Mater.* **2018**, *54*, 96–101. [CrossRef]
47. Ogihara, H.; Imai, N.; Yoshida-Hirahara, M.; Kurokawa, H. Direct Dehydrogenative Conversion of Methane to Hydrogen, Nanocarbons, Ethane, and Ethylene on Pd/SiO_2 Catalysts. *Chem. Lett.* **2020**, *49*, 236–239. [CrossRef]
48. Hayek, N.S.; Lucas, N.S.; Warwar Damouny, C.; Gazit, O.M. Critical Surface Parameters for the Oxidative Coupling of Methane over the Mn-Na-W/SiO_2 Catalyst. *ACS Appl. Mater. Interfaces* **2017**, *9*, 40404–40411. [CrossRef] [PubMed]
49. Nipan, G.D. Melt-Assisted Phase Transformations of $A/W/Mn/SiO_2$ (A = Li, Na, K, Rb, Cs) Composite Catalysts. *Inorg. Mater.* **2017**, *53*, 553–559. [CrossRef]
50. Wang, P.; Zhao, G.; Wang, Y.; Lu, Y. $MnTiO_3$-Driven Low-Temperature Oxidative Coupling of Methane over TiO_2-Doped Mn_2O_3-Na_2WO_4/SiO_2 Catalyst. *Sci. Adv.* **2017**, *3*, e1603180. [CrossRef] [PubMed]
51. Nipan, G.D.; Buzanov, G.A.; Zhizhin, K.Y.; Kuznetsov, N.T. Phase States of Li(Na,K,Rb,Cs)/W/Mn/SiO_2composite Catalysts for Oxidative Coupling of Methane. *Russ. J. Inorg. Chem.* **2016**, *61*, 1689–1707. [CrossRef]
52. Elkins, T.W.; Roberts, S.J.; Hagelin-Weaver, H.E. Effects of Alkali and Alkaline-Earth Metal Dopants on Magnesium Oxide Supported Rare-Earth Oxide Catalysts in the Oxidative Coupling of Methane. *Appl. Catal. A Gen.* **2016**, *528*, 175–190. [CrossRef]
53. Colmenares, M.G.; Simon, U.; Yildiz, M.; Arndt, S.; Schomaecker, R.; Thomas, A.; Rosowski, F.; Gurlo, A.; Goerke, O. Oxidative Coupling of Methane on the Na2WO4-MnxOy Catalyst: COK-12 as an Inexpensive Alternative to SBA-15. *Catal. Commun.* **2016**, *85*, 75–78. [CrossRef]
54. Yildiz, M.; Aksu, Y.; Simon, U.; Otremba, T.; Kailasam, K.; Göbel, C.; Girgsdies, F.; Görke, O.; Rosowski, F.; Thomas, A.; et al. Silica Material Variation for the Mn_xO_y-Na_2WO_4/SiO_2. *Appl. Catal. A Gen.* **2016**, *525*, 168–179. [CrossRef]
55. Anshits, A.G.; Bayukov, O.A.; Kondratenko, E.V.; Anshits, N.N.; Pletnev, O.N.; Rabchevskii, E.V.; Solovyov, L.A. Catalytic Properties and Nature of Active Centers of Ferrospheres in Oxidative Coupling of Methane. *Appl. Catal. A Gen.* **2016**, *524*, 192–199. [CrossRef]

56. Sollier, B.M.; Gómez, L.E.; Boix, A.V.; Miró, E.E. Oxidative Coupling of Methane on Cordierite Monoliths Coated with Sr/La_2O_3 Catalysts. Influence of Honeycomb Structure and Catalyst-Cordierite Chemical Interactions on the Catalytic Behavior. *Appl. Catal. A Gen.* **2018**, *550*, 113–121. [CrossRef]
57. Igenegbai, V.O.; Almallahi, R.; Meyer, R.J.; Linic, S. Oxidative Coupling of Methane over Hybrid Membrane/Catalyst Active Centers: Chemical Requirements for Prolonged Lifetime. *ACS Energy Lett.* **2019**, *4*, 1465–1470. [CrossRef]
58. Pirro, L.; Mendes, P.S.F.; Vandegehuchte, B.D.; Marin, G.B.; Thybaut, J.W. Catalyst Screening for the Oxidative Coupling of Methane: From Isothermal to Adiabatic Operation: Via Microkinetic Simulations. *React. Chem. Eng.* **2020**, *5*, 584–596. [CrossRef]
59. Igenegbai, V.O.; Meyer, R.J.; Linic, S. In Search of Membrane-Catalyst Materials for Oxidative Coupling of Methane: Performance and Phase Stability Studies of Gadolinium-Doped Barium Cerate and the Impact of Zr Doping. *Appl. Catal. B Environ.* **2018**, *230*, 29–35. [CrossRef]
60. Garcia-Fayos, J.; Lobera, M.P.; Balaguer, M.; Serra, J.M. Catalyst Screening for Oxidative Coupling of Methane Integrated in Membrane Reactors. *Front. Mater.* **2018**, *5*, 1–11. [CrossRef]
61. Oh, S.C.; Wu, Y.; Tran, D.T.; Lee, I.C.; Lei, Y.; Liu, D. Influences of Cation and Anion Substitutions on Oxidative Coupling of Methane over Hydroxyapatite Catalysts. *Fuel* **2016**, *167*, 208–217. [CrossRef]
62. Farrell, B.L.; Linic, S. Oxidative Coupling of Methane over Mixed Oxide Catalysts Designed for Solid Oxide Membrane Reactors. *Catal. Sci. Technol.* **2016**, *6*, 4370–4376. [CrossRef]
63. Zhao, M.; Ke, S.; Wu, H.; Xia, W.; Wan, H. Flower-like $Sr\text{-}La_2O_3$ Microspheres with Hierarchically Porous Structures for Oxidative Coupling of Methane. *Ind. Eng. Chem. Res.* **2019**, *58*, 22847–22856. [CrossRef]
64. Seubsai, A.; Tiencharoenwong, P.; Kidamorn, P.; Niamnuy, C. Synthesis of Light Hydrocarbons via Oxidative Coupling of Methane over Silica-Supported Na_2WO_4-Tio_2 Catalyst. *Eng. J.* **2019**, *23*, 169–182. [CrossRef]
65. Yıldız, M. Mesoporous TiO_2-Rutile Supported $MnxOy\text{-}Na_2WO_4$: Preparation, Characterization and Catalytic Performance in the Oxidative Coupling of Methane. *J. Ind. Eng. Chem.* **2019**, *76*, 488–499. [CrossRef]
66. Kwon, G.; Shin, D.; Jeong, H.; Sahoo, S.K.; Lee, J.; Kim, G.; Choi, J.; Kim, D.H.; Han, J.W.; Lee, H. Oxidative Methane Conversion to Ethane on Highly Oxidized Pd/CeO_2 Catalysts Below 400 °C. *ChemSusChem* **2020**, *13*, 677–681. [CrossRef] [PubMed]
67. Özdemir, H.; Öksüzömer, M.A.F.; Ali Gürkaynak, M. Studies on Oxidative Coupling of Methane Using Sm_2O_3-Based Catalysts. *Chem. Eng. Commun.* **2019**, *206*, 48–60. [CrossRef]
68. Matsumoto, T.; Saito, M.; Ishikawa, S.; Fujii, K.; Yashima, M.; Ueda, W.; Motohashi, T. High Catalytic Activity of Crystalline Lithium Calcium Silicate for Oxidative Coupling of Methane Originated from Crystallographic Joint Effects of Multiple Cations. *ChemCatChem* **2020**, *12*, 1968–1972. [CrossRef]
69. Cheng, F.; Yang, J.; Yan, L.; Zhao, J.; Zhao, H.; Song, H.; Chou, L.J. Enhancement of La_2O_3 to $Li\text{-}Mn/WO_3/TiO_2$ for Oxidative Coupling of Methane. *J. Rare Earths* **2020**, *38*, 167–174. [CrossRef]
70. Bosch, C.E.; Poulston, S.; Collier, P.; Thybaut, J.W.; Marin, G.B. Exploring Microemulsion-Prepared Lanthanum Catalysts for Natural Gas Valorisation. *Johnson Matthey Technol. Rev.* **2019**, *63*, 265–276. [CrossRef]
71. Lee, B.J.; Hur, Y.G.; Kim, D.H.; Lee, S.H.; Lee, K.Y. Non-Oxidative Aromatization and Ethylene Formation over Ga/HZSM-5 Catalysts Using a Mixed Feed of Methane and Ethane. *Fuel* **2019**, *253*, 449–459. [CrossRef]
72. Jones, A.S.; Alfonso, N.; Hagelin-Weaver, H.E. Transition-Metal Doped, Magnesium Oxide-Supported Terbium Oxides as Catalysts for the Oxidative Coupling of Methane. *Polyhedron* **2019**, *170*, 602–611. [CrossRef]
73. Chukeaw, T.; Sringam, S.; Chareonpanich, M.; Seubsai, A. Screening of Single and Binary Catalysts for Oxidative Coupling of Methane to Value-Added Chemicals. *Mol. Catal.* **2019**, *470*, 40–47. [CrossRef]
74. Kolesnichenko, N.V.; Ezhova, N.N.; Snatenkova, Y.M. Lower Olefins from Methane: Recent Advances. *Russ. Chem. Rev.* **2020**, *89*, 191–224. [CrossRef]
75. Gao, Y.; Neal, L.; Ding, D.; Wu, W.; Baroi, C.; Gaffney, A.M.; Li, F. Recent Advances in Intensified Ethylene Production—A Review. *ACS Catal.* **2019**, *9*, 8592–8621. [CrossRef]
76. Scapinello, M.; Delikonstantis, E.; Stefanidis, G.D. The Panorama of Plasma-Assisted Non-Oxidative Methane Reforming. *Chem. Eng. Process. Process Intensif.* **2017**, *117*, 120–140. [CrossRef]
77. García, L.; Poveda, Y.A.; Rodríguez, G.; Esche, E.; Godini, H.R.; Wozny, G.; Repke, J.U.; Orjuela, Á. Adsorption Separation of Oxidative Coupling of Methane Effluent Gases. Mini-Plant Scale Experiments and Modeling. *J. Nat. Gas Sci. Eng.* **2019**, *61*, 106–118. [CrossRef]
78. Bachman, J.E.; Reed, D.A.; Kapelewski, M.T.; Chachra, G.; Jonnavittula, D.; Radaelli, G.; Long, J.R. Enabling Alternative Ethylene Production through Its Selective Adsorption in the Metal-Organic Framework Mn2(: M -Dobdc). *Energy Environ. Sci.* **2018**, *11*, 2423–2431. [CrossRef]
79. Penteado, A.; Esche, E.; Salerno, D.; Godini, H.R.; Wozny, G. Design and Assessment of a Membrane and Absorption Based Carbon Dioxide Removal Process for Oxidative Coupling of Methane. *Ind. Eng. Chem. Res.* **2016**, *55*, 7473–7483. [CrossRef]
80. Parishan, S.; Littlewood, P.; Arinchtein, A.; Fleischer, V.; Schomäcker, R. Chemical Looping as a Reactor Concept for the Oxidative Coupling of Methane over the MnxOy-Na2WO4/SiO2 Catalyst, Benefits and Limitation. *Catal. Today* **2018**, *311*, 40–47. [CrossRef]
81. Fleischer, V.; Simon, U.; Parishan, S.; Colmenares, M.G.; Görke, O.; Gurlo, A.; Riedel, W.; Thum, L.; Schmidt, J.; Risse, T.; et al. Investigation of the Role of the $Na_2WO_4/Mn/SiO_2$ Catalyst Composition in the Oxidative Coupling of Methane by Chemical Looping Experiments. *J. Catal.* **2018**, *360*, 102–117. [CrossRef]

82. Chung, E.Y.; Wang, W.K.; Nadgouda, S.G.; Baser, D.S.; Sofranko, J.A.; Fan, L.S. Catalytic Oxygen Carriers and Process Systems for Oxidative Coupling of Methane Using the Chemical Looping Technology. *Ind. Eng. Chem. Res.* **2016**, *55*, 12750–12764. [CrossRef]
83. Fleischer, V.; Littlewood, P.; Parishan, S.; Schomäcker, R. Chemical Looping as Reactor Concept for the Oxidative Coupling of Methane over a $Na_2WO_4/Mn/SiO_2$ Catalyst. *Chem. Eng. J.* **2016**, *306*, 646–654. [CrossRef]
84. Bayanak, M.; Azimi, A. Investigation of Activity and Selectivity of Redox Catalysts in Oxidative Coupling of Methane in Fluidized Bed Reactor. *J. Fundam. Appl. Sci.* **2016**, *8*, 397. [CrossRef]
85. Aseem, A.; Harold, M.P. C2 Yield Enhancement during Oxidative Coupling of Methane in a Nonpermselective Porous Membrane Reactor. *Chem. Eng. Sci.* **2018**, *175*, 199–207. [CrossRef]
86. Liang, W.; Sarsani, S.; West, D.; Mamedov, A.; Lengyel, I.; Perez, H.; Lowrey, J. Performance Improvement for a Fixed-Bed Reactor with Layered Loading Catalysts of Different Catalytic Properties for Oxidative Coupling of Methane. *Catal. Today* **2018**, *299*, 60–66. [CrossRef]
87. Han, Q.; Tanaka, A.; Matsumoto, M.; Endo, A.; Kubota, Y.; Inagaki, S. Conversion of Methane to C_2 and C_3 Hydrocarbons over TiO_2/ZSM-5 Core-Shell Particles in an Electric Field. *RSC Adv.* **2019**, *9*, 34793–34803. [CrossRef]
88. Sato, A.; Ogo, S.; Takeno, Y.; Takise, K.; Seo, J.G.; Sekine, Y. Electric Field and Mobile Oxygen Promote Low-Temperature Oxidative Coupling of Methane over La1-XCaxAlO3-δ Perovskite Catalysts. *ACS Omega* **2019**, *4*, 10438–10443. [CrossRef] [PubMed]
89. Zhang, Y.; Cho, Y.; Yamaguchi, A.; Peng, X.; Miyauchi, M.; Abe, H.; Fujita, T. CO_2 Oxidative Coupling of Methane Using an Earth-Abundant CaO-Based Catalyst. *Sci. Rep.* **2019**, *9*, 15454. [CrossRef]
90. Hayek, N.S.; Khlief, G.J.; Horani, F.; Gazit, O.M. Effect of Reaction Conditions on the Oxidative Coupling of Methane over Doped MnO_x-Na_2WO_4/SiO_2 Catalyst. *J. Catal.* **2019**, *376*, 25–31. [CrossRef]
91. Valadkhani, A.; Shahrokhi, M.; Pishvaie, M.R.; Zarrinpashneh, S. Simulation and Experimental Studies of Methane Oxidative Coupling Reaction in a Bench Scale Fixed Bed Reactor. *Energy Sources Part A Recover. Util. Environ. Eff.* **2013**, *35*, 1418–1426. [CrossRef]
92. Stansch, Z.; Mleczko, M.; Baerns, L. Comprehensive Kinetics of Oxidative Coupling of Methane over the La_2O_3/CaO Catalyst. *Ind. Eng. Chem. Res.* **1997**, *36*, 2568–2579. [CrossRef]
93. Couwenberg, P.M.; Chen, Q.; Marin, G.B. Kinetics of a Gas-Phase Chain Reaction Catalyzed by a Solid: The Oxidative Coupling of Methane over Li/MgO-Based Catalysts. *Ind. Eng. Chem. Res.* **1996**, *35*, 3999–4011. [CrossRef]
94. Simon, Y.; Baronnet, F.; Côme, G.M.; Marquaire, P.M. Detailed Mechanism of the Oxidative Coupling of Methane. *Stud. Surf. Sci. Catal.* **2004**, *147*, 571–576. [CrossRef]
95. Sinev, M.Y.; Fattakhova, Z.T.; Lomonosov, V.I.; Gordienko, Y.A. Kinetics of Oxidative Coupling of Methane: Bridging the Gap between Comprehension and Description. *J. Nat. Gas Chem.* **2009**, *18*, 273–287. [CrossRef]
96. Chen, Q.; Hoebink, J.H.B.J.; Marin, G.B. Kinetics of the Oxidative Coupling of Methane at Atmospheric Pressure in the Absence of Catalyst. *Ind. Eng. Chem. Res.* **1991**, *30*, 2088–2097. [CrossRef]
97. Chen, Q.; Couwenberg, P.M.; Marin, G.B. Effect of Pressure on the Oxidative Coupling of Methane in the Absence of Catalyst. *AIChE J.* **1994**, *40*, 521–535. [CrossRef]
98. Zanthoff, H.W.; Baerns, M. Oxidative Coupling of Methane in the Gas Phase. Kinetic Simulation and Experimental Verification. *Ind. Eng. Chem. Res.* **1990**, *29*, 2–10. [CrossRef]
99. Chen, Q.; Couwenberg, P.M.; Marin, G.B. The Oxidative Coupling of Methane with Cofeeding of Ethane. *Catal. Today* **1994**, *21*, 309–319. [CrossRef]
100. Ekstrom, A.; Regtop, R.; Bhargava, S. Effect of Pressure on the Oxidative Coupling Reaction of Methane. *Appl. Catal.* **1990**, *62*, 253–269. [CrossRef]
101. Beck, B.; Fleischer, V.; Arndt, S.; Hevia, M.G.; Urakawa, A.; Hugo, P.; Schomäcker, R. Oxidative Coupling of Methane—A Complex Surface/Gas Phase Mechanism with Strong Impact on the Reaction Engineering. *Catal. Today* **2014**, *228*, 212–218. [CrossRef]
102. Al-Zahrani, S.; Song, Q.; Lobban, L.L. Effects of CO_2 during Oxidative Coupling of Methane over Li/MgO: Mechanisms and Models. *Ind. Eng. Chem. Res.* **1994**, *33*, 251–258. [CrossRef]
103. Choudhary, V.R.; Rane, V.H.; Pandit, M.Y. Comparison of Alkali Metal Promoted MgO Catalysts for Their Surface Acidity/Basicity and Catalytic Activity/Selectivity in the Oxidative Coupling of Methane. *J. Chem. Technol. Biotechnol.* **1997**, *68*, 177–186. [CrossRef]
104. Sun, J.; Thybaut, J.W.; Marin, G.B. Microkinetics of Methane Oxidative Coupling. *Catal. Today* **2008**, *137*, 90–102. [CrossRef]
105. Kechagiopoulos, P.N.; Thybaut, J.W.; Marin, G.B. Oxidative Coupling of Methane: A Microkinetic Model Accounting for Intraparticle Surface-Intermediates Concentration Profiles. *Ind. Eng. Chem. Res.* **2014**, *53*, 1825–1840. [CrossRef]
106. Nibbelke, R.H.; Scheerová, J.; De Croon, M.H.J.M.; Marin, G.B. The Oxidative Coupling of Methane over MgO-Based Catalysts: A Steady-State Isotope Transient Kinetic Analysis. *J. Catal.* **1995**, 106–119. [CrossRef]
107. Buyevskaya, M.O.V.; Rothaemel, M.; Zanthoff, H.W.; Baerns, M. Transient Studies on Reactions Steps in the Oxidative Coupling of Methane over Catalytic Surfaces of MgO and Sm_2O_3. *J. Catal.* **1994**, *146*, 346–357. [CrossRef]
108. Luo, L.; Tang, X.; Wang, W.; Wang, Y.; Sun, S.; Qi, F.; Huang, W. Methyl Radicals in Oxidative Coupling of Methane Directly Confirmed by Synchrotron VUV Photoionization Mass Spectroscopy. *Sci. Rep.* **2013**, *3*, 1625. [CrossRef] [PubMed]
109. Schwach, P.; Pan, X.; Bao, X. Direct Conversion of Methane to Value-Added Chemicals over Heterogeneous Catalysts: Challenges and Prospects. *Chem. Rev.* **2017**, *117*, 8497–8520. [CrossRef] [PubMed]
110. Kuś, S.L.S.; Otremba, M.; Taniewski, M. The Catalytic Performance in Oxidative Coupling of Methane and the Surface Basicity of La_2O_3, Nd_2O_3, ZrO_2 and Nb_2O_5. *Fuel* **2003**, *82*, 1331–1338. [CrossRef]

111. Arndt, S.; Simon, U.; Heitz, S.; Berthold, A.; Beck, B.; Görke, O.; Epping, J.D.; Otremba, T.; Aksu, Y.; Irran, E.; et al. Li-Doped MgO from Different Preparative Routes for the Oxidative Coupling of Methane. *Top. Catal.* **2011**, *54*, 1266–1285. [CrossRef]
112. Pannek, U.; Mleczko, L. Comprehensive Model of Oxidative Coupling of Methane in a Fluidized-Bed Reactor. *Chem. Eng. Sci.* **1996**, *51*, 3575–3590. [CrossRef]
113. Jašo, S.; Arellano-Garcia, H.; Wozny, G. Oxidative Coupling of Methane in a Fluidized Bed Reactor: Influence of Feeding Policy, Hydronamics and Rector Geometry. *Chem. Eng. J.* **2011**, *171*, 255–271. [CrossRef]
114. Salehi, M.S.; Askarishahi, M.; Godini, H.R.; Schomäcker, R.; Wozny, G. CFD Simulation of Oxidative Coupling of Methane in Fluidized-Bed Reactors: A Detailed Analysis of Flow-Reaction Characteristics and Operating Conditions. *Ind. Eng. Chem. Res.* **2016**, *55*, 1149–1163. [CrossRef]
115. Holst, N.; Jašo, S.; Godini, H.R.; Glöser, S.; Arellano-Garcia, H.; Wozny, G.; Steinbach, J. Two-Dimensional Model for Oxidative Coupling of Methane in a Packed-Bed Membrane Reactor. *Chem. Eng. Technol.* **2012**, *35*, 294–301. [CrossRef]
116. Godini, H.R.; Xiao, S.; Kim, M.; Holst, N.; Jašo, S.; Görke, O.; Steinbach, J.; Wozny, G. Experimental and Model-Based Analysis of Membrane Reactor Performance for Methane Oxidative Coupling: Effect of Radial Heat and Mass Transfer. *J. Ind. Eng. Chem.* **2014**, *20*, 1993–2002. [CrossRef]
117. Onoja, O.P.; Wang, X.; Kechagiopoulos, P.N. Influencing Selectivity in the Oxidative Coupling of Methane by Modulating Oxygen Permeation in a Variable Thickness Membrane Reactor. *Chem. Eng. Process. Process Intensif.* **2019**, *135*, 156–167. [CrossRef]
118. Couwenberg, P.M.; Chen, Q.; Marin, G.B. Irreducible Mass-Transport Limitations during a Heterogeneously Catalyzed Gas-Phase Chain Reaction: Oxidative Coupling of Methane. *Ind. Eng. Chem. Res.* **1996**, *35*, 415–421. [CrossRef]
119. Yaghobi, N.; Ghoreishy, M.H.R. Oxidative Coupling of Methane in a Fixed Bed Reactor over Perovskite Catalyst: A Simulation Study Using Experimental Kinetic Model. *J. Nat. Gas Chem.* **2008**, *17*, 8–16. [CrossRef]
120. Sun, Z.; West, D.H.; Balakotaiah, V. Bifurcation Analysis of Catalytic Partial Oxidations in Laboratory-Scale Packed-Bed Reactors with Heat Exchange. *Chem. Eng. J.* **2019**, *377*. [CrossRef]
121. Sun, Z.; West, D.H.; Gautam, P.; Balakotaiah, V. Scale-up Analysis of Autothermal Operation of Methane Oxidative Coupling with La_2O_3/CaO Catalyst. *AIChE J.* **2020**, *66*, e16949. [CrossRef]
122. Zhang, Z.; Ji, S. Numerical Simulation of Particle/Monolithic Two-Stage Catalyst Bed Reactor with Beds-Interspace Distributed Dioxygen Feeding for Oxidative Coupling of Methane. *Comput. Chem. Eng.* **2016**, *90*, 247–259. [CrossRef]
123. Vandewalle, L.A.; Van de Vijver, R.; Van Geem, K.M.; Marin, G.B. The Role of Mass and Heat Transfer in the Design of Novel Reactors for Oxidative Coupling of Methane. *Chem. Eng. Sci.* **2019**, *198*, 268–289. [CrossRef]
124. Cruellas, A.; Melchiori, T.; Gallucci, F.; van Sint Annaland, M. Advanced Reactor Concepts for Oxidative Coupling of Methane. *Catal. Rev. Sci. Eng.* **2017**, *59*, 234–294. [CrossRef]
125. Froment, G.; Bischoff, K.; De Wilde, J. *Chemical Reactor Analysis and Design*, 2nd ed.; Wiley Subscription Services, Inc., A Wiley Company: New York, NY, USA, 2011.
126. Alexiadis, V.I.; Thybaut, J.W.; Kechagiopoulos, P.N.; Chaar, M.; Van Veen, A.C.; Muhler, M.; Marin, G.B. Oxidative Coupling of Methane: Catalytic Behaviour Assessment via Comprehensive Microkinetic Modelling. *Appl. Catal. B Environ.* **2014**, *150–151*, 496–505. [CrossRef]
127. Sarsani, S.; West, D.; Liang, W.; Balakotaiah, V. Autothermal Oxidative Coupling of Methane with Ambient Feed Temperature. *Chem. Eng. J.* **2017**, *328*, 484–496. [CrossRef]
128. Vandewalle, L.A.; Lengyel, I.; West, D.H.; Van Geem, K.M.; Marin, G.B. Catalyst Ignition and Extinction: A Microkinetics-Based Bifurcation Study of Adiabatic Reactors for Oxidative Coupling of Methane. *Chem. Eng. Sci.* **2019**, *199*, 635–651. [CrossRef]
129. Dautzenberg, F.M.; Schlatter, J.C. Catalyst and Reactor Requirements for the Oxidative Coupling of Methane. *Catal. Today* **1992**, *13*, 503–5r09. [CrossRef]
130. Kato, K.; Wen, C.Y. Bubble Assemblage Model for Fluidized Bed Catalytic Reactors. *Chem. Eng. Sci.* **1969**, *24*, 1351–1369. [CrossRef]
131. Mleczko, L.; Schweer, D.; Durjanova, Z.; Andorf, R.; Baerns, M. Reaction Engineering Approaches to the Oxidative Coupling of Methane to C2+ Hydrocarbons. *Stud. Surf Sci. Catal.* **1992**, *81*, 155–164.
132. Uglietti, R.; Bracconi, M.; Maestri, M. Coupling CFD-DEM and Microkinetic Modeling of Surface Chemistry for the Simulation of Catalytic Fluidized Systems. *React. Chem. Eng.* **2018**, *3*, 527–539. [CrossRef]
133. Cruellas, A.; Melchiori, T.; Gallucci, F.; van Sint Annaland, M. Oxidative Coupling of Methane: A Comparison of Different Reactor Configurations. *Energy Technol.* **2019**, *8*, 1900148. [CrossRef]
134. Pak, S.; Lunsford, J.H. Thermal Effects during the Oxidative Coupling of Methane over $Mn/Na_2WO_4/SiO_2$ and $Mn/Na_2WO_4/MgO$ Catalysts. *Appl. Catal. A Gen.* **1998**, *168*, 131–137. [CrossRef]
135. Noon, D.; Zohour, B.; Senkan, S. Oxidative Coupling of Methane with La_2O_3-CeO_2 Nanofiber Fabrics: A Reaction Engineering Study. *J. Nat. Gas Sci. Eng.* **2014**, *18*, 406–411. [CrossRef]
136. Lee, J.Y.; Jeon, W.; Choi, J.W.; Suh, Y.W.; Ha, J.M.; Suh, D.J.; Park, Y.K. Scaled-up Production of C2 Hydrocarbons by the Oxidative Coupling of Methane over Pelletized $Na_2WO_4/Mn/SiO_2$ Catalysts: Observing Hot Spots for the Selective Process. *Fuel* **2013**, *106*, 851–857. [CrossRef]
137. Liu, H.; Wang, X.; Yang, D.; Gao, R.; Wang, Z.; Yang, J. Scale up and Stability Test for Oxidative Coupling of Methane over Na_2WO_4-Mn/SiO_2 Catalyst in a 200 Ml Fixed-Bed Reactor. *J. Nat. Gas Chem.* **2008**, *17*, 59–63. [CrossRef]

138. Geerts, J.W.M.H.; Chen, Q.; van Kasteren, J.M.N.; van der Wiele, K. Thermodynamics and Kinetic Modeling of the Homogeneous Gas Phase Reactions of the Oxidative Coupling of Methane. *Catal. Today* **1990**, *6*, 519–526. [CrossRef]
139. Farrell, B.L.; Igenegbai, V.O.; Linic, S. A Viewpoint on Direct Methane Conversion to Ethane and Ethylene Using Oxidative Coupling on Solid Catalysts. *ACS Catal.* **2016**, *6*, 4340–4346. [CrossRef]
140. Thybaut, J.W.; Marin, G.B.; Mirodatos, C.; Schuurman, Y.; Van Veen, A.C.; Sadykov, V.A.; Pennemann, H.; Bellinghausen, R.; Mleczko, L. A Novel Technology for Natural Gas Conversion by Means of Integrated Oxidative Coupling and Dry Reforming of Methane. *Chem. Ingenieur Tech.* **2014**, *86*, 1855–1870. [CrossRef]
141. Koretsky, M.D. *Engineering and Chemical Thermodynamics*, 2nd ed.; John Wiley & Sons, Inc.: Hoboken, NJ, USA, 2013.
142. Su, Y.S.; Ying, J.Y.; Green, W.H. Upper Bound on the Yield for Oxidative Coupling of Methane. *J. Catal.* **2003**, *218*, 321–333. [CrossRef]
143. Scheid, A.J.; Barbosa-Coutinho, E.; Schwaab, M.; Salau, N.P.G. GPREC—Gas-Phase Reaction Equilibrium Calculator. Computer program in Fortran/Matlab, registered in the Brazilian National Institute of Intellectual Property (INPI), under No BR 51 2017 001692 5.
144. Barnes, C.; Koretsky, M.D. *ThermoSolver*; John Wiley & Sons, Inc.: Hoboken, NJ, USA, 2003.
145. Machocki, A.; Denis, A. Simultaneous Oxidative Coupling of Methane and Oxidative Dehydrogenation of Ethane on the Na^+/CaO Catalyst. *Chem. Eng. J.* **2002**, *90*, 165–172. [CrossRef]
146. Snytnikov, V.N.; Mishchenko, T.I.; Snytnikov, V.N.; Malykhin, S.E.; Avdeev, V.I.; Parmon, V.N. Autocatalytic Gas-Phase Dehydrogenation of Ethane. *Res. Chem. Intermed.* **2012**, *38*, 1133–1147. [CrossRef]
147. Korf, S.J.; Roos, J.A.; De Bruijn, N.A.; Van Ommen, J.G.; Ross, J.R.H. Influence of CO_2 on the Oxidative Coupling of Methane over a Lithium Promoted Magnesium Oxide Catalyst. *J. Chem. Soc. Chem. Commun.* **1987**, *19*, 1433–1434. [CrossRef]
148. Thum, L.; Rudolph, M.; Schomäcker, R.; Wang, Y.; Tarasov, A.; Trunschke, A.; Schlögl, R. Oxygen Activation in Oxidative Coupling of Methane on Calcium Oxide. *J. Phys. Chem. C* **2019**, *123*, 8018–8026. [CrossRef]
149. Sarsani, V.S.R.; West, D.; Lengyel, I. Method for Producing Hydrocarbons by Oxidative Coupling of Methane with a Heavy Diluent. U.S. Patent 2017/0057889 A1, 2 March 2017.
150. Cai, X.; Hu, Y.H. Advances in Catalytic Conversion of Methane and Carbon Dioxide to Highly Valuable Products. *Energy Sci. Eng.* **2019**, *7*, 4–29. [CrossRef]
151. Istadi Amin, N.A.S. Co-Generation of C_2 Hydrocarbons and Synthesis Gases from Methane and Carbon Dioxide: A Thermodynamic Analysis. *J. Nat. Gas Chem.* **2005**, *14*, 140–150.
152. Rafique, H.A.; Vuddagiri, S.; Radaelli, G.; Scher, E.C.; McCormick, J.; Cizeron, J. Oxidative Coupling of Methane Implementation for Olefin Production. U.S. Patent 9352295B2, 31 May 2016.
153. Iwamoto, M.; Lunsford, J.H. Surface Reactions of Oxygen Ions. 5. Oxidation of Alkanes and Alkenes by O^{2-} on MgO. *J. Phys. Chem.* **1980**, *84*, 3079–3084. [CrossRef]
154. Kumar, G.; Lau, S.L.J.; Krcha, M.D.; Janik, M.J. Correlation of Methane Activation and Oxide Catalyst Reducibility and Its Implications for Oxidative Coupling. *ACS Catal.* **2016**, *6*, 1812–1821. [CrossRef]
155. Zavyalova, U.; Holena, M.; Schlögl, R.; Baerns, M. Statistical Analysis of Past Catalytic Data on Oxidative Methane Coupling for New Insights into the Composition of High-Performance Catalysts. *ChemCatChem* **2011**, *3*, 1935–1947. [CrossRef]
156. Gambo, Y.; Jalil, A.A.; Triwahyono, S.; Abdulrasheed, A.A. Recent Advances and Future Prospect in Catalysts for Oxidative Coupling of Methane to Ethylene: A Review. *J. Ind. Eng. Chem.* **2018**, *59*, 218–229. [CrossRef]
157. Schucker, R.C.; Derrickson, K.J.; Ali, A.K.; Caton, N.J. Identification of the Optimum Catalyst and Operating Conditions for Oxidative Coupling of Methane: Activity and Selectivity of Alkaline Earth-Doped Lanthanides. *Ind. Eng. Chem. Res.* **2020**, *59*, 18434–18446. [CrossRef]
158. Gao, Z.; Zhang, J.; Wang, R. Formation of Hydrogen in Oxidative Coupling of Methane over $BaCO_3$ and MgO Catalysts. *J. Nat. Gas Chem.* **2008**, *17*, 238–241. [CrossRef]
159. Rane, V.H.; Chaudhari, S.T.; Choudhary, V.R. Oxidative Coupling of Methane over La-Promoted CaO Catalysts: Influence of Precursors and Catalyst Preparation Method. *J. Nat. Gas Chem.* **2010**, *19*, 25–30. [CrossRef]
160. Baidya, T.; Van Vegten, N.; Verel, R.; Jiang, Y.; Yulikov, M.; Kohn, T.; Jeschke, G.; Baiker, A. $SrO{\cdot}Al_2O_3$ Mixed Oxides: A Promising Class of Catalysts for Oxidative Coupling of Methane. *J. Catal.* **2011**, *281*, 241–253. [CrossRef]
161. Yunarti, R.T.; Lee, M.; Hwang, Y.J.; Choi, J.W.; Suh, D.J.; Lee, J.; Kim, I.W.; Ha, J.M. Transition Metal-Doped TiO_2 Nanowire Catalysts for the Oxidative Coupling of Methane. *Catal. Commun.* **2014**, *50*, 54–58. [CrossRef]
162. Simon, U.; Arndt, S.; Otremba, T.; Schlingmann, T.; Görke, O.; Dinse, K.P.; Schomäcker, R.; Schubert, H. Li/MgO with Spin Sensors as Catalyst for the Oxidative Coupling of Methane. *Catal. Commun.* **2012**, *18*, 132–136. [CrossRef]
163. Scher, E.C.; Zurcher, F.R.; Cizeron, J.M.; Schammel, W.P.; Tkachenko, A.; Karshtedt, D.; Nyce, G. Nanowire Catalysts. U.S. Patent Application WO2011/149996A2, 1 December 2011.
164. Rane, V.H.; Chaudhari, S.T.; Choudhary, V.R. Influence of Alkali Metal Doping on Surface Properties and Catalytic Activity/Selectivity of CaO Catalysts in Oxidative Coupling of Methane. *J. Nat. Gas Chem.* **2008**, *17*, 313–320. [CrossRef]
165. Arndt, S.; Laugel, G.; Levchenko, S.; Horn, R.; Baerns, M.; Scheffler, M.; Schlögl, R.; Schomäcker, R. A Critical Assessment of Li/MgO-Based Catalysts for the Oxidative Coupling of Methane. *Catal. Rev. Sci. Eng.* **2011**, *53*, 424–514. [CrossRef]
166. Song, J.; Sun, Y.; Ba, R.; Huang, S.; Zhao, Y.; Zhang, J.; Sun, Y.; Zhu, Y. Monodisperse Sr-La_2O_3 Hybrid Nanofibers for Oxidative Coupling of Methane to Synthesize C2 Hydrocarbons. *Nanoscale* **2015**, *7*, 2260–2264. [CrossRef] [PubMed]

167. Galadima, A.; Muraza, O. Revisiting the Oxidative Coupling of Methane to Ethylene in the Golden Period of Shale Gas: A Review. *J. Ind. Eng. Chem.* **2016**, *37*, 1–13. [CrossRef]
168. He, Y.; Yang, B.; Cheng, G. On the Oxidative Coupling of Methane with Carbon Dioxide over CeO_2/ZnO Nanocatalysts. *Catal. Today* **2004**, *98*, 595–600. [CrossRef]
169. Noon, D.; Seubsai, A.; Senkan, S. Oxidative Coupling of Methane by Nanofiber Catalysts. *ChemCatChem* **2013**, *5*, 146–149. [CrossRef]
170. Kolmakov, A.; Moskovits, M. Chemical Sensing and Catalysis By One-Dimensional Metal-Oxide Nanostructures. *Annu. Rev. Mater. Res.* **2004**, *34*, 151–180. [CrossRef]
171. Chinta, S.; Thorman, J.; Butler, J.; Rives, T. Process for the Oxidative Coupling. U.S. Patent 8912381B2, 29 June 2009.
172. Tanaka, K.; Sekine, Y.; Inoue, J.; Araki, H.; Matsukata, M.; Kikuchi, E. Oxidative Coupling of Methane over Ba-Incorporate $LaInO_3$ Perovskite Catalyst. *J. Jpn. Pet. Inst.* **2012**, *55*, 71–72. [CrossRef]
173. Ivanov, D.V.; Isupova, L.A.; Gerasimov, E.Y.; Dovlitova, L.S.; Glazneva, T.S.; Prosvirin, I.P. Oxidative Methane Coupling over Mg, Al, Ca, Ba, Pb-Promoted $SrTiO_3$ and Sr_2TiO_4: Influence of Surface Composition and Microstructure. *Appl. Catal. A Gen.* **2014**, *485*, 10–19. [CrossRef]
174. Ghose, R.; Hwang, H.T.; Varma, A. Catalysts for Oxidative Coupling of Methane and Solution Combustion Method for the Production of the Same. U.S. Patent 9610565 B2, 4 April 2017.
175. Othman, N.H.; Wu, Z.; Li, K. Micro-Structured $Bi_{1.5}Y_{0.3}Sm_{0.2}O_3$-Alpha Catalysts for Oxidative Couplinf of Methane. *AIChE J.* **2015**, *61*, 3451–3458. [CrossRef]
176. Huang, K.; Chen, F.-Q.; Lu, D.-W. Artificial Neural Network-Aided Design of Multi-Component Catalyst for Methane Oxidative Coupling. *Appl. Catal. A Gen.* **2001**, *219*, 61–68. [CrossRef]
177. Huang, K.; Zhan, X.L.; Chen, F.Q.; Lü, D.W. Catalyst Design for Methane Oxidative Coupling by Using Artificial Neural Network and Hybrid Genetic Algorithm. *Chem. Eng. Sci.* **2003**, *58*, 81–87. [CrossRef]
178. Cizeron, J.M.; Scher, E.C.; Zurcher, F.R.; Schammel, W.P.; Nyce, G.; Rumplecker, A.; McCormick, J.; Alcid, M.; Gamoras, J.; Rosenberg, D.; et al. Catalysts for Petrochemical Catalysis. U.S. Patent 2013/0023709A1, 24 January 2013.
179. Dedov, A.G.; Loktev, A.S.; Nipan, G.D.; Dorokhov, S.N.; Golikov, S.D.; Spesivtsev, N.A.; Moiseev, I.I. Oxidative Coupling of Methane to Form Ethylene: Effect of the Preparation Method on the Phase Composition and Catalytic Properties of Li-W-Mn-O-SiO_2 Composite Materials. *Pet. Chem.* **2015**, *55*, 163–168. [CrossRef]
180. Zhang, B.; Wang, J.; Chou, L.; Song, H.; Zhao, J.; Yang, J.; Li, S. Effective and Stable CeO_2-W-Mn/SiO_2 Catalyst for Methane Oxidation to Ethylene and Ethane. *Stud. Surf. Sci. Catal.* **2007**, *167*, 237–242. [CrossRef]
181. Arndt, S.; Otremba, T.; Simon, U.; Yildiz, M.; Schubert, H.; Schomäcker, R. Mn-Na 2WO 4/SiO_2 as Catalyst for the Oxidative Coupling of Methane. What Is Really Known? *Appl. Catal. A Gen.* **2012**, *425*, 53–61. [CrossRef]
182. Werny, M.J.; Wang, Y.; Girgsdies, F.; Schlögl, R.; Trunschke, A. Fluctuating Storage of the Active Phase in a Mn-Na_2WO_4/SiO_2 Catalyst for the Oxidative Coupling of Methane. *Angew. Chem. Int. Ed.* **2020**, *59*, 14921–14926. [CrossRef]
183. Liu, W.C.; Ralston, W.T.; Melaet, G.; Somorjai, G.A. Oxidative Coupling of Methane (OCM): Effect of Noble Metal (M = Pt, Ir, Rh) Doping on the Performance of Mesoporous Silica MCF-17 Supported Mn_xO_y-Na_2WO_4 Catalysts. *Appl. Catal. A Gen.* **2017**, *545*, 17–23. [CrossRef]
184. Gordienko, Y.; Usmanov, T.; Bychkov, V.; Lomonosov, V.; Fattakhova, Z.; Tulenin, Y.; Shashkin, D.; Sinev, M. Oxygen Availability and Catalytic Performance of NaWMn/SiO_2 Mixed Oxide and Its Components in Oxidative Coupling of Methane. *Catal. Today* **2016**, *278*, 127–134. [CrossRef]
185. Simon, U.; Görke, O.; Berthold, A.; Arndt, S.; Schomäcker, R.; Schubert, H. Fluidized Bed Processing of Sodium Tungsten Manganese Catalysts for the Oxidative Coupling of Methane. *Chem. Eng. J.* **2011**, *168*, 1352–1359. [CrossRef]
186. Nguyen, T.N.; Nhat, T.T.P.; Takimoto, K.; Thakur, A.; Nishimura, S.; Ohyama, J.; Miyazato, I.; Takahashi, L.; Fujima, J.; Takahashi, K.; et al. High-Throughput Experimentation and Catalyst Informatics for Oxidative Coupling of Methane. *ACS Catal.* **2020**, *10*, 921–932. [CrossRef]
187. Yildiz, M.; Simon, U.; Otremba, T.; Aksu, Y.; Kailasam, K.; Thomas, A.; Schomäcker, R.; Arndt, S. Support Material Variation for the Mn_xO_y-Na_2WO_4/SiO_2 Catalyst. *Catal. Today* **2014**, *228*, 5–14. [CrossRef]
188. Ha, J.M.; Suh, D.J.; Choi, J.W.; Yoon, Y.H.; Yang, G.S.; Jeon, W. Catalyst for Oxidative Coupling of Methane, Method for Preparing the Same, and Method for Oxidative Coupling Reaction of Methane Using the Same. U.S. Patent 2013178680A1, 11 July 2013.
189. Ji, S.; Xiao, T.; Li, S.; Chou, L.; Zhang, B.; Xu, C.; Hou, R.; York, A.P.E.; Green, M.L.H. Surface WO4 Tetrahedron: The Essence of the Oxidative Coupling of Methane over M-W-Mn/SiO_2 Catalysts. *J. Catal.* **2003**, *220*, 47–56. [CrossRef]
190. Park, L.H.; Jo, Y.R.; Choi, J.W.; Suh, D.J.; Song, K.H.; Ha, J.M. SiO_2@MnO: X@Na_2WO_4@SiO_2core-Shell-Derived Catalyst for Oxidative Coupling of Methane. *RSC Adv.* **2020**, *10*, 37749–37756. [CrossRef]
191. Shi, J.; Yao, L.; Hu, C. Effect of CO_2 on the Structural Variation of Na_2WO_4/Mn/SiO_2 Catalyst for Oxidative Coupling of Methane to Ethylene. *J. Energy Chem.* **2015**, *24*, 394–400. [CrossRef]
192. Yildiz, M.; Aksu, Y.; Simon, U.; Kailasam, K.; Goerke, O.; Rosowski, F.; Schomacker, R.; Thomas, A.; Arndt, S. Enhanced Catalytic Performance of MnxOy–Na_2WO_4/SiO_2 for the Oxidative Coupling of Methane Using an Ordered Mesoporous Silica Support. *Chem. Commun.* **2014**, *50*, 14440–14442. [CrossRef] [PubMed]
193. Karakaya, C.; Kee, R.J. Progress in the Direct Catalytic Conversion of Methane to Fuels and Chemicals. *Prog. Energy Combust. Sci.* **2016**, *55*, 60–97. [CrossRef]

194. Thiruvenkataswamy, P.; Eljack, F.T.; Roy, N.; Mannan, M.S.; El-Halwagi, M.M. Safety and Techno-Economic Analysis of Ethylene Technologies. *J. Loss Prev. Process Ind.* **2016**, *39*, 74–84. [CrossRef]
195. Huang, C.H.; Tan, C.S. A Review: CO_2 Utilization. *Aerosol Air Qual. Res.* **2014**, *14*, 480–499. [CrossRef]
196. Song, C. Global Challenges and Strategies for Control, Conversion and Utilization of CO_2 for Sustainable Development Involving Energy, Catalysis, Adsorption and Chemical Processing. *Catal. Today* **2006**, *115*, 2–32. [CrossRef]
197. Chauvy, R.; De Weireld, G. CO_2 Utilization Technologies in Europe: A Short Review. *Energy Technol.* **2020**, *8*, 2000627. [CrossRef]
198. Hepburn, C.; Adlen, E.; Beddington, J.; Carter, E.A.; Fuss, S.; Mac Dowell, N.; Minx, J.C.; Smith, P.; Williams, C.K. The Technological and Economic Prospects for CO_2 Utilization and Removal. *Nature* **2019**, *575*, 87–97. [CrossRef] [PubMed]
199. Radaelli, G.; Rafique, H.A.; Vuddagiri, S.; Scher, E.C.; McCormick, J.; Cizeron, J.; Patel, B.; Lakhapatri, S. Efficient Oxidative Coupling of Methane Processes and Systems. U.S. Patent Application 2016/0272557A1, 22 September 2016.